5-1-2013

A Measurement of the W/Z Cross Section Ratio as a Function of Hadronic Activity with the ATLAS Detector

Andrew Robert Meade
University of Massachusetts - Amherst, ameadephysics@gmail.com

Recommended Citation

Meade, Andrew Robert, "A Measurement of the W/Z Cross Section Ratio as a Function of Hadronic Activity with the ATLAS Detector" (2013). *Dissertations.* Paper 757.

A MEASUREMENT OF THE W/Z CROSS SECTION RATIO AS A FUNCTION OF HADRONIC ACTIVITY WITH THE ATLAS DETECTOR

A Dissertation Presented

by

ANDREW MEADE

Submitted to the Graduate School of the
University of Massachusetts Amherst in partial fulfillment
of the requirements for the degree of

DOCTOR OF PHILOSOPHY

May 2013

Physics

A MEASUREMENT OF THE W/Z CROSS SECTION RATIO AS A FUNCTION OF HADRONIC ACTIVITY WITH THE ATLAS DETECTOR

A Dissertation Presented

by

ANDREW MEADE

Approved as to style and content by:

Benjamin Brau, Chair

Stéphane Willocq, Member

John Donoghue, Member

Min Yun, Member

Donald Candela, Department Chair
Physics

Thank you to my family, who supported me through all the shaky moments, and to all my friends old and new, who made these last few years not just bearable, but a joy.

ABSTRACT

A MEASUREMENT OF THE W/Z CROSS SECTION RATIO AS A FUNCTION OF HADRONIC ACTIVITY WITH THE ATLAS DETECTOR

MAY 2013

ANDREW MEADE

B.A., SWARTHMORE COLLEGE, SWARTHMORE, PA

M.Sc., UNIVERSITY OF MASSACHUSETTS, AMHERST

Ph.D., UNIVERSITY OF MASSACHUSETTS, AMHERST

Directed by: Professor Benjamin Brau

Hadronic collisions at the LHC at CERN probe particle interactions at the highest energy scale of any experiment to date. We present a research program measuring $R_{\text{jet}} = \frac{\sigma_W BR(W\rightarrow\mu\nu)}{\sigma_Z BR(Z\rightarrow\mu\mu)}$ as a function of a number of hadronic variables. The measurements are performed with the ATLAS detector at the LHC, using the 2011 data set, consisting of 4.64 fb^{-1} of pp collisions at a center of mass energy of 7 TeV. This measurement is a robust way to test the Standard Model and the modeling of perturbative QCD, and is sensitive to a wide variety of possible new physics in events with high jet E_T, including some variations of Supersymmetry. By taking the ratio of W/Z production, a large number of systematic uncertainties cancel, including those associated with luminosity, jet energy scale and resolution, and many theoretical uncertainties.

The measurement of R_{jet} is performed as a function of the p_{T} and rapidity of the 1st-4th leading jet, S_T, H_T, and a number of dijet variables: invariant mass, ΔR_{jj} and $\Delta\phi_{jj}$. The measurements are compared with NLO theoretical predictions from BlackHat+Sherpa, as well as using leading order simulations from Alpgen and Sherpa. Over most of the kinematic phase-space, there is good agreement between the data and theoretical predictions. There is a significant deviation for exactly one selected jet above 30 GeV, where BlackHat+Sherpa over-estimates the ratio R_{jet} by 12%.

TABLE OF CONTENTS

Page

CHAPTER

List of Tables

Table **Page**

List of Figures

INTRODUCTION

Experimental particle physics seeks to understand the most fundamental constituents of matter and their interactions. A theme in this quest for understanding has been unification, the idea that often seeming disparate phenomena can be explained by a single coherent framework. Physicists generally agree that this represents a more fundamental understanding than disconnected explanations for phenomena as diverse as optics, nuclear phenomena and contact interactions. The birth of physics as a discipline is rooted in this idea. When Isaac Newton developed and published his theories of universal gravitation and classical mechanics, they showed definitively that the celestial sphere was governed by the same laws that we experience on earth.

The theme of unification has similarly been a driving force in modern particle physics. The unification of the weak and electromagnetic theory was accomplished in the 1960's with the most notable contributions by Weinberg, Salam, and Glashow [4, 5, 6]. The discovery of confined, fractionally charged quarks in the nucleus 1974 accompanied advances in non-abelian gauge theories to eventually lead to the development of Quantum Chromodynamics. These two theories together represent the crowning achievement of modern particle physics: the Standard Model, in which all particles and forces come out of a specific gauge symmetry group SU(3) x SU(2) x U(1), and describe all observed particle phenomena.

The Standard Model of particle physics has shown unparalleled success in describing the behavior of fundamental particles. In particular, the electroweak sector has been carefully probed: the masses, cross sections and couplings of the W and Z bosons have been very carefully measured at LEP, SLD and the Tevatron. Before the LHC, all but one of particles predicted by the Standard Model had been successfully measured, and all free parameters of the theory had been measured but one, the mass of the Higgs boson. The existence of massive electroweak bosons (W,Z) indicates that the theory's SU(2) x U(1) symmetry must be broken somehow for the Standard Model to retain its predictive power. The Higgs Mechanism is the current favored model for how this occurs, and predicts the existence of a new particle, the Higgs Boson. The lack of experimental evidence for the mechanism of electroweak symmetry breaking was one of the primary motivations for constructing the Large Hadron Collider (LHC).

Proton collisions at the LHC probe electroweak and hadronic interactions at a new energy scale. Due to electroweak constraints on the Higgs mass, it was expected that the explanation for electroweak symmetry breaking should be discovered by the LHC. During the writing of this thesis, a particle has been discovered by the the experiments at the LHC (ATLAS,CMS), with a mass of approximately 126 GeV, consistent with the production and decay of the Standard Model Higgs Boson [1]. The LHC will continue to measure this particle in order to further elucidate electroweak symmetry breaking. In addition, the LHC hopes to address other problems inherent to the Standard Model, such as the hierarchy problem, the strong CP problem, as well as cosmological issues such as the source of dark matter and an explanation for baryogenesis in the early universe.

Because of the importance of electroweak physics to the LHC's mission, the doctoral research presented in this thesis centers around the measurement of W and Z boson cross sections. Specifically this thesis seeks to measure the ratio of the production cross sections times their branching fractions to leptons: $R_{\text{jet}} = \frac{\sigma_W BR(W \to \ell\nu)}{\sigma_Z BR(Z \to \ell\ell)}$ as a function of the number of associated jets and other hadronic variables such as their scalar sum of transverse energy $S_T = \sum E_{T jets}$. In this case ℓ refers to muons or electrons. This study builds on the 2010 measurement of R_{jet} as a function of lead jet p_{T} [7], but is expanded in both scope and the amount of integrated luminosity. At the Tevatron, running at a center of mass energy ($\sqrt{s}$) of 1.98 TeV and with $p\bar{p}$ collisions, the inclusive ratio R was measured to be 10.82 [8]. This quantity is slightly lower for pp collisions due to their different quark content, and is weakly dependent on $\sqrt{s}$, as at higher values there is a higher proportion of virtual $\bar{u}$ and $\bar{d}$ quarks that can interact to produce a Z boson.

In the high jet E_T regime accessible by ATLAS, R_{jet} has not been probed previously experimentally, and is sensitive to many new physics models, including some varieties of Supersymmetry. Because the measurement is not tailored to any particular model, it can be viewed as a type of model independent search. In addition, the W/Z cross section ratio has further advantages as an early physics measurement, as many systematic uncertainties associated with luminosity and detector effects are canceled or reduced in the ratio. In addition, the W/Z boson characteristics have been measured very precisely at LEP and the Tevatron. This gives the measurement sound footing, as the low jet p_T regime can be used to cross check results.

These measurements are performed in two separate channels: with the bosons decaying to muons, and with the bosons decaying into electrons, as these two channels have differing reconstruction characteristics and systematics due to the different signatures of electrons and muons in the ATLAS detector. This thesis will present the results only for the muon channel, but future publications will include results from both channels.

Chapter 1 examines the structure of the Standard Model, and its history, successes, and shortfalls. Theoretical models which provide solutions for these shortfalls are briefly discussed, with a focus on models which could alter the value of R_{jet} over some kinematic range. The details of the Monte Carlo generators used to provide the theoretical modeling in this thesis is also be covered. Chapter 2 describes the ATLAS detector and the LHC at CERN, with a focus on the detector elements responsible for reconstruction of physics objects. This informs a discussion of the details of the reconstruction of electrons, muons, $E_{\mathrm{T}}^{\mathrm{miss}}$, and jets, which in turn illuminates the object definitions used in this thesis.

Chapter 3 summarizes the details of the measurement of R_{jet} using 4.64 fb^{-1} at 7 TeV center of mass energy, as a function of the following variables: the number of jets, the p_{T} and rapidity of the 1st-4th leading jets, and a number of other derived hadronic quantities: S_T, H_T, dijet mass, ΔR_{jj} and $\Delta\phi_{jj}$. Cross checks, background subtraction, acceptance and efficiency corrections, systematic uncertainty estimation and theoretical predictions are discussed. Chapter 4 summarizes the results of the research program and explores possible future directions for related research.

CHAPTER 1

THEORETICAL BACKGROUND

The Standard Model (SM) is not only successful in describing particle phenomena, but is also theoretically elegant, as it can be derived from the assumption of a small number of symmetries and principles. The SM is built on the framework of relativistic quantum field theory, which developed gradually in the 1930's, and lead to the prediction of anti-particles. All particle characteristics and dynamics predicted by the Standard Model can be determined by requiring that the Lagrangian of the theory obey a particular set of gauge symmetries: SU(3) for Quantum Chromodynamics, and SU(2)xU(1) for Electroweak dynamics. A formal treatment of quantum field theory can be found in Ref.[9], and a full treatment of the derivation of the Standard Model can be found in Ref.[10].

This Chapter will briefly explain the dynamics of the Strong and Electroweak sectors, and the mechanism of Electroweak Symmetry Breaking. Motivations for the R_{jet} measurement in understanding the Standard Model will be discussed. Conceptual problems with the Standard Model will then be explored. Supersymmetry will be briefly explored as an example of a theory that goes beyond the Standard Model and that could solve or illuminate these problems. Focus will be given to ways these theories could contribute to an altered R_{jet} signal. The Chapter will conclude with an overview of collider physics, and how this physics is modeled in the simulations used in this thesis.

1.1 The Standard Model and its Constituents

With the exception of the scalar Higgs Boson, all Standard Model particles can be classified into one of two categories: spin 1/2 fermions, which due to the Pauli-exclusion principle exhibit the sort of space occupying properties we associate with “matter”, and spin 1 bosons, which due to their own quantum statistics, act not as static matter, but as “force-carriers” that act as the quanta for field or wave interactions.

Figure 1.1 shows all known fundamental particles in the Standard Model, and their masses. Fermionic particles (matter) are divided into leptons, which are subject to only the electroweak interaction, and quarks, which are subject to both the electroweak and strong interactions. Electrons and their neutrinos (leptons) and up and down quarks are the lightest fermions, and represent the constituents of most “ordinary”, stable matter that makes up the plants, animals and all other objects with which we are familiar. Two more generations of quarks and leptons have been discovered experimentally, with identical charges and spin as their more abundant counterparts, but with greater mass. These particles are not stable, but are produced in high energy collisions, and influence the characteristics of stable matter through their existence as virtual particles.

Leptons: Each generation of leptons has a charged lepton with electric charge e (1.60 $\times 10^{-19}$ C), and a corresponding electrically neutral neutrino. Electrons, muons and taus (e,μ,τ) are the lightest, second lightest and heaviest charged leptons. Their corresponding neutrinos are denoted ν_e, ν_μ, and ν_τ. Neutrinos were only recently discovered to have mass; prior to the discovery of neutrino flavor oscillations they were assumed to be massless. Cosmological limits using WMAP data and photometric red-shift surveys place the sum of the three neutrino masses at less than 0.3 eV [11]. Current laboratory experiments put weaker bounds on these masses, $m < 2\,\text{eV}, 170\,\text{keV}, 18\,\text{MeV}$ for the electron, muon and tau, respectively (these mea-

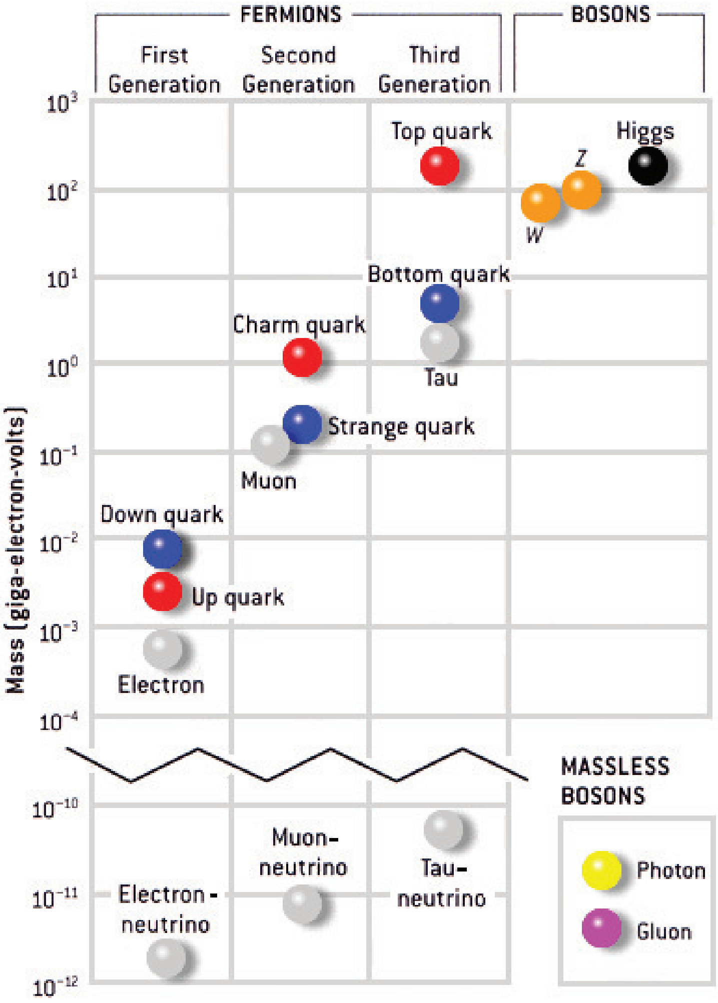

Figure 1.1. Constituent particles of the Standard Model, arranged according to their masses and generations. The scalar Higgs boson, shown on this diagram, is a hypothetical particle posited to explain mass generation and electroweak symmetry breaking. A new particle consistent with the Higgs Boson has recently been discovered at the LHC by ATLAS and CMS [1]. Image from Scientific American, used through fair use [2].

sure mass expectation values for the flavor eigenstates). It is also experimentally unknown if neutrinos are their own anti-particles. These details do not substantially alter collider physics, and for the purpose of this thesis neutrinos will be considered massless, and as having anti-particles denoted by $\bar{\nu}_e$, $\bar{\nu}_\mu$, and $\bar{\nu}_\tau$. All leptons are subject to the weak force.

Quarks: Each generation of quarks has two types (or flavors) of quarks, with fractional charges $+\frac{2}{3}e$ and $-\frac{1}{3}e$. The positively (negatively) charged quarks are whimsically named up (down), charm (strange), and top (bottom), in order of increasing mass. Each of these possesses strong charge, which comes in three colors, often denoted red, green, and blue. As with electric charge, each of these can be positive or negative (negative color charge often referred to as anti-color). Bound states of quarks are either baryons, containing equal amounts of all color charge (the proton, made of two up quarks and a down quark), or mesons, containing a quark and an anti-quark with the same color/anti-color, which leaves the composite with zero net color. Quarks are also charged under weak and electromagnetic interactions.

Force Carriers: In quantum field theory, every force can be thought of as mediated by the exchange of virtual force carrier bosons. Virtual particles have the same characteristics as a usual particle, except that they have a mass that violates the energy-momentum relationship of special relativity: $E^2 - p^2c^2 = m^2c^4$. This is a consequence of the energy momentum uncertainty principle, as the duration of existence of the boson and its energy cannot both be known precisely. However, a complete interaction does always conserve energy and momentum.

Evidence for the quantization of electromagnetic radiation, including the photoelectric effect, lead to the discovery of the first known force carrier, the photon. This in turn lead to the development of the first quantum field theory. Quantum electrodynamics was considered a fantastic success due to its predictions of quantities such as the anomalous magnetic moment of the electron. The photon is massless, which leads electromagnetism to be a long range force (like gravity). Most of the forces we experience in our every day existence are electromagnetic in nature.

While the weak force is technically derived from the same symmetry group as electromagnetism, it's observable form is very different in nature. It has two charged force carriers ($W^{\pm}$) and a neutral force carrier (Z). The W (Z) boson has a mass of 80.39 (91.19) GeV. Due to this rest mass, the weak force is short range and rather feeble at the accessible energies (hence its name). In fact, contributions to forces due to the Z boson are very difficult to measure, because in most cases the interaction is also mediated by the much more substantial strong and electromagnetic forces. Neutrino scattering, which is notoriously difficult to detect, and resonant production are the only realistic detection methods. The $W^{\pm}$ by contrast, has the unique ability that it does not conserve the "flavor" of the fermion with which it interacts. This produces the weak force's most visible signature: nuclear beta decay, in which a neutron decays into a proton, a neutrino, and an electron, as well as allowing quark mixing and CP violation, discussed in sections 1.3 and 1.4.

The aptly named strong force is responsible for binding quarks into hadrons, and its residual force in the nucleus binds together protons and neutrons. This force is mediated by the gluon, which is massless like the photon, but unlike the photon, is charged under color interactions. Due to this gluons interact with other gluons, and in fact, interact with themselves, and this drastically changes the nature of their interactions. Due to this self interaction, a calculational problem occurs. Typically, perturbative calculations in quantum field theories are made by taking the simplest transition from one state to another as the "lowest order" calculation, and corrections are calculated by including diagrams with more interactions. However, in quantum chromodynamics, these higher order corrections from these diagrams can in some cases be just as large or larger than the lower order terms. The strength of the strong force can only be calculated for small momentum transfer compared to the QCD scale

(Λ_s):

$$\alpha_s(q^2) \propto \frac{1}{\ln(q^2/\Lambda_s^2)} \quad (\text{for } |q^2| \gg \Lambda_s^2) \ , \tag{1.1}$$

where q^2 represents the square of the gluons momentum four vector, and α_s is the strong coupling constant. This equation captures two fundamental characteristics of Quantum Chromodynamics: confinement and asymptotic freedom. At low momentum (corresponding to large distance), the magnitude of the strong force increases without bound. Therefore the amount of energy required to separate a quark from a nucleon is larger than the amount required to produce a new quark anti-quark pair, and so quarks can not be isolated from color neutral arrangements. This phenomenon is termed confinement, as quarks do not exist in a "free" state. Conversely, at high momentum and low distance, the strong force becomes very weak (asymptotic freedom), and perturbation theory can be used in this regime. The computational challenges associated with Quantum Chromodynamics will not be discussed in detail in this dissertation, but its effect on simulation of the ATLAS experiment is discussed in section 1.9.

1.2 Electroweak Symmetry Breaking: The Higgs Mechanism

Electroweak theory developed over many decades, with contributors including Fermi, Lee and Yang, Feynman, and Gell-Mann, but it was put into its modern form in the 1960's by Abdus Salam, Sheldon Glashow and Steven Weinberg. In its unbroken form, it is based on a U(1) weak hypercharge and SU(2) weak isospin symmetries, to produce the following Lagrangian, separated into a gauge term and a fermionic term:

$$L_{WS} = L_G + L_F, \tag{1.2}$$

$$L_G = -\tfrac{1}{4} F_i^{\mu\nu} F_{\mu\nu}^i - \tfrac{1}{4} B^{\mu\nu} B_{\mu\nu}, \tag{1.3}$$

$$L_F = \sum_{\psi_L} \bar{\psi}_L i \not{D} \psi_L + \sum_{\psi_R} \bar{\psi}_R i \not{D} \psi_R, \tag{1.4}$$

where $F_{\mu\nu}^i$ and $B_{\mu\nu}$ are the SU(2) and U(1) field strengths:

$$F_{\mu\nu}^i = \partial_\mu W_\nu^i - \partial_\nu W_\mu^i - g_2 \epsilon^{ijk} W_\mu^j W_\nu^k, \tag{1.5}$$

$$B_{\mu\nu} = \partial_\mu B_\nu - \partial_\nu B_\mu, \tag{1.6}$$

where B_μ and $\vec{W}_\mu = (W_\mu^1, W_\mu^2, W_\mu^3)$ represent the weak hypercharge and the weak isospin fields, and D_μ is the covariant derivative of the theory:

$$D_\mu \phi = (\mathbf{I}(\partial_\mu + i\frac{g_1}{2} B_\mu) + ig_2 \frac{\tilde{\tau}}{2} \cdot \vec{W}_\mu)\phi. \tag{1.7}$$

The covariant derivative is the ordinary derivative modified in such a way as to make it behave like a true vector operator, so that equations written using the covariant derivative preserve their physical properties under gauge transformations defined by the symmetries underlying our theory. The subscripts L and R specify left and right handed chiralities, as right handed chiral fermions do not couple to weak isospin. The constants g_1 and g_2 are the U(1) and SU(2) coupling constants.

The trouble is, that this Lagrangian describes massless gauge bosons, as well as massless fermions. Even during the development of electroweak theory, the weak bosons were expected to be massive, due to the weakness of the force, and fermionic masses had obviously been observed as well. Adding a boson mass term of the form $\frac{1}{2} M B_\mu B^\mu$ leaves the theory no longer invariant under the gauge symmetries we based our theory on. This is theoretically distasteful, as the original motivation for this approach was to describe the electroweak sector using a small number of symmetries; the

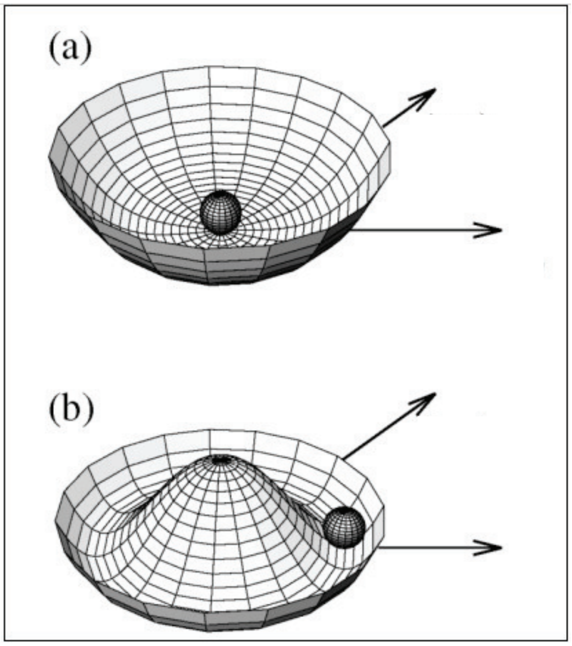

Figure 1.2. The shape of the potential described by equation 1.8, for $\mu^2 > 0$ (a), and $\mu^2 < 0$ (b). Image taken from Ref. [3].

original Lagrangian includes terms consistent with the gauge symmetry postulated, and nothing more.

The typical solution to this conundrum involves the introduction of the Higgs Mechanism [12], in which a complex scalar field, coupled to our theory, generates a vacuum expectation value, leading to a ground state which is not symmetric under our original symmetries, while still preserving the symmetries in the interactions of the theory. The most general Lagrangian for a complex scalar ϕ that obeys our gauge symmetries is the following:

$$L = (D_\mu\phi)^\dagger(D_\mu\phi) - V = (D_\mu\phi)^\dagger(D_\mu\phi) - \mu^2\phi^\dagger\phi - \tfrac{1}{4}(\phi^\dagger\phi) \tag{1.8}$$

where the first term is a kinetic term, with D_μ is again the covariant derivative.

Figure 1.2 shows the form of the potential V(ϕ) for $\mu^2 < 0$ and $\mu^2 > 0$. As can be seen, for $\mu^2 < 0$, ϕ has a ground state not at zero, and gains a vacuum expectation value. If one expands the Lagrangian around this expectation value, to first order, the following term is observed:

$$L_m = \tfrac{1}{2} V_\mu M^2 V^\mu, \tag{1.9}$$

where V_μ is the vector of the boson fields for isospin and hypercharge $V_\mu \equiv (W^1_\mu, W^2_\mu, W^3_\mu, B_\mu)$, and M^2 is a matrix which can be interpreted as the masses of those fields, with the following terms:

$$M^2 = \frac{v^2}{4} \begin{pmatrix} g_2^2 & 0 & 0 & 0 \\ 0 & g_2^2 & 0 & 0 \\ 0 & 0 & g_2^2 & -g_1 g_2 \\ 0 & 0 & -g_1 g_2 & g_1^2 \end{pmatrix} \tag{1.10}$$

When this mass matrix is diagonalized, it produces a massless electromagnetic boson, and 3 massive weak bosons, as are observed in nature. This mixing of the bosons produces different masses for the $W^\pm$ and Z electroweak bosons:

$$M_W = \frac{v}{2} g_2, \; M_Z = \frac{v}{2} \sqrt{g_1^2 + g_2^2}. \tag{1.11}$$

The mixing between isospin and hypercharge sectors can be thought of as a rotation of angle θ_W, which is an important input parameter to the Standard Model, and defines the ratio of boson masses:

$$\tan \theta_W = \frac{g_1}{g_2}, \; \cos \theta_W = \frac{M_W}{M_Z}. \tag{1.12}$$

In the Standard Model masses for the leptons and quarks are also produced by coupling to the Higgs Field ϕ.

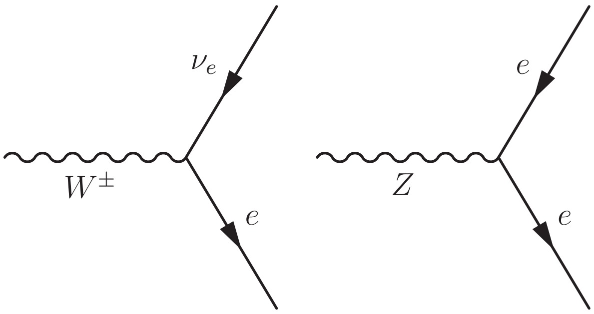

Figure 1.3. Charged (left) and neutral (right) weak interaction Feynman diagrams.

1.3 Parity and Electroweak Interactions

While not all fermions have electromagnetic charge, all of them participate in weak interactions. Figure 1.3 shows the basic charged (W) and neutral (Z) weak interactions for leptons. In leptonic interactions, lepton number is conserved for each generation, where each neutrino carries the same lepton number as its corresponding muon/electron/tau. A muon cannot simply decay into an electron and a Z boson.

In the 1950's, the weak interaction was initially assumed to conserve parity, which is equivalent to the invariance of the theory under spatial inversion. This inversion switches the spin direction of all particles in an interaction. At this time the strong and electromagnetic forces had been found to obey parity symmetries, so it was suspected to be a universal symmetry. However, it was observed in 1956 that the K^+ meson decayed to both an even parity state ($\pi^+\pi^+\pi^-$) and an odd parity state ($\pi^+\pi^0$), in violation of parity symmetry (Lee and Mills). Direct experiments on beta decay in Cobalt-60 by C.S. Wu made a startling discovery. Not only does the weak interaction violate parity, but it violates it "maximally". Weak interactions only couple to left handed fermions (and right handed anti-fermions). This interaction can be described by the following current (for a muon transitioning to a muon neutrino and a W boson):

$$J^{\mu} = \bar{\psi}_{\mu}\gamma^{\mu}(1-\gamma^{5})\psi_{\nu}. \tag{1.13}$$

The combined symmetry of charge and parity inversion (CP), is much closer to being a symmetry of the weak interaction, but is violated to a very small degree. CP violation is very carefully studied, because it is often used to formulate theories by which a matter/antimatter imbalance could occur in the early universe. Without this violation, models predict the nearly complete annihilation of matter and antimatter, leaving only radiation in our present day universe.

1.4 Quark Mixing and CP Violation

It is tempting to assume that weak interactions of quarks would not change flavor, and that each generation of quarks would have its flavor individually conserved. However, were this true, many observed decays of strange mesons, such as the decay of the lambda ($\Lambda \rightarrow p^{+} + \pi^{-}$) would be forbidden. Instead it turns out that the quark generations have a different eigenbasis under the weak interaction than they have in the strong basis. Cabibbo first suggested this solution in 1963, and it was later applied by Glashow, Illioopoulos and Maiani (GIM) and extended to three quark generations by Kobayashi and Maskawa (KM).

We now know this mixing matrix as the CKM-matrix (Cabbibo, Kobayashi and Maskawa):

$$\begin{pmatrix} d' \\ s' \\ b' \end{pmatrix} = \begin{pmatrix} V_{ud} & V_{us} & V_{ub} \\ V_{cd} & V_{cs} & V_{cb} \\ V_{td} & V_{ts} & V_{tb} \end{pmatrix} \begin{pmatrix} d \\ s \\ b \end{pmatrix} \tag{1.14}$$

in which the weak force couples the pairs (u,d'), (c,s'), and (t,b'), instead of the eigenstates of the strong force, where d',s' and b' are the weak eigenstates, and no prime specifies the physical quarks. This matrix is mostly diagonal, but because off diagonal elements are not zero, there are transitions between quark generations. The elements of the CKM matrix are fundamental elements of the Standard Model, and can only be determined from experiment.

If two generations of quarks are assumed, the matrix allows no CP violating phases. At the time of the development of the Standard Model, CP violation had already been observed in neutral kaon decays in 1964. This observation lead to the observation in 1973 by Kobayashi and Maskawa that there must be three generations of quarks[13].

1.5 The Standard Model Lagrange Density

We now have all the pieces to present the full Standard Model Lagrange Density, after electroweak symmetry breaking and including quark mixing. Fermion/boson interactions, which were not treated in Section 1.2 are properly included here. The Higgs field is not included explicitly.

$$\mathcal{L}_{SM} = \mathcal{L}_{Dirac} + \mathcal{L}_{mass} + \mathcal{L}_{gauge} + \mathcal{L}_{int}. \tag{1.15}$$

Here,

$$\mathcal{L}_{Dirac} = i\bar{e}^i_L \not{\partial} e^i_L + i\bar{\nu}^i_L \not{\partial} \nu^i_L + i\bar{e}^i_R \not{\partial} e^i_R + i\bar{u}^i_L \not{\partial} u^i_L + i\bar{d}^i_L \not{\partial} d^i_L + i\bar{u}^i_R \not{\partial} u^i_R + i\bar{d}^i_R \not{\partial} d^i_R; \tag{1.16}$$

$$\mathcal{L}_{mass} = -v(\lambda^i_e \bar{e}^i_L e^i_R + \lambda^i_u \bar{u}^i_L u^i_R + \lambda^i_d \bar{d}^i_L d^i_R + h.c.) - M_W^2 W^+_\mu W^{-\mu} - \frac{M_W^2}{2\cos^2\theta_W} Z_\mu Z^\mu; \tag{1.17}$$

$$\mathcal{L}_{gauge} = -\frac{1}{4}(G^a_{\mu\nu})^2 - \frac{1}{2} W^+_{\mu\nu} W^{-\mu\nu} - \frac{1}{4} Z_{\mu\nu} Z^{\mu\nu} - \frac{1}{4} F_{\mu\nu} F^{\mu\nu} + \mathcal{L}_{WZA}, \tag{1.18}$$

where

$$G^a_{\mu\nu} = \partial_\mu A^a_\nu - \partial_\nu A^a_\mu - g_3 f^{abc} A^b_\mu A^c_\nu \tag{1.19}$$

$$W^\pm_{\mu\nu} = \partial_\mu W^\pm_\nu - \partial_\nu W^\pm_\mu \tag{1.20}$$

$$Z_{\mu\nu} = \partial_\mu Z_\nu - \partial_\nu Z_\mu \tag{1.21}$$

$$F_{\mu\nu} = \partial_\mu A_\nu - \partial_\nu A_\mu, \tag{1.22}$$

and

$$\mathcal{L}_{int} = -g_3 A^a_\mu J^{\mu a}_{(3)} - g_2(W^+_\mu J^\mu_{W^+} + W^-_\mu J^\mu_{W^-} + Z_\mu J^\mu_Z) - g_1 \cos\theta_W A_\mu J^\mu_A. \tag{1.23}$$

The i denotes generation, with e^i representing the field for one of electron/muon/tau. Similarly u^i represents up/charm/top and d^i represents down/strange/bottom. Repeated indices are summed over. The fields $G^a_{\mu\nu}$, $W^\pm_{\mu\nu}$, $z_{\mu\nu}$, and $F_{\mu\nu}$ are those associated with gluons, $W^\pm$ bosons, Z bosons, and the photon, which are then expressed in terms of their potentials. The indices a/b/c represent a particular color, with f^{abc} representing the structure constants for SU(3), and g_3 representing the coupling constant for SU(3) (QCD). The term $\mathcal{L}_{WZA}$ includes triple and quadruple gauge field coupling terms, which are important for higher orders of perturbation theory, but will not be discussed here.

The interaction term $\mathcal{L}_{int}$ is specified in terms of the following current densities for each of the gauge fields:

$$J^{\mu a}_{(3)} = \bar{u}^i \gamma^\mu T^a_{(3)} u^i + \bar{d}^i \gamma^\mu T^a_{(3)} d^i \tag{1.24}$$

$$J^\mu_{W^+} = \frac{1}{\sqrt{2}}(\bar{\nu}^i_L \gamma^\mu e^i_L + V^{ij} \bar{u}^i_L \gamma^\mu d^j_L) \tag{1.25}$$

$$J^\mu_{W^-} = (J^\mu_{W^+})^* \tag{1.26}$$

$$J^\mu_Z = \frac{1}{\cos\theta_W}[\frac{1}{2}\bar{\nu}^i_L \gamma^\mu \nu^i_L + (-\frac{1}{2} + \sin^2\theta_W)\bar{e}^i_L \gamma^\mu e^i_L + (\sin^2\theta_W)\bar{e}^i_R \gamma^\mu e^i_R \tag{1.27}$$

$$+ (\frac{1}{2} - \frac{2}{3}\sin^2\theta_W)\bar{u}^i_L \gamma^\mu u^i_L + (-\frac{2}{3}\sin^2\theta_W)\bar{u}^i_R \gamma^\mu u^i_R \tag{1.28}$$

$$+ (-\frac{1}{2} + \frac{1}{3}\sin^2\theta_W)\bar{d}^i_L \gamma^\mu d^i_L + (\frac{1}{3}\sin^2\theta_W)\bar{d}^i_R \gamma^\mu d^i_R] \tag{1.29}$$

$$J^\mu_A = (-1)\bar{e}^i \gamma^\mu e^i + (\frac{2}{3})\bar{u}^i \gamma^\mu u^i + (-\frac{1}{3})\bar{d}^i \gamma^\mu d^i. \tag{1.30}$$

$$\tag{1.31}$$

The matrices $T^a_{(3)}$ represent the generators of the SU(3) group. As discussed in the previous section the V_{ij} are elements of the CKM matrix describing mixing between different generations of quarks.

1.6 R as a Probe of the Standard Model

Measurement of R can be used to extract useful information about the Standard Model. The inclusive R measurement can be written as:

$$R = \frac{\sigma_W}{\sigma_Z} \frac{\Gamma(W \to \ell\nu)}{\Gamma(Z \to \ell\ell)} \frac{\Gamma(Z)}{\Gamma(W)} \tag{1.32}$$

where Γ refers to decay width/rate, and σ to cross section. The overall cross sections can be predicted from the boson couplings combined with knowledge of proton structure. The decay widths of the Z boson have been carefully measured at LEP [14]. This gives sufficient information to determine the branching ratio $BR(W \to \ell\nu) = \Gamma(W \to \ell\nu)/\Gamma(W)$, which also allows an indirect measure of $\Gamma(W)$, using the SM prediction for $\Gamma(W \to \ell\nu)$. The W width depends on the quark couplings, and can thus provide a constraint on these terms in the CKM Matrix. The Tevatron has used this method to determine V_{cs}, which is the least well constrained matrix element [8]. In addition, precise measurements at the higher energy of the LHC can potentially provide constraints on Parton Distribution Functions, described in Section 1.9

1.7 Open Physics Questions in the Standard Model Era

While the Standard Model has predicted experimented results with unprecedented success, the theory suffers from some perplexing characteristics, for example, the large unexplained difference between Electroweak Scale and the Gravitational Scale. As discussed above, the explanation for electroweak symmetry breaking is the most important open question in the Standard Model, as the theory is incomplete without its inclusion. The following are interesting questions that the Standard Model does not adequately address:

The Hierarchy Problem: Intuitively, one would expect loop corrections to the Higgs Boson to pull its mass towards the Plank scale, and fine tuning of parameters is needed to keep that mass at the Electroweak scale. This problem relates to physicists' desire to find a unified description of known forces and gravity, specifically General Relativity. A computationally tractable theory that can unify gravity and the Standard Model has not been achieved, due to difficulties that arise in calculations at small length scales and high energy densities.

Vacuum Expectation / Cosmological Constant: Computations of the quantum vacuum in quantum field theory predict very large vacuum energy. For theoretical reasons, this vacuum energy is often identified with the cosmological constant, a term used to explain the increasing rate of expansion of the universe. This identification produces a prediction for the vacuum that is many orders of magnitude too small. The cosmological constant is also termed "Dark Energy" and describes an energy term for the universe that does not dilute during an expanding universe. The Standard Model gives no insight into this problem.

Dark Matter: As observed by Zwicky in the mid 1930's, it has been clear that the amount of gravitation mass in galaxies, predicted by the movements of their constituents, does not match the amount of matter predicted from luminous matter contained in stars, gas and dust [15]. The hypothesis of gravitationally interacting but non-luminous matter has been termed "Dark Matter". Even stronger evidence for this unexplained form of matter has come from gravitational lensing, as dark matter concentrations can be mapped by their effect of bending the light of distant stars. In 2006, gravitational lensing was used to track a collision of two galaxy clusters in the Bullet Cluster. The luminous mass in the collision was shown to slow down, while the non-luminous matter was observed to pass through without this deceleration [16]. This is considered direct evidence for Dark Matter. Many hypotheses for dark matter involve new weakly interacting particles that could be produced at particle colliders such as the LHC. These would observed as unexplained "Missing Energy" in the detector, which will be explained further in Section 2.3.4.

Other Questions: The Standard Model does not explain why there are three generations of particles, or why these generations have the same hierarchical structure for the quark and lepton sectors. It also does not explain why the strong force respects CP symmetry, while the weak force does not. There is no theoretical explanation in the Standard Model for the terms of the CKM matrix, the weak mixing angle, or any of the other free parameters of the model, and many physicists would find it satisfying to find a deeper physical explanation for their structure. These questions are especially interesting because the input parameters of the Standard Model affect both molecular structure and the formation of stars and solar systems, both necessary for life as we know it. There are also cosmological questions about the observed imbalance of particles and anti-particles in our universe, which is difficult to explain with the very small CP violation present in the Standard Model.

1.8 Supersymmetry, and R_{jet} as a Probe for New Physics

Supersymmetry (SUSY) is a new physics theory that resolves hierarchy/fine-tuning issues in the Standard Model, and provides a dark matter candidate, as well as being a necessary component of a number of Grand Unified Theories(GUTs), such as String Theory. SUSY is defined by an additional symmetry on top of the Standard Model, specifically between bosonic and fermionic spin states. This symmetry leads to the existence of a supersymmetric partner for every Standard Model particle, with all characteristics identical except possessing the opposite type of spin statistics. Due to the lack of experimental observation of these superpartners, the mass equivalence between superpartners must be disrupted by one of a variety of possible symmetry breaking scenarios. Despite SUSY's advantages, this symmetry breaking leaves unconstrained SUSY models with a large number of free parameters. For example, the Minimal Supersymmetric Standard Model (MSSM), when soft symmetry breaking terms are included, has 150 free parameters.

Minimal Supergravity, or mSUGRA, is a variety of SUSY in which coupling to gravity breaks the symmetry between supersymmetric partners. It makes two additional assumptions: first, soft supersymmetry breaking universality, which is motivated by experimental constraints and requires among other things that no complex phases are introduced by the symmetry breaking terms. The second is the unification of forces at the Plank Scale. While these assumptions are only weakly justified, these constraints reduce the theory to only five free parameters. This provides a useful way to explore the phenomenology of SUSY without having to explicitly deal with 100's of parameters.

mSUGRA is presented here because it is typical of models which could differentially affect W and Z measurement channels. In mSUGRA, as in most realizations of SUSY, the lightest supersymmetric particle (LSP) must be chargeless, flavorless, and stable (due to cosmological and other constraints). SUSY events at the LHC would most likely involve cascade decays of up and down squarks into lighter sparticles (s signifying a SUSY partner). The second lightest SUSY particle strongly influences the phenomenology of the event. For example, a light stau could only decay into a tau and an LSP, which would produce events in the lepton + MET + jets channel [17]. The proposed measurement could be sensitive to any physics model which has large jet $\sum |E_T|$ and preferentially produces lepton + MET or dilepton signals, an additional example being 4th generation quark models [18], though this has been ruled out by the recent Higgs candidate measurement.

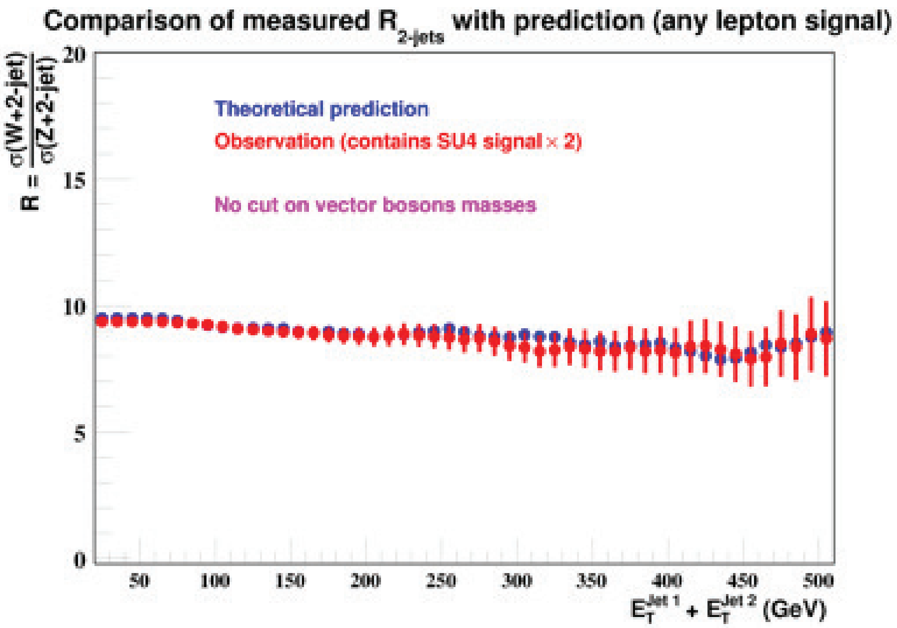

Figure 1.4. R_{jet} as function of scalar sum $p_{\mathrm{T}}$of jets, for exactly two jets, shown for theory, and reconstructed result including SU4 new physics signal. No selection is made on the boson mass for the W or Z boson.

This section presents a very simple Monte Carlo study to show how new physics could appear in the R_{jet} result. This study compares theoretical prediction for R_{jet} with an "observed result" containing an SU4 signal, which is a specific set of mSUGRA parameters representative of a phenomenology with a high branching fraction to leptons. The study examines R_{jet} for exactly two 30 GeV jets, as a function of the scalar sum of the p_{T} of the two jets. The "observed result" is corrected back to the theoretical level using a simple bin-by-bin acceptance correction. Only W and Z signal are included, and no backgrounds are included. Obviously this is an idealized situation, but gives a flavor of how a deviation in R_{jet} could appear. The study assumes 200 pb^{-1} of integrated luminosity at 10 TeVcenter of mass energy.

Two interesting questions present themselves when considering new physics in R_{jet}:

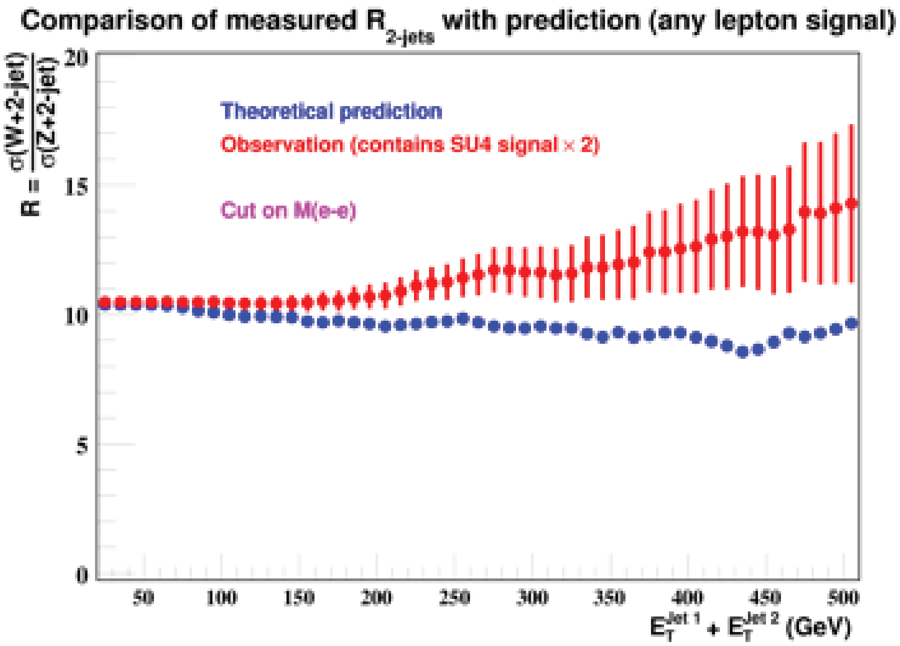

Figure 1.5. R_{jet} as function of scalar sum $p_{\text{T}}$of jets, for exactly two jets, shown for theory, and reconstructed result including SU4 new physics signal. An upper limit is placed on the Z invariant mass, but no upper limit is placed on the transverse mass of the W.

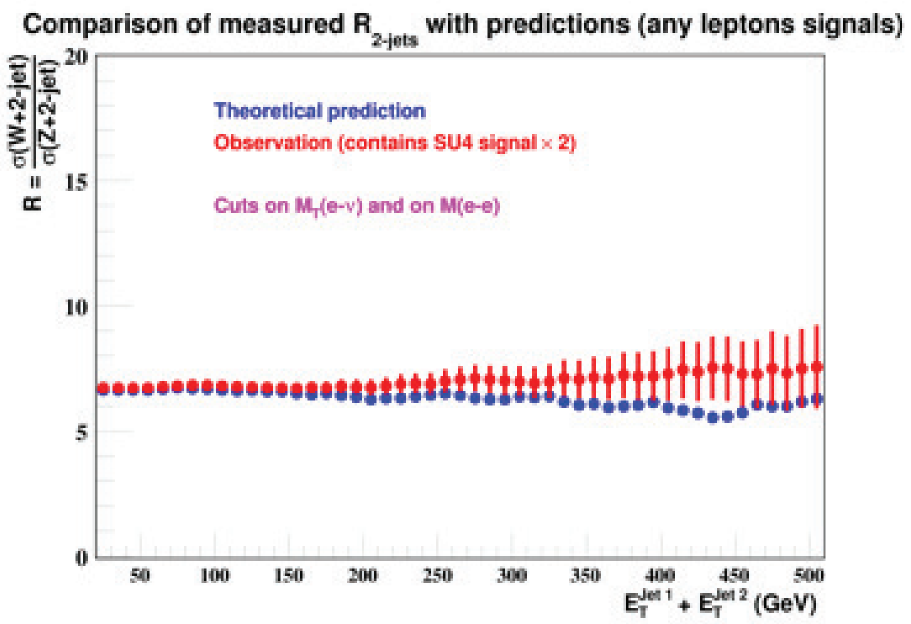

Figure 1.6. R_{jet} as function of scalar sum $p_{\text{T}}$of jets, for exactly two jets, shown for theory, and reconstructed result including SU4 new physics signal. An upper mass selection is applied to both the W and the Z boson.

1. If there is a deviation, how do we know it is from new physics, and not mis-modeling of known physics?
2. Could new physics contribute to both the W and Z channels equally such as to mask the signal in R_{jet}?

One tool to elucidate these questions is invariant and transverse mass cuts on the bosons. Removing low mass events is required to reduce known backgrounds. Selections rejecting high mass events in practice reduce the contribution from higher energy processes, serving to cut out new physics. Figure 1.4 shows the R_{jet} comparison between theory and observation in the case where no mass cuts are applied to the bosons. In this case, there is little deviation of R_{jet}, due to signal presence in both channels. As shown in figure 1.5, this can be remedied by applying an upper mass selection on one or the other channel. In these studies, an upper mass selection signifies restricting either the invariant mass or transverse mass to smaller than 100

GeV. This strategy can also be used to validate a deviation seen, as if a deviation is seen in R_{jet}, if it is really a new physics signal, applying an upper mass selection to both the W and Z should reduce or eliminate this deviation, as shown in figure 1.6.

1.9 Collider Physics and Monte Carlo Simulation

While a proton can undoubtedly be thought of as a composite of three quarks (uud), when two protons collide, the process is much more complex than this, due to the nature of quantum field theory. Quarks are constantly radiating and reabsorbing virtual particles, affecting the details of both their bound state and their collisions with other particles. So not only do the valence (uud) quarks play a part in the collision, but the "sea" of virtual quark/anti-quark pairs ($q\bar{q}$) and gluons do as well. In practice this is modeled by "Parton Distribution Functions" (PDFs) which model the probability that a given "parton" will have a given fraction of the proton momentum. These PDFs are a function of the momentum transfer in a given collision.

Factorization is the statement that the cross section of deep inelastic scattering processes can be written as the product of a hard scattering cross section that can be calculated perturbatively, and non-perturbative PDFs previously mentioned. Lower energy internal gluon "ladder terms" are factored with corrections to the PDF, while higher energy gluon terms contribute to cross section. The cutoff between these two scales is termed the factorization scale. This and the renormalization scale are taken as empirical parameters in most simulation programs. For a thorough treatment of QCD in Deep Inelastic Scattering, including renormalization and theoretical techniques associated with the "Improved Parton Model", see Ref. [19].

Two main programs can be used by ATLAS to generate PDF sets: MSTW (formerly MRST) [20] and CTEQ [21]. These programs can both model the proton structure at 1st, 2nd and 3rd order in perturbation theory. These structures cannot be predicted from first principles, but instead are tuned based on data from deep inelastic scattering experiments, as well as hadronic colliders such as the Tevatron and the LHC.

A proton-proton collision event is a very chaotic interaction. While the hard scatter between two (or more) partons produces many of the high momentum objects in a collision, modeling physics processes correctly requires understanding all of the following aspects of particle collisions:

1. A hard scatter occurs between two of the partons in the collision, as determined by their PDFs. Matrix elements are used to predict the cross section for a number of Feynman diagrams to a given order, such as leading order (LO) or to next to leading order (NLO). Parton showering algorithms are often used to approximate the production of complex states that the matrix element calculation does not include. In these cases, some type of matching or combination must be performed between the matrix element and parton shower results.

2. If a short lived particle such as a W or Z boson is produced, conservation of quantum numbers (such as spin correlations) must be preserved in the transition from the production process to the decay stages.

3. Initial State Radiation (ISR): As a collision implies accelerated color and electromagnetic charges, Bremsstrahlung (deceleration radiation) can occur. This process cannot be predicted from first principles, but can be approximated by parton shower algorithms.

4. Final State Radiation (FSR): Interactions of outgoing particles can also produce radiation, also often modeled using parton showers. ISR is typically modeled with space-like parton showers, and FSR with time-like parton showers. Often the distinction between ISR, FSR, and the hard scattering process is ambiguous.

5. Multiple Collisions: More than one parton pair can collide during a hard scatter, each with its own ISR and FSR.

6. Beam Remnants: The partons not involved in the collision carry off the energy not lost to the hard scatter, mostly undeflected. These remnants also compensate for the color taken away by the outgoing partons.

7. Color Fields: Due to the principle of the asymptotic freedom, shortly after the collision when partons are close, they can be considered as free particles. However, as the partons recede from each other, this is no longer true. Because quantum chromodynamics involve strongly coupled dynamics, we have no computational description of this process based on first principles. Instead a variety of phenomenological models are used.

8. Hadronization: As a part of this process the potential energy of these fields can produce new quark anti-quark pairs, which then associate either to the remnants or collision partons to form baryons and mesons. Two common models for color interactions and hadronization exist:

    - Color String Models: The quarks left after the parton showering are “strung” together to form colorless states, which can either snap and produce more quarks or remain as final underlying event particles.
    - Cluster Models: Gluons are converted into quark anti-quark or diquark anti-diquark pairs. The quarks are then grouped into colorless states based on preconfinment, i.e. states with low mass and low spatial extent are favored. These colorless groupings then have a series of phenomenological rules to decay to SM particles.

9. Detector Response: Many of these hadrons are unstable and decay further, but most do so on a time scale that is observable in our detector, and so at this point the event generation framework must be linked to a detector simulation, which models all details of further decay within the detector, and the detector’s

response. This final step should produce output that can be reconstructed in an identical way as detector data, to interpret what physical phenomenon was happening in the given event. The interaction of decay products with detector is modeled in ATLAS using the Geant4 [22] toolkit.

The Monte Carlo programs used to simulate these processes vary from very general to very specific. Because of the breadth of the process to be modeled, the more specific programs are often used as "plug-ins" by the more general programs, in order to for example treat matrix elements of specific process or model the hadronization process. The follow generators were used in this thesis:

- Alpgen [23] is the generator mostly widely used for signal samples in this thesis, as it uses exact tree level matrix calculations for the hard scattering process involving a boson plus up to 5 additional partons in the event. Additional partons must be modeled with a showering processes. Alpgen is significant for its matching procedure, which weights the matrix element with Sudakov form factors to suppress the result in regions of phase space where parton showering dominates, as well as employing an explicit veto of parton showering in regions of phase space covered by the matrix element result. As Alpgen is a somewhat specialized generator, it does not calculate parton showering and hadronization, but instead uses Herwig to do so (see below). Jimmy is used to model multi-parton interactions and the underlying event produced by the beam remnant[24].

- Sherpa [25] is also used widely in this thesis, primarily as a cross check to Alpgen, as both generators are tree level generators with the ability to model the exact matrix elements of multi-parton interactions. A conceptually similar matching scheme to Alpgen is used. Sherpa has internal modules for parton showering, hadronization, and underlying event. Parton showering is done using a virtuality-ordered approach (particles farther off shell emit their radiation first). Hadronization is performed using a phenomenological cluster-hadronization model.

- BlackHat [26] is a tool kit for providing NLO QCD matrix element calculations. In our case it is used in conjunction with Sherpa which provides the showering capabilities and matching scheme. BlackHat+Sherpa is used in this thesis for our best theoretical prediction of R_{jet} distributions, as they include one loop theoretical contributions (NLO), and include less tunable parameters, due to not relying on showering algorithms. These predictions are only provided at born level (before radiation and hadronization). As described later in Section 3.11, Alpgen is used to calculate the small correction factors to take these effects into account and allow comparison to our measured result.

- Pythia [27] is a general event generator package that handles all hard scattering at leading-order, as well as computes parton showering and hadronization. For W and Z production, it uses matrix element calculation for the computation of the boson plus up to one additional parton in the event. Pythia uses parton showering for addition jet hadronic states. For this reason, Pythia is not used for the predictions of this thesis, but is mentioned because of its use in performance studies to determine quantities such as trigger and muon reconstruction efficiencies. For its showering, a momentum-ordered approach is used (gluons and photons are emitted with softer and softer momentum as the shower evolves).

  Pythia uses a string model for hadronization. While Pythia also handles ISR and FSR, for Drell Yan processes at ATLAS, FSR of photons is handled by a separate package photos [28], which implements all leading-order QED radiative corrections to Z/γ^* decays.

- The HERWIG (Hadron Emission Reactions With Interfering Gluons) package [29] is also a full event generator. The parton showering proceeds with an angular ordering (this is similar but not identical to p_T ordering, as higher momentum radiation tends to be emitted at a larger angle).

- The JIMMY [24] package describes multi-parton interactions using cluster parton showering.

- MC@NLO [30] generates hard scatters to NLO accuracy. The kinematic information from the hard scatter is then fed to the HERWIG program.

Further details of the simulation samples used in this thesis will be discussed in Chapter 3.

CHAPTER 2

THE ATLAS EXPERIMENT AT THE LHC

The Large Hadron Collider (LHC) [31, 32] is a synchrotron accelerator and hadron collider operated by the European Organization for Nuclear Research (CERN). It is the first collider to explore physics at the TeV scale, and has been producing proton-proton collisions at a center of mass energy ($\sqrt{s}$) of 7 TeV in 2010-2011 and 8 TeV in 2012, with an ultimate design energy of $\sqrt{s} = 14$ TeV. The primary goals of the LHC include Standard Model (SM) measurements, searches for the Higgs Boson to explain Electroweak Symmetry Breaking, and searches for other novel physics motivated by questions not addressed by the SM. The LHC also has a program of lead ion collisions central to its mission but not discussed in this thesis. Four major experiments are located along the LHC beam pipe: ATLAS (A Large Toroidal LHC ApparatuS) [33] and CMS (Compact Muon Solenoid) are all-purpose detectors designed to be used for a wide variety of SM measurements and new physics searches. ALICE (A Large Ion Collision Experiment) is a detector designed to examine heavy ion collisions (pb-pb), in order to study strongly interacting states of matter, most notably the quark-gluon plasma. LHCb is a B-physics experiment studying CP-violation in the quark sector.

2.1 The Large Hadron Collider

The LHC synchrotron is located in the 26.7 km circumference tunnel formerly used for the Large Electron Positron Collider (LEP) [34], housed in CERNs accelerator complex located at the Swiss-French border near Geneva [35] (Fig.2.1). The acceleration is performed in several stages. Hydrogen atoms are ionized and the

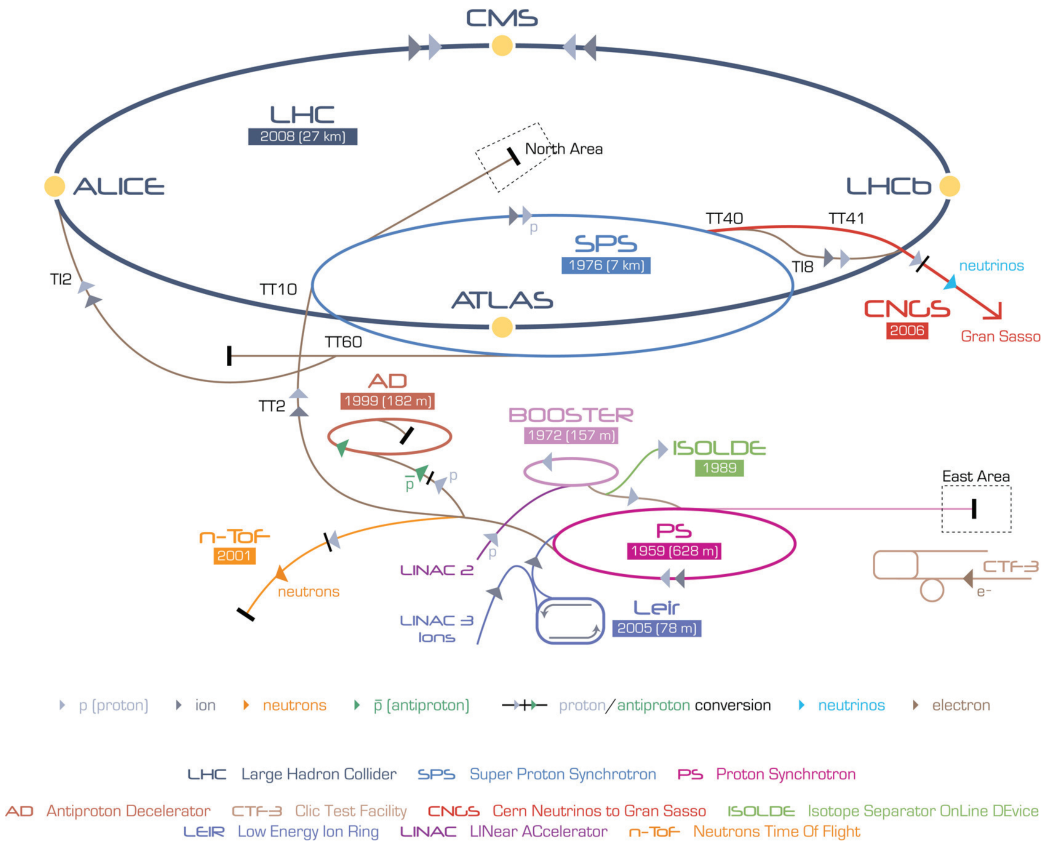

Figure 2.1. The CERN accelerator complex.

protons are separated using a duoplasmatron [36]. These protons are accelerated, first using a linear accelerator and then they are injected sequentially into two synchrotrons: the Proton Synchrotron (PS) and the Super Proton Synchrotron (SPS). In the SPS the protons are accelerated to an energy of 450 GeV before they are injected into the LHC ring, where the acceleration continues until the protons reach their final energy (3.5 TeV for 2011 running). The beam line is equipped with 1232 superconducting dipole bending magnets each generating an 8 Tesla magnetic field. Hundreds of additional magnets are installed to focus the beam.

The two proton beams collide at four interaction points along the LHC beam line. The beams are produced with a bunch structure. Typical beam parameters for the end of 2011 running are 1033 bunches with a 50 ns spacing between bunches.

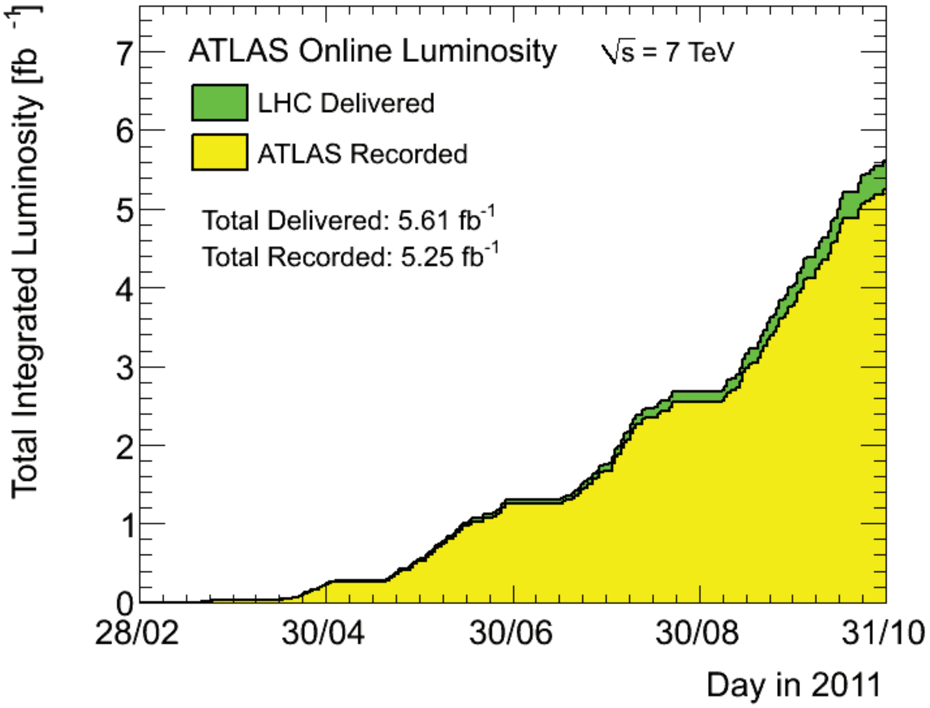

Figure 2.2. Cumulative luminosity versus day delivered to (green), and recorded by ATLAS (yellow) during stable beams and for pp collisions at 7 TeV center-of-mass energy in 2011. The delivered luminosity accounts for the luminosity delivered from the start of stable beams until the LHC requests ATLAS to turn the sensitive detector off to allow a beam dump or beam studies. Given is the luminosity as determined from counting rates measured by the luminosity detectors.

The peak stable luminosity achieved by the LHC in 2011 was 3.65×10^{33} cm^{-2}s^{-1}. It takes several hours to ramp up the energy of the proton beam, and the beam is stored for roughly a day (called a fill), until the beam becomes unstable, or the luminosity decays due to collisions and other escaping particles. Figure 2.2 shows the integrated luminosity as a function of time in 2011. The regions of this plot that are not increasing show experiment down-time. The plot also shows the increasing luminosity over the course of 2011, due to improvements, including increasing the number of bunches and number of protons per bunch.

2.2 The ATLAS Detector

The ATLAS detector[1] consists of a super-conducting solenoid surrounding a tracking spectrometer and vertexing detector (Inner Detector or ID), electromagnetic and hadronic calorimeters, and three large super-conducting toroids arranged with an eight-fold azimuthal symmetry providing the magnetic field for the large outer Muon Spectrometer. The Inner Detector is composed of pixel detectors and a silicon microstrip tracker (SCT), covering $|\eta| < 2.5$, and a straw-tube Transition Radiation Tracker (TRT) covering $|\eta| < 2.0$. The electromagnetic (EM) calorimeter provides electron identification and uses lead absorber plates and an active liquid argon presampler. The hadronic calorimeter is based on scintillating tiles in the barrel, and liquid argon in the endcaps, and together with the electromagnetic calorimeter provides a measurement of jet energy. The Muon Spectrometer provides muon identification and momentum measurement, particularly at high p_T, and is composed of 3 layers of precision chambers (Monitored Drift Tubes, supplemented by Cathode Strip Chambers in the forward region), and trigger chambers (Thin Gap Chambers in the endcap and Resistive Plate Chambers in the barrel).

A full description of the ATLAS and its material specifications can be found in Ref. [37]. Expected performance can be found in Ref. [38].

2.2.1 Inner Detector

Surrounding the beam-pipe, the Inner Detector is designed to provide pattern recognition, momentum measurements for charged tracks, and reconstruction of primary and secondary vertices. Due to the high interaction rate, the time resolution of

---

[1] The ATLAS detector uses a cylindrical coordinate system with the z axis along the beam pipe. The transverse momentum $p_{\mathrm{T}} = \sqrt{p_x^2 + p_y^2}$, and the pseudorapidity $\eta = -\ln(\tan\frac{\theta}{2})$ are used by particle physicists to describe kinematics due to their behavior under Lorentz boosts along the beamline (p_{T} is invariant and η is additive). θ is the azimuthal angle measured from the z axis.

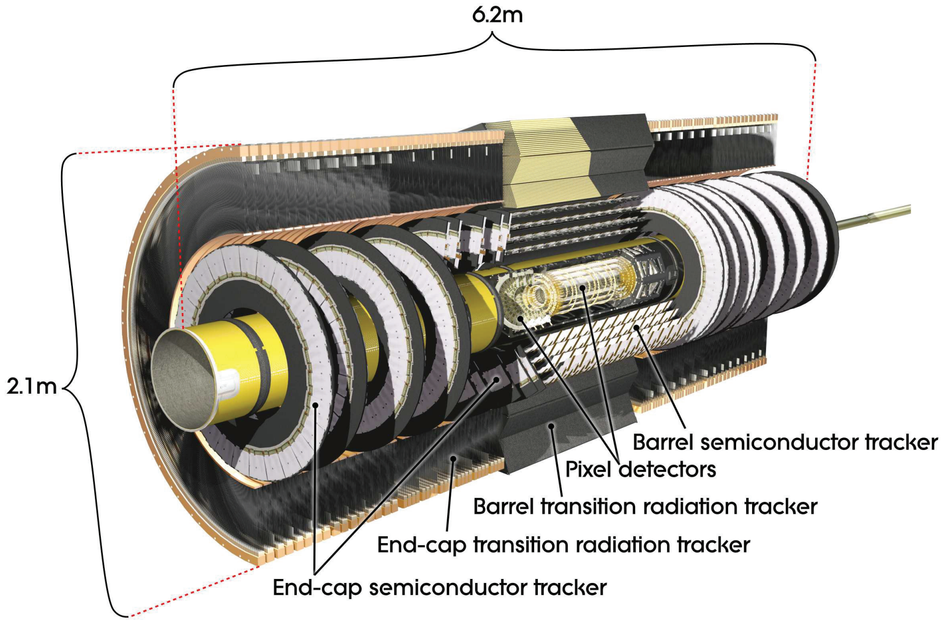

Figure 2.3. Cutout showing the ATLAS Inner Detector and its components.

the detector is required to be smaller than 25 ns to reduce the number of tracks not from the primary interaction.

Figure 2.3 shows a cutout of the ATLAS Inner Detector. The ID consists of three independent sub-detectors, as is emphasized in Figure 2.4. Closest to the beam-pipe, high resolution pattern recognition is provided by the discrete space point measurements of the Pixel detector and from stereo pairs made by silicon microstrips (SCT) just outside of the pixels. The TRT, located at larger radii, is a gaseous straw tube tracker with many layers of tubes. It provides an average of 36 measurements per track, continuous tracking over the range $|\eta| < 2.0$, and electron identification information complimentary to that provided by the ATLAS calorimeter system. The entire system is enclosed in a solenoidal magnet providing a nominal field strength of 2 Tesla. The design momentum resolution for most tracks is $\Delta p_{\mathrm{T}}/p_{\mathrm{T}} = 0.04\% \times p_{\mathrm{T}} \oplus 2\%$ (p_{T} in GeV) and an impact parameter resolution of 15 microns in the transverse plane.

The pixel detector is situated directly around the beam pipe. It has three layers of which the first pixel layer is positioned at a radius of 4cm. The total system has 80

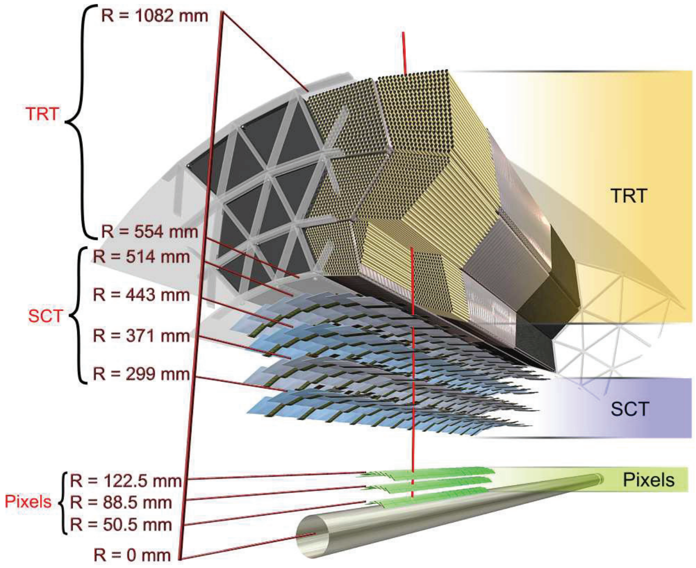

Figure 2.4. Diagram illustrating the 3 tracker technologies passed by a charged track of 10GeV pT in the barrel Inner Detector (η=0.3).

million pixels, each 50 μm in the $r-\phi$ plane and 400 μm along the z-axis. The three track measurements determine the impact parameter resolution and are vital for ID pattern recognition. The barrel SCT consists of four double layers of silicon strip detectors with a strip pitch of 80 μm providing four accurate measurements in the $r-\phi$ plane. The SCT end-caps both contain nine disks equipped with double layers of silicon strip detectors. The strips are pointing towards the beam axis providing a measurement in the $r-\phi$ plane. A small stereo angle between the strips in different layers makes it possible to measure the 3rd coordinate of the hit.

The TRT was designed to achieve the balance between cost and performance, providing a large number of space point measurements at low cost. This is achieved by using Polyimide drift straws with a diameter of 4 mm and a maximum length of 150 cm. In the barrel the straws are oriented parallel to the beam axis providing a measurement in the bending plane of the magnetic field. Following the design of the SCT, the straws in the end-cap are pointing towards the beam axis. The TRT can also detect transition radiation occurring when a relativistic particle crosses the boundary between two media with different electrical properties. The number of transition radiation hits is a measure for the velocity of a particle. This allows the separation of electrons and pions, and to a lesser extent the separation of kaons and pions.

2.2.2 Calorimeters

The ATLAS calorimeter system consists of an electromagnetic calorimeter designed to measure the energy of electrons and photons, located just outside of the solenoid, and just outside of this, a hadronic calorimeter designed to absorb the remaining energy from strongly interacting particles (excluding muons). In the far forward region, a radiation hard calorimeter is used, due to the large amount of particles produced near the beamline. This forward calorimeter has a coarser granularity. The accordion shape of the calorimeter system provides continuous azimuthal coverage. The total thickness of the electromagnetic calorimeter is more than 24 radiation lengths in the barrel and more than 26 radiation lengths in the end-cap. In addition to providing good containment for showers, this serves to limit other charged particles passing through to the muon system, which would otherwise be a source of fake muons. This excellent coverage also allows us to use conservation of momentum to reconstruct an addition variable, the Missing Transverse Momentum or $E_{\mathrm{T}}^{\mathrm{miss}}$, which is necessary to provide evidence for the presence of non-interacting particles. This variable is defined and described in Section 2.3.4.

The calorimeter system is shown in Figure 2.5. The EM calorimeter is divided into a barrel portion (from $|\eta| < 1.475$) and an endcap portion (from $1.375 < |\eta| < 3.2$). It is a lead-LAr detector with accordion-shaped kapton electrodes and lead absorber plates over its entire coverage. The calorimeter is segmented into 3 sections in depth over the region with Inner Detector coverage, where precision measurements can be made ($|\eta| < 2.5$), and 2 sections over the rest of the detector. The lateral sections are

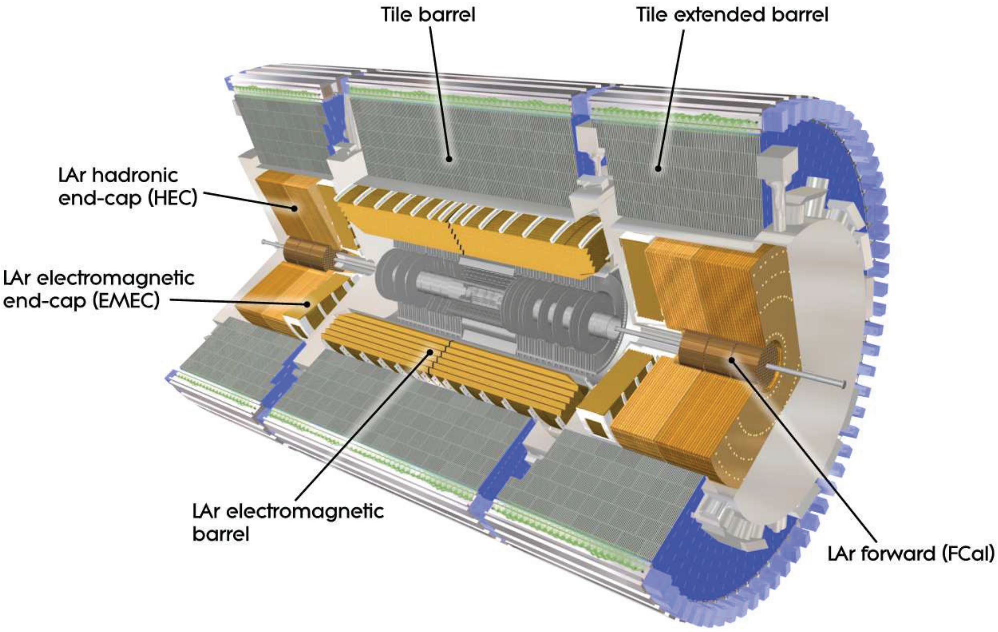

Figure 2.5. Diagram showing a cut out of the ATLAS Calorimeter system, including the electromagnetic, hadronic, and forward calorimeters.

projective in η and ϕ, and have finer granularity in the precision region. The typical energy resolution is $\Delta E/E = 11.5\%/\sqrt{E} \oplus 0.5\%$ (E in GeV), the resolution on the polar direction of a shower is $\delta\phi = 50 \text{ mrad}/\sqrt{E}$ (E in GeV).

The hadronic calorimeters use three different technologies for the barrel, endcap, and forward region. The barrel is covered by a tile calorimeter immediately outside of the EM calorimeter. It has two disconnected sections, barrel ($|\eta| < 1.0$), and extended barrel ($|\eta| < 1.7$). The tile calorimeter is a sampling calorimeter using steel as the absorber and scintillating tiles used for the active material. The calorimeter is segmented in three sections in depth and azimuthally into 64 modules, and is 0.97 meters thick, which corresponds to 9.7 interaction lengths at $\eta = 0$.

The hadronic endcap calorimeter is a LAr detector with copper plates as the absorber. It consists of two wheels per endcap, and overlaps with both the endcap and forward calorimeters ($1.5 < |\eta| < 3.2$). Each wheel has 32 wedge shaped modules, and two sections in depth.The average jet energy resolution (over the whole detector) is $\Delta E/E = 50\%/\sqrt{E} \oplus 3\%$ (E in GeV).

The forward calorimeter uses a high density design due to space and other constraints. It consists of a copper layer optimized for electromagnetic measurements, and two tungsten layers for measuring hadronic interactions. It covers the following range: $3.1 < |\eta| < 4.75$, and is approximately 10 radiation lengths.

2.2.3 Muon Spectrometer

The Muon Spectrometer (MS) is the outermost portion of the ATLAS detector, and also the largest. It is designed to measure charged particles exiting the calorimeter, the vast majority of which will be muons, due to their large mass, lack of hadronic interactions, and relative stability, which cause them to typically lose only a small amount of ionization energy in the calorimeter systems. The MS is capable of standalone momentum measurement of charged tracks over the range $|\eta| < 2.7$, and is capable of triggering on these tracks for $|\eta| < 2.4$. A specific design goal of ATLAS is to be able to measure the transverse momentum of 1 TeV muon tracks with a resolution of approximately 10%. Given the average magnetic field strength, this corresponds to a sagitta (defined as the depth of an arc) of approximately 500 μm, therefore requiring a sagittal resolution of ≤ 50 μm. Muon momentum can be measured down to about 3 GeV by the spectrometer independently, this limitation due to energy loss in the calorimeter.

The Muon Spectrometer is shown in Figure 2.6.The barrel tracking chambers are located on and between the eight coils of the toroidal magnet system. The muon system as a whole has an eight fold ϕ symmetry, matching that of the toroid. Each octant is subdivided azimuthally into 2 sections, a small and large sector, with some overlap region in ϕ, minimizing gaps in detector coverage. The barrel has 3 cylindrical layers of chambers at radii of approximately 5 m, 7.5 m, 10 m. There is a gap in

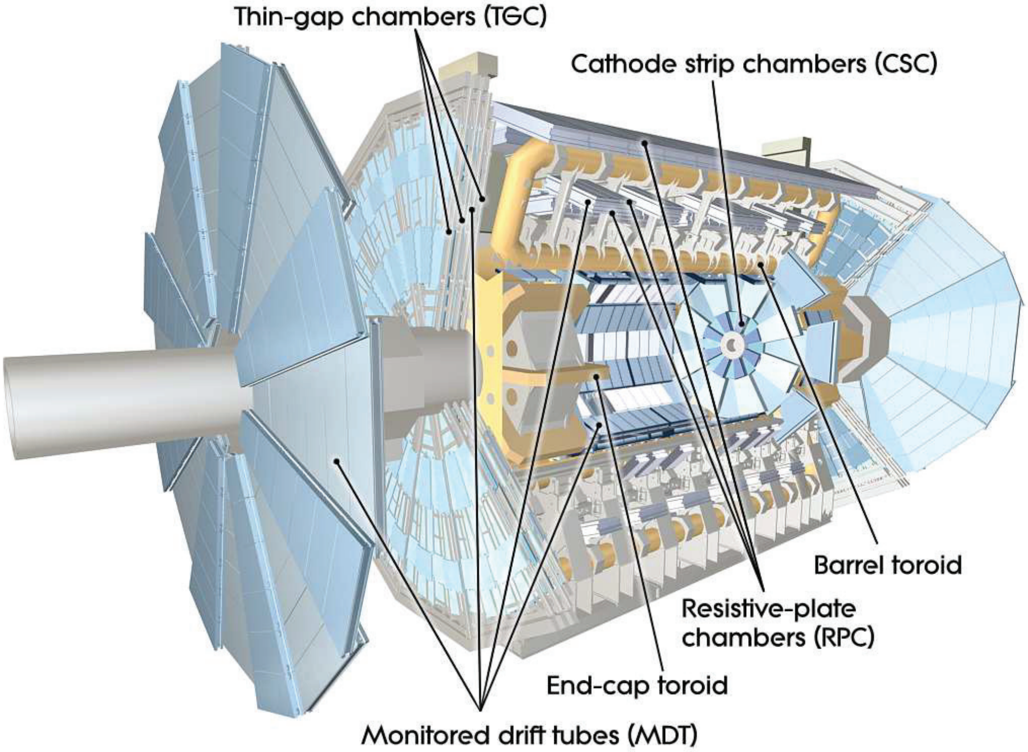

Figure 2.6. Diagrammatic cut out of the ATLAS Muon Spectrometer.

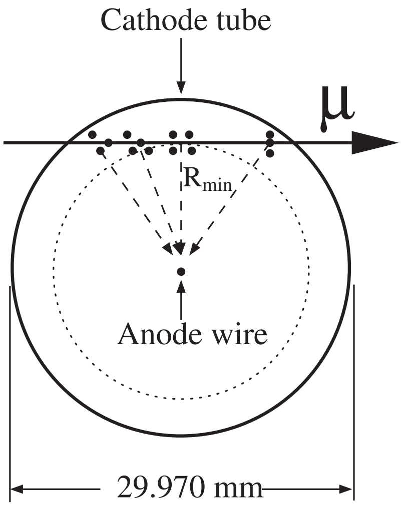

Figure 2.7. Schematic of a muon drift tube.

acceptance at $|\eta| \approx 0$, left open for services to the solenoid, calorimeter and Inner Detector. In the endcap, the chambers are placed on large wheels orthogonal to the z-axis, at roughly 7.4 m, 10.8 m, 14 m, and 21.5 m.

The precision momentum measurement is primarily performed by Monitored Drift Tube (MDT) chambers, consisting of pressurized drift tubes with a radius of about 3 cm, operating with Ar/CO_2 gas (93/7) at a pressure of 3 bar (Fig. 2.7). Ionization from passing muons is collected at a central tungsten-rhenium wire, held at a potential of 3080 V. Each chamber consists of 3 to 8 layers of drift tubes. The MDTs achieve an average resolution of 80 μm per tube, or roughly 35 μm per chamber. The MDT chambers have the advantage of mechanical precision and robustness, because a tube failure does not affect the operation of the other tubes.

The measured pulse spectrum of of the collected ionization is measured each time a tube is read out, as shown in Figure 2.8. The key characteristic of this distribution is the time of the leading edge, often called the drift time. The figure also shows a typical relationship between the drift time and distance of closest approach of the anode of the MDT. This relationship is not found during the reconstruction of an

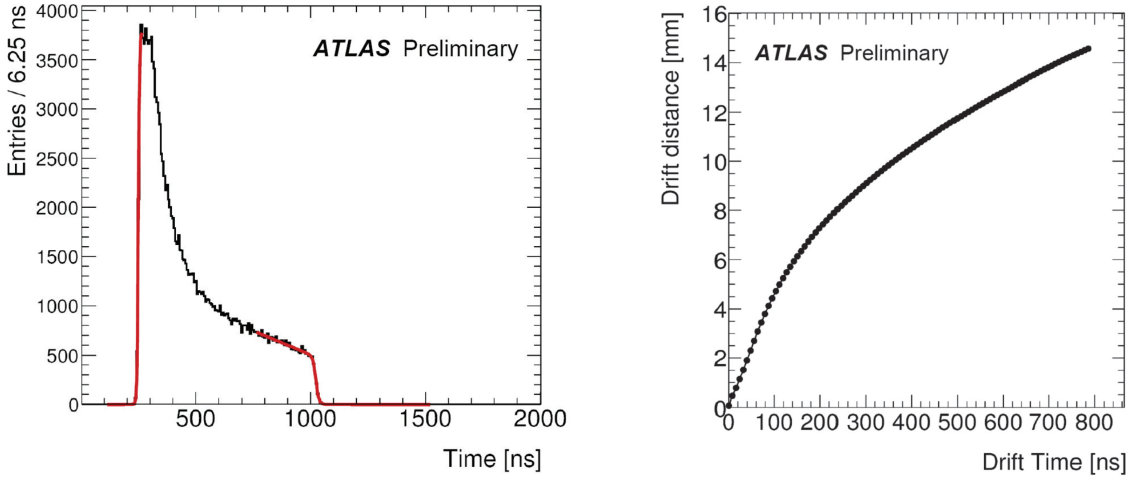

Figure 2.8. A typical MDT measured pulse spectrum (left) and space-time (r-t) relationship for MDT chambers (right).

event, but rather for each chamber using an iterative calibration procedure that uses straight muon tracks as input.

In the forward region $2.0 < |\eta| < 2.7$ the most inner precision tracking layer is made up of Cathode-Strip Chambers (CSC). These have higher rate capability and time resolution than the MDTs, and are therefore well suited to the high activity region near the beamline. The CSCs are multi-wire proportional chambers capable of measuring both coordinates from the induced charge distribution. CSC resolution is 40 μm in the bending plane, and about 5mm non-bending plane.

The design goals of ATLAS require the locations of the MDT and CSC chambers along a muon track to be known better than 30 μm. In order to achieve this, an optical alignment system is used to monitor the positions and deformations of the precision chambers. This is complemented by track-based alignment algorithms that are used to provide independent confirmation of proper alignment.

The capability to trigger on muon tracks is provided by a system of fast trigger chambers capable of relaying track information within 20 ns of a particles passage. Resistive Plate Chambers (RPC) are used in the barrel region ($|\eta| < 1.05$), and Thin

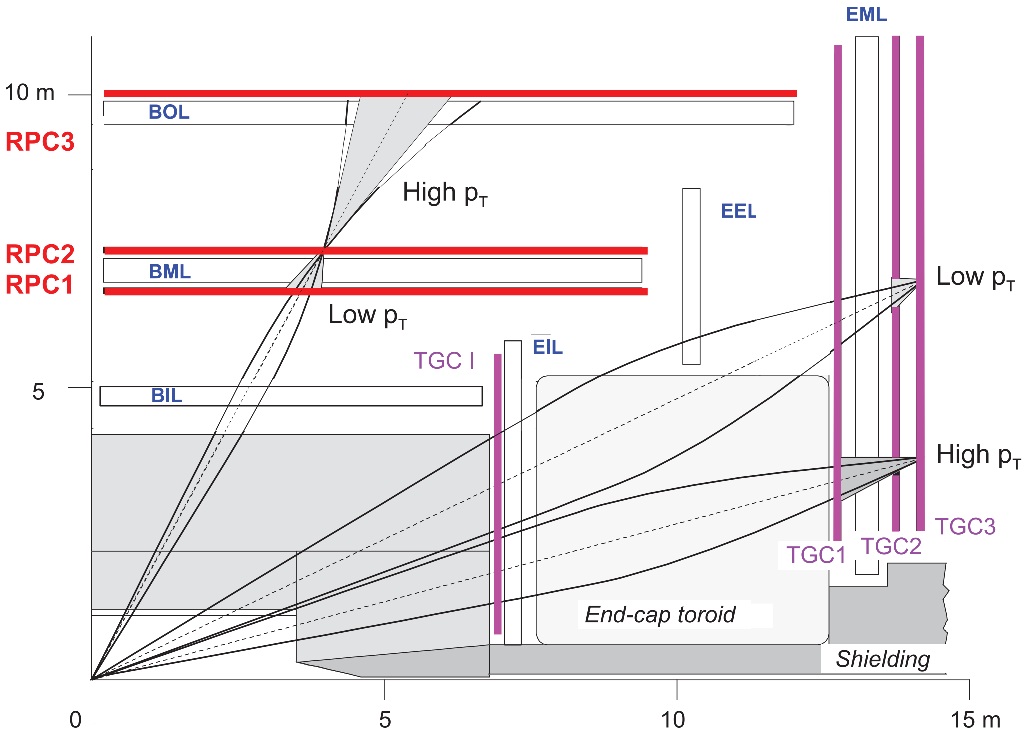

Figure 2.9. Schematic drawing of the muon trigger system.

Gap Chambers (TGC) are used in the endcap ($1.05 < |\eta| < 2.4$). The TGCs (RPCs) have an intrinsic time resolution of 4 ns (1.5 ns). Design of these chambers require the signal propagation and electronics times to also be small in order for reliable beam-crossing identification with greater than 99% probability. Both chamber types provide this, delivering signals with a spread of 15-25 ns. In addition to triggering, each trigger chamber measures both coordinates of the track, one in the bending (η) plane, and the other in the non-bending (ϕ) plane. The MDTs only measure the coordinate of the track in the bending plane, and therefore the trigger chambers coordinate is used as the second coordinate of the MDT measurement.

The RPC trigger chambers exist in three layers, as shown in Figure 2.9: two sandwiching the middle layer of MDT chambers, and one placed on the outer MDT chambers. The large lever arm between the inner and outer RPCs allows triggering on tracks with small curvature (high p_T trigger: 9-35 GeV). The two inner chambers provide for the low p_T trigger: 6-9 GeV. The three chambers also allow redundancy, which allows for the rejection of fake tracks from noise hits. The RPC is a gaseous parallel electrode-plate detector. The two resistive plates spaced at a distance of 2mm, and the field of 4.9 kV/mm allows avalanches to form towards the anode, along the muon tracks. The gas used is a mixture of $C_2H_2F_4$/Iso-C_4H_{10}/SF_6 (94.7/5/0.3).

The endcap has different trigger requirements than the barrel. Physics analysis requires a trigger on p_T, but the Muon Spectrometer measures the momentum. Correspondingly, p is about 5.8 times larger than p_T at $|\eta| < 2.4$, but the integrated field strength is only about twice the value at $|\eta| = 0$. This requires an increased and η dependent granularity in the endcap. Other challenges of the endcap trigger system include higher rate and a complex field structure in the transition region. For all these reasons a different technology was selected in the endcap (TGCs). The middle layer of MDTs is accompanied by 7 layers of TGCs, while the inner layer only has two TGC layers. Thin Gap Chambers operate on the same principle as multiple-wire proportional chambers and have high rate capability and adjustable spatial resolution (based on the readout channel granularity). The TGCs use a highly quenching gas mixture of CO_2 and n-$C5H_{12}$ (n-pentane).

The air-core magnet concept of the Muon Spectrometer minimizes the amount of material traversed by muon tracks after their exit from the calorimeters. However, the muons must also pass other materials, such as support structures, vacuum vessels, the toroid coils, and the muon chambers themselves. Figure 2.10 shows the material distribution that the muon tracks cross as a function of η and ϕ. As shown in the figure, there is a large increase in the radiative thickness above $|\eta| \approx 1.4$. This is due to the heavy mechanical structure of the endcap toroid, and the fact that the tracking chambers and toroid have separate support structures in the endcap.

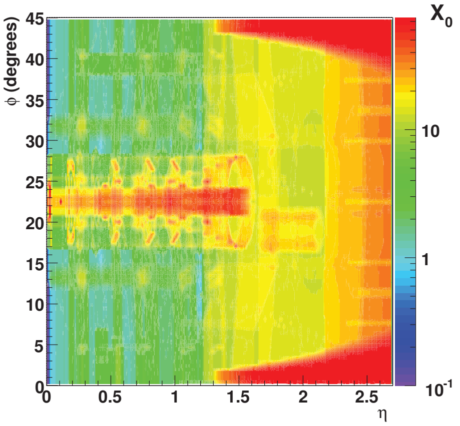

Figure 2.10. Number of radiation lengths of material passed by a straight muon track after exiting the calorimeter system.

2.2.4 Trigger, Data Acquisition, and Data Quality

The bunch crossing rate in 2011 was 20 MHz, and each event recorded produces approximately 1.5 MB of data. Given this preponderance of data, and the fact that the processes of interest occur at a much lower rate, it is unrealistic and unnecessary to write every ATLAS event to disk. ATLAS uses a three level trigger and data acquisition system to select events of interest and reduce the amount of data written to disk.

The first level (L1) is a purely hardware based trigger system. This level of event selection must be very fast in order to resolve events in time with the current bunch crossing. Each bunch crossing has a design separation of 25 ns, and a trigger decision must be made within 2.5 μs in order to achieve the necessary data reduction. The L1 trigger uses a subset of detector elements to look for simple signatures such as tracks with small curvature indicating a high momentum particle. The Central Trigger Processor (CPT) organizes this information and defines one or more Regions of Interest (ROI). This selection reduces the data stream from a rate of 20 MHz to 70 kHZ. This data is then passed to temporary data buffers and processed by the next two trigger layers, level two (L2), and the event filter (EF). These two trigger selections are software based and collectively make up the High Level Trigger (HLT).

The L2 trigger is seeded by the regions of interests defined by the L1 trigger, and uses all detector information within this region. Simplified reconstruction and selection is performed on these objects, and the rate is further reduced from 100 kHz to 3 kHz. Finally the EF performs full reconstruction on the remaining events, using the same algorithms as the offline reconstruction, and the rate is further reduced to roughly 200-400 Hz.

A large number of trigger selections (triggers) are defined to select different physics signatures (muons, displaced vertices, $E_{\mathrm{T}}^{\mathrm{miss}}$). Many of these processes are useful, but occur at a rate that would overwhelm the data acquisition system. In this case, the trigger corresponding to that process is prescaled, meaning that a certain proportion of the events passing the trigger are not passed on to the next stage of data acquisition.

Selected events are written to tape where they are stored by run number, a run being defined by a single fill and lasting approximately one day, and by Lumi Block (LB) which are divisions based on time varying from run to run, roughly 2 minutes long for current running. This data is separated by physics event streams based on different object signatures. Conditions and data quality information are also stored for each Lumi Block in a separate database.

For physics studies it is critical that the detector conditions be optimal, stable, and well understood. Data quality flags are defined based on whether the detector was capable of reading out (electronics, power-supplies, gas systems, etc. were functional), and based on the results of an online data monitoring framework which compares a number of data quality histograms to expected distributions. These quality criteria are defined per Lumi Block, and are used to define “Good Run Lists” that define a baseline of acceptable data for a particular analysis or working group. Data quality requirements for this thesis are listed below:

- General: The ATLAS data has been evaluated and approved by the Data Quality group, the currents in the solenoid and toroid magnets are stable (and nonzero), and the luminosity and forward detectors are operational and give reliable luminosity measurements. A reliable beam spot measurement is also required.

- Muon Spectrometer: Each section of the MDT, RPC and TGC chambers must have more than 90% of the system with High Voltage on and be collecting data. There also must be at least 3 of 4 layers taking good quality data in all CSC chambers.

- Inner Detector: The Pixel, SCT and TRT detectors are operating correctly, there are no known problems with the data, software-level tracking is OK and there are no synchronization or timing problems in the ID detector.

- Calorimeters: The EM and hadronic calorimeters are functional and reading out, and the data and calibration are in agreement with the current understanding of the detector. The hadronic calorimeter must be timed in to within 2 bunch crossings, and no more 3 consecutive modules may be out of data taking.

- Trigger: Muon triggers in both the barrel and the endcap have been on and running with reasonable efficiency, and there were no timing, consistency, synchronization or data problems.

- Muon Reconstruction: The software algorithms Staco and Muid were running without problems.

- Jet/$E_{\mathrm{T}}^{\mathrm{miss}}$ Reconstruction: Jets and $E_{\mathrm{T}}^{\mathrm{miss}}$ variables must have smooth eta/phi distributions (no unexpected peaks or depleted regions), no excess of events with high p_{T} jets or excessive $E_{\mathrm{T}}^{\mathrm{miss}}$, and reasonable symmetry in phi and in positive/negative eta regions.

2.3 Object Definitions and Reconstruction

This section describes the reconstruction of muons, electrons, jets, and $E_{\mathrm{T}}^{\mathrm{miss}}$ in collision events and how these objects are defined in this analysis. The Athena software framework is used by ATLAS to simulate, digitize, and reconstruct collision events, as well as for final physics analysis tools. This framework is coded in C++ and configured by python scripts. Release 17 of the framework was used for the majority of this analysis.

2.3.1 Electron Reconstruction

Electron candidates are reconstructed by associating an EM calorimeter energy deposit with a track in the Inner Detector. Energy deposits are first formed into clusters using the "Sliding Window Clustering" method. First, the EM calorimeter is divided into a grid of "towers" which are small rectangular divisions in η and ϕ. For each tower, the energy of the cells is summed across all longitudinal layers. Then a window of set size in η and ϕ is shifted across this grid of towers. When the summed energy in these towers is above some threshold, a seed is formed. Cluster seeds then undergo overlap removal and their center is calculated. Then the final cluster is defined by a set size centered around the seed center, in our case clusters are 3 x 7 towers in $\eta \times \phi$.

These clusters are then used to seed the track matching procedure. For each cluster, tracks with track parameters at the interaction point (IP) nearby the cluster position (0.05 in η, 0.1 in ϕ), are loosely associated with the cluster. These tracks are then extrapolated to the 2nd calorimeter sampling depth and $\Delta R = \sqrt{(\Delta\eta)^2 + (\Delta\phi)^2}$ is calculated between the cluster and the track. The track with the smallest ΔR is matched to the cluster.

Electron candidates are distinguished from hadronic energy deposits through a number of selection criteria. Electromagnetic showers, as compared to hadronic showers, are expected to have different distributions in the calorimeter system. Electron candidates are required to satisfy lateral shower containment, shape and width criteria, and minimal leakage into the hadronic calorimeter in order to be classified as "medium". In addition, medium electrons must pass the following hit criteria:

- at least nine precision hits (Pixel+SCT),
- at least two hits in the pixel layers, one of the hits being in the b-layer,
- a transverse impact parameter $|d_0| < 0.1$ cm.

The impact parameter d_0 is the transverse distance of the ID track from the "primary vertex" of the hard scatter. Primary vertices are reconstructed by extrapolating all tracks to the interaction point, and fitting them to a single vertex. If multiple vertices are reconstructed, the one with the largest scalar sum p_{T} is associated with the hard scattering process. The lateral impact parameter z_0 is determined in the same manner.

Consistency between track p_T and cluster energy, as well as tighter hit requirements are additionally required to categorize an electron as "tight". Electrons of many interesting physical processes are also expected to be isolated from other hadronic activity, however, this criterion is highly dependent on the physics channel being investigated. In this analysis isolation was not required at the electron definition level.

The electron energy is defined by the calorimeter cluster energy, which is more precise at higher energies. The electron direction is given by the track parameters, as the Inner Detector provides much better spatial resolution. In the case of a track with fewer than 4 Silicon hits (pixel and/or SCT) the cluster η and ϕ are used for the electron, as the TRT detector does not provide adequate angular information. Cluster η is also used to bin all corrections involving the calorimeter: identification efficiency, scale corrections, and rejection of regions with dead sensors.

2.3.2 Muon Reconstruction

Two families of muon reconstruction algorithms exist for the ATLAS collaboration, and there is currently a central effort to merge the best features of the two algorithms. This thesis uses exclusively muons reconstructed by the Staco algorithm, and the other algorithm Muid will not be discussed in depth.

The reconstruction of a muon begins by building the precision hits in the Muon Spectrometer into segments, which are muon paths generally confined to a single muon chamber. These segments define a position and direction in the precision plane for the muon as it passes that chamber. These segments (typically three segments/chambers traversed by the muon) are built into a track and combined with trigger chamber information, providing information on the second position coordinate. This track is extrapolated back to the interaction point, taking energy loss in the calorimeter into account. All track parameters (q/p_{T}, η, ϕ, d_0 and z_0) are then expressed with respect to the primary reconstructed vertex. This track is referred to as a standalone muon, for which no ID information is used. Standalone muons have excellent reconstruction efficiency and momentum resolution, but suffer from high fake rates from cosmics, decay in flight of pions, and other processes.

Combined muons are formed by combining the Muon Spectrometer track with an Inner Detector track. The muon track is extrapolated to the interaction point, and matched by ΔR to an Inner Detector track. The track parameters of the combined muon are calculated using a statistical combination of the track parameters and error matrices of the ID and MS track. In the case of multiple ID tracks matched to a MS track, the pair with the lowest match-χ^2 is chosen, given by:

$$\chi^2 = (P_1 - P_2)^T (C_1^{-1} + C_2^{-1})^{-1} (P_1 - P_2), \tag{2.1}$$

where P_1 and P_2 are the track parameter vectors, and C_1 and C_2 are the covariance matrices of the track parameters for the ID and MS, respectively. A minimum match-

χ^2 requirement is also placed on the final combined muon. Combined muons have much lower fake rates than standalone muons. The following hit requirements are also placed on combined muons:

- pixel hits + dead sensors traversed > 1
- SCT hits + dead sensors traversed > 5
- Missing Silicon Hits traversed by track < 3
- A successful TRT extension when within the TRT acceptance.

For the purposes of this analysis, a combined muon as described above is characterized as having "medium" quality. In order for a muon to be considered "tight" quality, the following further requirements are made on the particles impact parameters and isolation from other track activity:

- $|d_0| / \sigma_{d_0} < 3$
- $|z_0| < 0.1\,\mathrm{mm}$
- $\Sigma p_{\mathrm{T-cone-0.2}} / p_{\mathrm{T}} < 0.1$

Here d_0 and z_0 are the impact parameters of the ID track with respect to the primary vertex, and σ_{d_0} is the uncertainty of the d_0 measurement, due to the uncertainty of both the track and the vertex. The last selection in the list is a track isolation cut, as muons from electroweak boson decay will in most cases be isolated from hadronic activity. Specifically $\Sigma p_{\mathrm{T-cone-0.2}}$ is the summed transverse momentum of all ID tracks within a cone of 0.2 in ΔR.

2.3.3 Jet Reconstruction

The goal of jet reconstruction is to turn the signals from the 180,000 calorimeter cells read out by the ATLAS detector into "jets", that is, aggregations of secondary decay particles roughly corresponding to the existence of original partons (gluons/quarks). Calorimeter cells are first grouped by one of two methods. The tower method uses a projective fixed 2-dimensional grid in η and ϕ with a grid size of 0.1. Alternatively, the topological clustering method uses the relationship between neighboring cells and the significance of their energy content to form clusters that closely model the actual energy deposition of incident particles. Both of these approaches can be used as inputs for jet reconstruction. Topological clustering is used for all jet reconstruction in this thesis.

There are a large number of algorithms available for grouping energy deposits into jets. The following features are desirable in a jet algorithm:

- The algorithm should work effectively at different levels, for example, using decay products from a simulation as well as using energy deposits directly from the detector.
- The number of final state jets and their energies should not be heavily dependent upon the distribution of soft or collinear particles. Instability of this kind is related to divergences in higher order perturbative calculations. This is the well known Infrared Collinear Safe problem (IRC). Examples of algorithms that fail this requirement include both "fixed cone" and "iterative cone" algorithms.
- Jets should have a somewhat regular shape that is not strongly dependent upon the distribution of soft particles. Cone algorithms pass this requirement, while many IRC safe algorithms, such as the k_T algorithm [39], suffer from a more flexible shape.

The anti-k_T algorithm has all of these features, and is the default jet reconstruction algorithm for ATLAS [40]. This algorithm is a sequential recombination algorithm, in which particles are recursively combined with the closest particle or “pseudo-jet” based on a measure of distance defined by the following:

$$\begin{aligned} d_{ij} &= \min(k_{ti}^{2p}, k_{tj}^{2p}) \frac{\Delta_{ij}^2}{R^2} \\ d_{iB} &= k_{ip}^{2p}, \end{aligned}$$

where $\Delta_{ij}^2 = (y_i y_j)^2 + (\phi_i \phi_j)^2$ and k_{ti}, y_i and ϕ_i are respectively the transverse momentum, rapidity and azimuth of particle i. The variable R is a free parameter which corresponds roughly to the preferred radius of the resulting jets, and d_{iB} is the distance to the beam. If the beam is the “closest” object to a pseudo-jet, it is removed from the list of objects for comparison and defined as a jet. The type of recombination algorithm is defined by p, for $p = 1$ we have the inclusive k_T algorithm, for $p = 0$ we recover the inclusive Cambridge/Aachen algorithm [41], and for $p = -1$ we recover our preferred algorithm, anti-k_T. The major characteristic of this algorithm is that soft particles will prefer to cluster with hard particles long before they cluster with other soft particles, leading to the “soft resilient” boundary we find desirable. Further description of how the beneficial characteristics of the algorithm follow from its definition is beyond the scope of this dissertation.

The jets in this thesis use an R value of 0.4.

2.3.4 $E_{\mathrm{T}}^{\mathrm{miss}}$ Reconstruction

Missing Transverse Momentum ($E_{\mathrm{T}}^{\mathrm{miss}}$) is calculated as the sum of momenta of all reconstructed objects, including muons, with an additional term for energy deposits unassociated with reconstructed objects. The term has the misleading variable $E_{\mathrm{T}}^{\mathrm{miss}}$for historical reasons, as for older detectors where the reconstruction of jet momenta was difficult, and the jet energies were instead used. This quantity, by conservation of energy and momentum is expected to be zero if we assume all decay products of the initial hard scatter are reconstructed. Therefore large $E_{\mathrm{T}}^{\mathrm{miss}}$ indicates the presence of particles that do not interact with the detector elements, such as neutrinos or new exotic particles.

The calibration of cell energy weights can be calculated a number of ways:

- H1-style Calibration: In this method, weights are a function of detector region and energy density, and are optimized using jet events.
- Hadronic Calibration: The weights from the topocluster calibration are used, and are optimized using single pions. (Section 2.3.3)
- Refined Calibration: Cells are given weights as a function of what reconstructed objects they are matched to (electrons, photons, jets, etc).

In this study, Refined Calibration is used for $E_{\mathrm{T}}^{\mathrm{miss}}$, unless otherwise specified. Noise suppression is applied to the cells by requiring $|E| > 2\sigma_{\mathrm{noise}}$ where σ_{noise} is the RMS of the noise produced by a particular cell.

The muon portion of the calculation of $E_{\mathrm{T}}^{\mathrm{miss}}$ is calculated primarily from Combined Muons. Calorimeter cells traversed by these muons are removed from the calculation to avoid double counting. Tagged muons are also included in the range $1.0 < |\eta| < 1.3$ in order to recover efficiency in the transition region between the barrel and the endcap. Standalone muons are used in the region $2.5 < |\eta| < 2.7$ due to the fact that the Inner Detector does not cover this region of the detector.

CHAPTER 3

W/Z +JETS CROSS SECTION RATIO MEASUREMENT

As discussed in the Introduction, this thesis presents a measurement of the cross section times branching fraction ratio between W and Z bosons:

$$R_{\text{jet}} = \frac{\sigma_W BR(W \to \ell\nu)}{\sigma_Z BR(Z \to \ell\ell)}. \tag{3.1}$$

This quantity is measured as a function of the following distributions: the number of selected jets, the p_T and rapidity of the 1st, 2nd, 3rd and 4th leading jets, the scalar sum p_T of all selected jets $S_T = \sum p_{Tjets}$, and the scalar sum of all high-p_T selected objects in the event, including leptons, $E_{\text{T}}^{\text{miss}}$, and jets, referred to as H_T. It is also measured as a function of the following dijet variables: invariant mass, ΔR_{jj} and $\Delta\phi_{jj}$

The measurement of R_{jet} is done using the 2011 ATLAS pp collision dataset, with an integrated luminosity of 4.64 fb^{-1}. This data passes the quality selection described in Section 2.2.4. The measurement is made in two channels: with the boson decaying to muon(s), and with the boson decaying to electron(s). The thesis presents the results only for the muon channel, though future publications will include results for both channels. The relevant equation for determining cross sections is the following:

$$\sigma = \frac{N(1 - f_b)}{A\varepsilon \int \mathcal{L}dt}, \tag{3.2}$$

where N is the number of events passing event selection, f_b is the background fraction, A is the geometrical and kinematic acceptance of the detector to a W or Z event,

ε is the overall selection efficiency, which includes both reconstruction and trigger efficiencies, and efficiencies of selection requirements made to reduce backgrounds. Finally $\int \mathcal{L}dt$ is the integrated luminosity. This equation can be used directly for the calculation of inclusive cross sections. When measuring a differential distribution such as R_{jet}, applying this formula bin-by-bin can produce biased results if the migration matrix from detector level to hadron level is significantly non-diagonal. This problem and preferred correction procedures are discussed in Section 3.12.

The description of the measurement begins with the details of simulated samples used in the analysis in Section 3.1, and the treatment of events overlapping the primary collision is covered in Section 3.2. Event selection for W/Z events is presented in Sections 3.3 and 3.4. Electroweak (W,Z,diboson) and top backgrounds are estimated directly from MC samples, while hadronic backgrounds are estimated from control samples in the data, due to the large uncertainties on their cross section, as described in Section 3.6. Trigger and Reconstruction efficiencies for the leptons used to measure the W/Z bosons are measured using tag-and-probe methods, described in Sections 3.7 and 3.8. Event level selection efficiencies for W/Z events are determined from MC, and are corrected using scale factor of measured over simulated efficiency for both the trigger and the reconstruction.

Scale and resolution corrections to momenta are determined from data for both jets and leptons. This is described in detail for the muon channel in Sections 3.9 and for jets in 3.10. Changes in the lepton/jet momenta affect the calculation of $E_{\mathrm{T}}^{\mathrm{miss}}$, and as such, these corrections are propagated to the $E_{\mathrm{T}}^{\mathrm{miss}}$ calculation, as are the systematic uncertainties on these corrections.

Section 3.11 describes the uncertainties on the theoretical prediction for R_{jet} at truth level. Section 3.12 describes the methods we use to determine hadron level cross-sections from the measured distributions. Section 3.13 summarizes the systematic and statistical uncertainties involved in the measurement, and Section 3.14 presents the final comparison of the unfolded measurements with current theoretical calculations. Cross checks and control distributions are included in Section 3.5.

3.1 Monte Carlo Samples

Simulated event samples were used to correct signal yields for detector effects, for some of the background estimates, and for comparison of the results to theoretical expectations. This section gives the technical specifications of the MC generators used in this thesis, for a more conceptual description, see Section 1.9.

Signal events ($Z \rightarrow \mu\mu$, $Z \rightarrow ee$, $W \rightarrow \mu\nu$, $W \rightarrow e\nu$) are generated using ALPGEN v2.13 [23] interfaced with HERWIG v6.520 [29] for parton shower and fragmentation into particles and to JIMMY v4.31 [29] to model underlying event contributions, using the AUET2-CTEQ6L1 tune [42]. For the ALPGEN samples, CTEQ61L [43] parton distribution functions (PDFs) are employed. Signal samples are also generated with SHERPA v1.4.0 [25], using CTEQ10 [44] PDFs. The program PHOTOS [28] is used to simulate final state QED radiation in ALPGEN and PYTHIA samples. SHERPA uses a self designed parton shower algorithm [25]. Both ALPGEN and SHERPA signal samples are generated up to 5 partons.

Background samples from other W/Z final states are generated similarly to the signal samples, using ALPGEN with HERWIG and JIMMY with CTEQ61L PDFs, normalized to NNLO and NLO pQCD predictions, respectively. Top-pair samples are produced in the same scheme. Single-top events are generated with ACERMC [45], interfaced with PYTHIA. Diboson processes (WW, WZ and ZZ) are simulated with HERWIG using the AUET2-LO* tune [42].

The generated samples are passed through a full simulation of the ATLAS detector and trigger, based on GEANT4 [22]. The simulated events are then reconstructed and analyzed with the same analysis chain as for the data, and the same trigger and event selection criteria. Uncertainties on the cross sections are of the order of 5%, except for $t\bar{t}$ cross sections, for which the uncertainty is about 10%.

3.2 Pileup

Due to the high luminosity at which the LHC is running, collision events overlap in time. When an event is triggered by the production of some high p_{T} object, typically an addition 3-18 collisions are also occurring, each with its own vertex. Nearly all of the additional collisions are not hard scatters, but very low energy collisions. These collisions have been studied individually at low luminosity, using a trigger with very minimal energy requirement, so as not to bias the topology of the collision. These typical, low energy collisions are as such often termed minimum-bias events. The additional minimum-bias events overlapping a high p_{T} collision of interest are often termed pileup.

The luminosity was still evolving at the time the MC samples were produced, so they are reweighted to produce agreement between the number of interactions in the MC samples and in the data. The amount of pileup increases with the luminosity, and as such the pileup increased as the luminosity increased throughout 2011. In addition, as described in the next section, jets originating from a pileup vertex are also rejected from the analysis.

3.3 Object Selection

Selected leptons in this thesis will refer specifically to muons and electrons. Leptons are selected if they have $p_{\mathrm{T}} > 25$ (20) GeV for the W (Z) channel, and are within $|\eta|$ of 2.4. Electrons are also rejected if they are within a crack in calorimeter coverage $1.37 < |\eta| < 1.53$. Jets are selected if they have $p_{\mathrm{T}} > 30$ GeV and $|y| < 4.4$. For unfolding of p_T distributions, jets with p_{T} down to 20 GeV are used in order to avoid edge effects, even though final results are only reported for $p_T > 30$ GeV. Object definitions, including lepton quality, are discussed in detail in Section 2.3. Jets are rejected if they are within $\Delta R < 0.5$ of a selected lepton.

The above selections are also applied at truth level predictions for jets (after hadronization) and leptons. The truth level leptons are calculated as “dressed” leptons, that is, they are calculated after initial and final state radiation, but with all photons from the primary collision within a cone of $\Delta R < 0.1$ added to the lepton momentum 4-vector.

Jets at reconstruction level are also subject to a variety of quality criteria, in order to remove jets that are likely to be from non-collision backgrounds, or from noise in calorimeter electronics. These criteria are based on quality information from individual clusters, shower shape information (for example that the shower should not be concentrated in a particular layer), and timing information. Jets within $|\eta| < 2.4$ are also required to have $JVF < 0.75$, where JVF is defined as the fraction of energy from tracks originating at the primary vertex. Jets failing this selection are real jets of good quality, but are usually from pileup interactions overlapping the primary collision.

3.4 W/Z Event Selection

Selection of W and Z events requires a primary vertex consistent with the beamspot and with at least 3 ID tracks. For runs 180614-185352, a detector element in the EM calorimeter failed. The affected angular area was roughly $-0.1 < \eta < 1.5$ and $-0.9 < \phi < -0.5$. Events with a jet with $p_{\mathrm{T}} > 20$ GeV within the affected area are rejected. Events with a jet failing quality criteria within $p_{\mathrm{T}} > 20$ GeV and $|\eta| < 4.5$ are also rejected. Single lepton triggers are required to be passed, and the trigger must be matched to a selected lepton, as described in detail in Section 3.7.

Selection of W events requires exactly one “tight” lepton and no “medium” leptons, as described in Sections 2.3.1 and 2.3.2. In addition the following requirements are imposed $E_{\mathrm{T}}^{\mathrm{miss}} > 25$ GeV and $M_{\mathrm{T}} > 40$ GeV where M_{T} is the transverse mass: $M_{\mathrm{T}} = \sqrt{2p_T^{\mu} E_{\mathrm{T}}^{\mathrm{miss}}(1 - \cos\Delta\phi))}$, where $\Delta\phi$ is the angle between the $E_{\mathrm{T}}^{\mathrm{miss}}$ vector and the muon p_{T} vector. At hadron level, these same requirements are made, but with the $E_{\mathrm{T}}^{\mathrm{miss}}$ replaced by the p_{T} of the neutrino.

Selection of Z events requires two medium electrons in the electron channel, or one tight muon and one medium muon in the muon channel. Events with additional medium leptons are rejected. The two selected leptons are required to have opposite sign charge, and an invariant mass in the range: 66 GeV $< |m_{\mu+\mu-}| <$ 116 GeV. The same requirements are made at hadron level.

The full details of $W \rightarrow \mu\nu$ and $Z \rightarrow \mu\mu$ event selection are shown in Table 3.1.

3.5 Control Plots

Because a variety of MC corrections are performed on the jets, $E_{\mathrm{T}}^{\mathrm{miss}}$, and leptons in these studies, a number of cross checks are performed to establish the consistency of the measurement. The control plots in this section compare the detector level measurement to the value predicted by the Alpgen simulation. The consistency of these plots underpins our confidence in the measurement.

Figure 3.1 shows the detector level distributions for $E_{\mathrm{T}}^{\mathrm{miss}}$ and M_{T} in the W channel, and for $m_{\mu+\mu-}$ in the Z channel. Figure 3.2 shows the exclusive jet multiplicity at detector level for each channel, and the experimental systematic uncertainties on this measurement. Figure 3.3 shows the leading jet p_{T} at detector level for each channel, and the experimental systematic uncertainties on this measurement.

3.6 Backgrounds

Expected and measured muon channel events for signal and background are shown in Tables 3.2 and 3.3, as a function of jet multiplicity. For $W \rightarrow \mu\nu$, $Z \rightarrow \mu\mu$ is a relevant background, as a single muon missed due to inefficiency, or because the muon

Pre-selection	
Vertex	≥ 1 good vertex: $N_{\text{tracks}} \geq 3$
remove events affected by LAr noise burst and data corruption (larError < 2)	

Muon selection	
Triggers	EF_mu18_MG (D-I), EF_mu18_MG_medium (J-M)
Lepton	STACO combined muon
	$\lvert\eta\rvert < 2.4$
	$p_{\text{T}} > 20$ GeV (25 GeV in the W Channel)
Quality	B Layer Hits > 0 if track passes through B Layer
	(Pixel Hits + Dead Pixel Sensors) > 1
	(SCT Hits + Dead SCT Sensors) ≥ 6
	(Missed Hits for Pixel/SCT) < 3
	with N=(nTRTOutliers + nTRTHits)
	if $\lvert\eta\rvert < 1.9$ then require N>5 && nTRTOutliers/N < 0.9
	if $\lvert\eta\rvert \geq 1.9$ && N>5 then require nTRTOutliers/N < 0.9
Isolation*	$\sum \mathrm{p}_{\mathrm{T}}(\text{IDCone20})/p_{\text{T}} < 0.1$
Impact par*	$\lvert d_0\rvert / \sigma_{d_0} < 3.0$
**Isolation and impact parameter selections only applied to first selected muon.*	

$Z \to \mu\mu$ event selection	
W veto	no third selected muon
Charge	Opposite sign
Invariant Mass	$66 < m_{\mu_+\mu_-} < 116$ GeV

$W \to \mu\nu$ event selection	
Z veto	no second selected muon
$E_{\text{T}}^{\text{miss}}$cleaning	no jets from noise or beam halo
Missing energy	$E_{\text{T}}^{\text{miss}} > 25$ GeV
Transverse mass	$M_{\text{T}} > 40$ GeV

Table 3.1. Event selection for the muon channel. Quality criterion for $E_{\text{T}}^{\text{miss}}$cleaning are described in the text. Muon quality criteria are described further in Section 2.3.2.

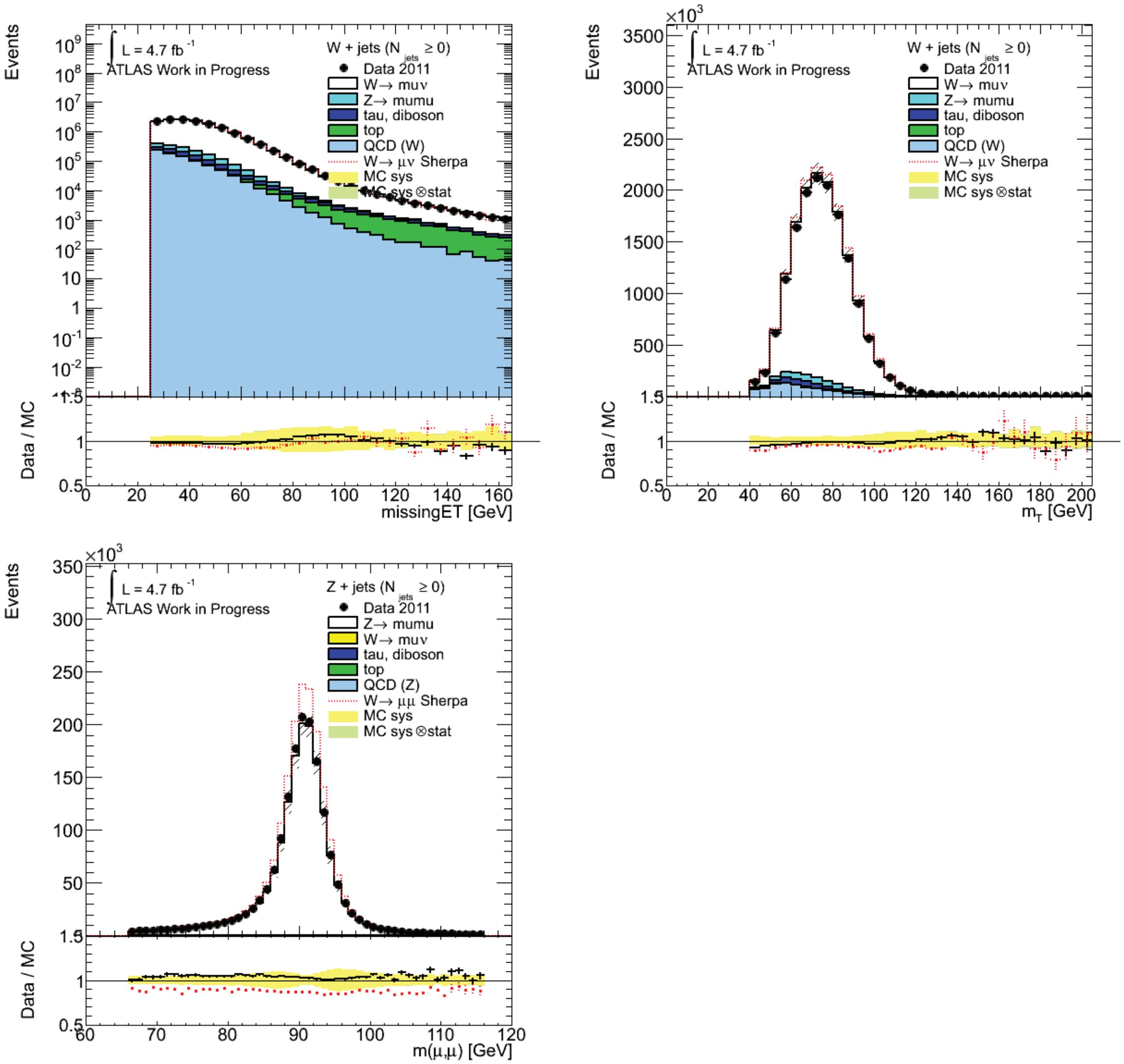

Figure 3.1. Muon channel detector level inclusive selection control plots. W selection: M_{T}, $E_{\mathrm{T}}^{\mathrm{miss}}$, Z selection: $m_{\mu_{+}\mu_{-}}$.

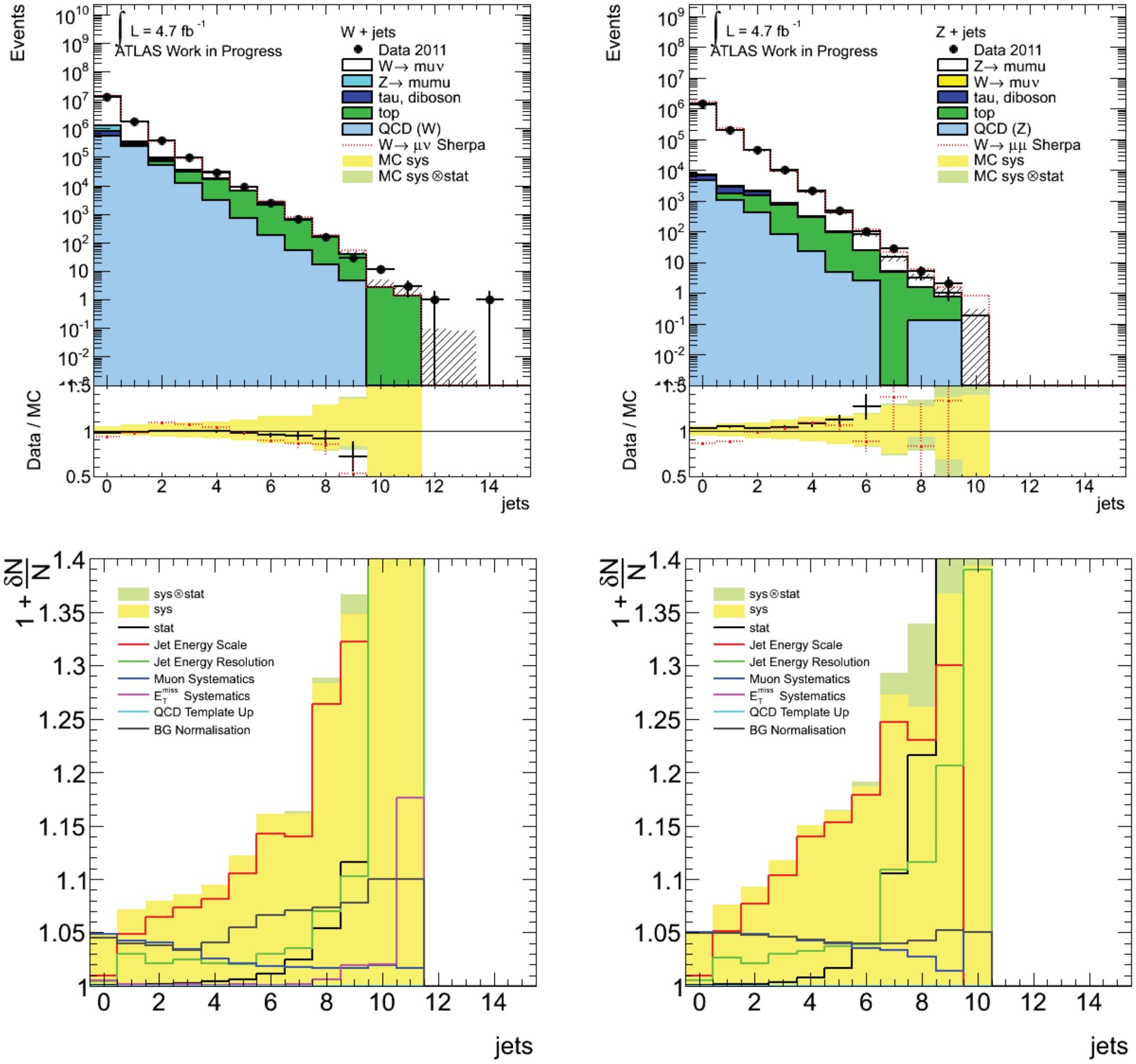

Figure 3.2. Muon channel detector level exclusive jet multiplicity N_{jet} in W and Z selection and its experimental systematic uncertainty breakdown.

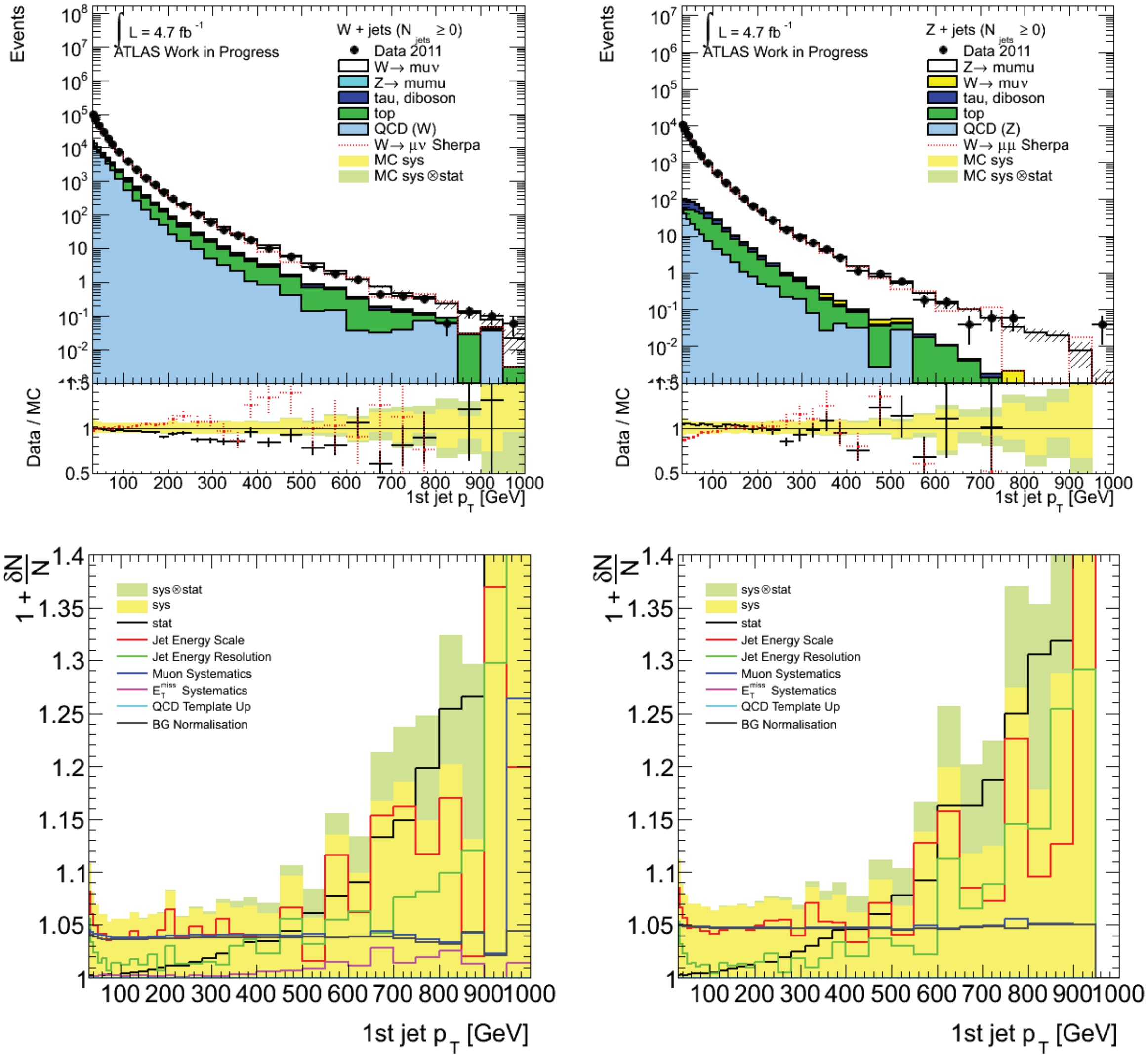

Figure 3.3. Muon channel detector level leading jet transverse momentum in W and Z selection and its experimental systematic uncertainty breakdown.

is out of detector acceptance, will lead to fake $E_{\mathrm{T}}^{\mathrm{miss}}$ in the event, as well as a single lepton signature. This contributes roughly 4% background to $W \to \mu\nu$. The multijet background is dominated by heavy flavor events with decays to real muons, as the isolation requirement rejects most other events. Multijet backgrounds are at the level of 20% for one or more jets in the event. For high jet multiplicity, $t\bar{t}$ is the dominant background. Top quarks always decay to a W boson and a b quark, so if one of those decays into leptons and the other to hadrons, four jets remain in the event. Additional partons in the interaction, and the fact that a jet can be below threshold lead top backgrounds to be significant for 3 or more jets.

	$N_{jet} = 0$	$N_{jet} = 1$	$N_{jet} = 2$	$N_{jet} = 3$	$N_{jet} = 4$	$N_{jet} = 5$	$N_{jet} = 6$	$N_{jet} = 7$
$W \to \mu\nu$	12118355 ± 659045	1370809 ± 109854	296325 ± 28034	59594 ± 7011	12137 ± 1791	2417 ± 425	452 ± 96	83 ± 17
$Z \to \mu\mu$	445188 ± 24295	56014 ± 4712	12321 ± 1247	2593 ± 330	539 ± 85	109 ± 20	21.4 ± 4.8	3.3 ± 1.1
Tau, Diboson	263359 ± 13933	46015 ± 2805	13051 ± 1063	2885 ± 349	583 ± 95	102 ± 19	15.2 ± 6.8	2.2 ± 1.3
Top	1040 ± 143	6251 ± 573	15693 ± 1088	18798 ± 1355	13009 ± 1192	5730 ± 690	1969 ± 310	540 ± 93
Multijet (W)	548635 ± 1374	245664 ± 756	52434 ± 317	12537 ± 147	3189 ± 72	737 ± 34	185 ± 17	55.1 ± 9.2
Total Predicted	13376577 ± 665426	1724753 ± 113996	389824 ± 29254	96407 ± 7636	29456 ± 2694	9095 ± 1054	2642 ± 400	684 ± 107
Data Observed	12997597	1702937	389751	96021	29176	8902	2523	645

Table 3.2. Number of events expected from Monte Carlo simulation and observed in data for several exclusive jet multiplicities for the $W \to \mu\nu$ selection. Multijet predictions are from a data-driven estimation, as described in section 3.6.1. The errors listed are the combined statistical and systematic uncertainties as described in Sections 3.6 to 3.10.

For the $Z \to \mu\mu$ channel, the backgrounds are very small, due to the requirement of two combined muons. $Z \to \tau\tau$ and diboson (WW,WZ,ZZ) backgrounds contribute a small but measurable background, around 1% and decreasing with jet multiplicity.

	$N_{jet} = 0$	$N_{jet} = 1$	$N_{jet} = 2$	$N_{jet} = 3$
$Z \to \mu\mu$	1365225 ± 70841	189596 ± 14029	41526 ± 3860	8508 ± 1004
$W \to \mu\nu$	545 ± 46	242 ± 20	85 ± 11	20.7 ± 4.8
Tau, Diboson	1791 ± 75	1091 ± 45	579 ± 42	133 ± 15
Top	102 ± 13	613 ± 60	1027 ± 84	629 ± 53
Multijet (Z)	4632 ± 36	1060 ± 13	414.7 ± 8.9	78.8 ± 3.2
Total Predicted	1372295 ± 70858	192601 ± 14005	43633 ± 3887	9370 ± 1036
Data Observed	1412518	200935	44917	9758

	$N_{jet} = 4$	$N_{jet} = 5$	$N_{jet} = 6$	$N_{jet} = 7$
$Z \to \mu\mu$	1688 ± 250	322 ± 56	56 ± 12	9.5 ± 3.0
$W \to \mu\nu$	4.9 ± 1.7	0.99 ± 0.33	0.66 ± 0.54	0.00 ± 0.00
Tau, Diboson	23.3 ± 3.3	3.81 ± 0.88	0.31 ± 0.16	0.24 ± 0.13
Top	271 ± 30	88 ± 12	21.5 ± 3.8	4.8 ± 1.8
Multijet (Z)	23.0 ± 1.7	4.91 ± 0.80	2.59 ± 0.58	0.00 ± 0.00
Total Predicted	2011 ± 273	419 ± 67	81 ± 15	14.6 ± 4.1
Data Observed	2162	470	102	29

Table 3.3. Number of events expected from Monte Carlo simulation and observed in data for several exclusive jet multiplicities for the $Z \to \mu\mu$ selection. Multijet predictions are from a data-driven estimation, as described in section 3.6.1. The errors listed are the combined statistical and systematic uncertainties as described in Sections 3.6 to 3.10.

The multijet background is small in this case, around the level of 1% and again decreasing with jet multiplicity. Top, particularly $t\bar{t}$, is a significant background for large jet multiplicities, though smaller than in the W channel due to the small branching ratio for $t\bar{t}$ to decay to two muons.

The following backgrounds are modeled by MC: $Z \to \mu\mu$, $W \to \mu\nu$, $Z \to \tau\tau$, $W \to \tau\nu$, diboson, $t\bar{t}$. Systematic uncertainties on these samples include a 1.8% luminosity uncertainty, uncertainty on the cross section of the sample, and uncertainty based on the MC statistics available. The luminosity uncertainty cancels completely when calculating R_{jet}.

3.6.1 Multijet Background Measurement

Large uncertainties are associated with the simulation of hadronic background, both due to cross section uncertainties, and due to difficulties in modeling the rate at which a jet, or a muon in a jet, will be reconstructed as an isolated muon. Due to these uncertainties, we adopt a fully data driven template method to model this background. Differences in shape between the $E_{\mathrm{T}}^{\mathrm{miss}}$ distribution in multijet events and in the W/Z signal are exploited to fit their relative fraction. A multijet control sample is selected by selecting events in data that pass all W event selection requirements, with the following exceptions: the $E_{\mathrm{T}}^{\mathrm{miss}}$ requirement is relaxed (but $M_{\mathrm{T}} > 40$ is still required), and selected muons are required to fail the d_0 selection ($d_0/\sigma_{d_0} < 3$), where d_0 is the radial impact parameter, in order to create a sample that is enriched in multijet background, while having similar kinematic properties as events passing W selection. The $E_{\mathrm{T}}^{\mathrm{miss}}$ templates for signal, electroweak, and top backgrounds are derived from MC. The data, with only the $E_{\mathrm{T}}^{\mathrm{miss}}$ selection relaxed, is then fit to these two distributions to determine their relative fraction. The fit is performed in the range from 10 to 100 GeV.

A similar method is employed for multijet estimation in the Z channel, with the dilepton invariant mass used as the fitting variable instead, with a range from 45 to 120 GeV. Due to the lower statistics in the Z channel, the isolation selection is reversed in this case instead of the d_0 selection to define the multijet enriched sample. In both channels, the fit is performed as a function of the number of jets in the event. This fit is performed for exactly zero to two jets in the Z channel, and also for events with three or more jets. In the W channel, the fit is performed for exactly zero to four jets, and also for events with five or more jets.

Figure 3.4 shows the $E_{\mathrm{T}}^{\mathrm{miss}}$ distribution in data, including the fit to the multijet and signal contributions. This fit is repeated for each jet multiplicity. For the Z channel, the plots have a strange shape below 40 GeV, this is because MC generator places a cut on the invariant mass of 40 GeV. The shape of the multijet background for each kinematic variable (jet p_{T}, jet rapidity, etc) is estimated as follows: The distribution is found by applying the multijet template selection in data, but requiring all other event selection criteria (including $E_{\mathrm{T}}^{\mathrm{miss}}$ or $m_{\mu+\mu-}$). This distribution is then scaled using the multijet scale factor found from the template fit, as a function of the jet multiplicity.

Tables 3.4 and 3.5 show multijet fraction for each jet multiplicity, and the fractional uncertainty from systematic variations. Systematic uncertainties are estimated by varying the fit ranges, the choice of fit variable, and the selection of the multijet control sample. The lower fit range is varied up and down by 5 GeV, and the upper range is varied by 10 GeV. The alternate fit variable used is the angle $\Delta\phi$ between the leading lepton and the vector sum of all the selected jet momenta. Alternate templates include an anti-d_0 template (Z channel), an anti-isolation template (W channel), relaxing the z_0 requirement, and "restricted" anti-isolation, which is defined by the following requirement: $0.1 < \Sigma p_{\mathrm{T-cone-0.2}}/p_{\mathrm{T}} < 0.5$. As the system-

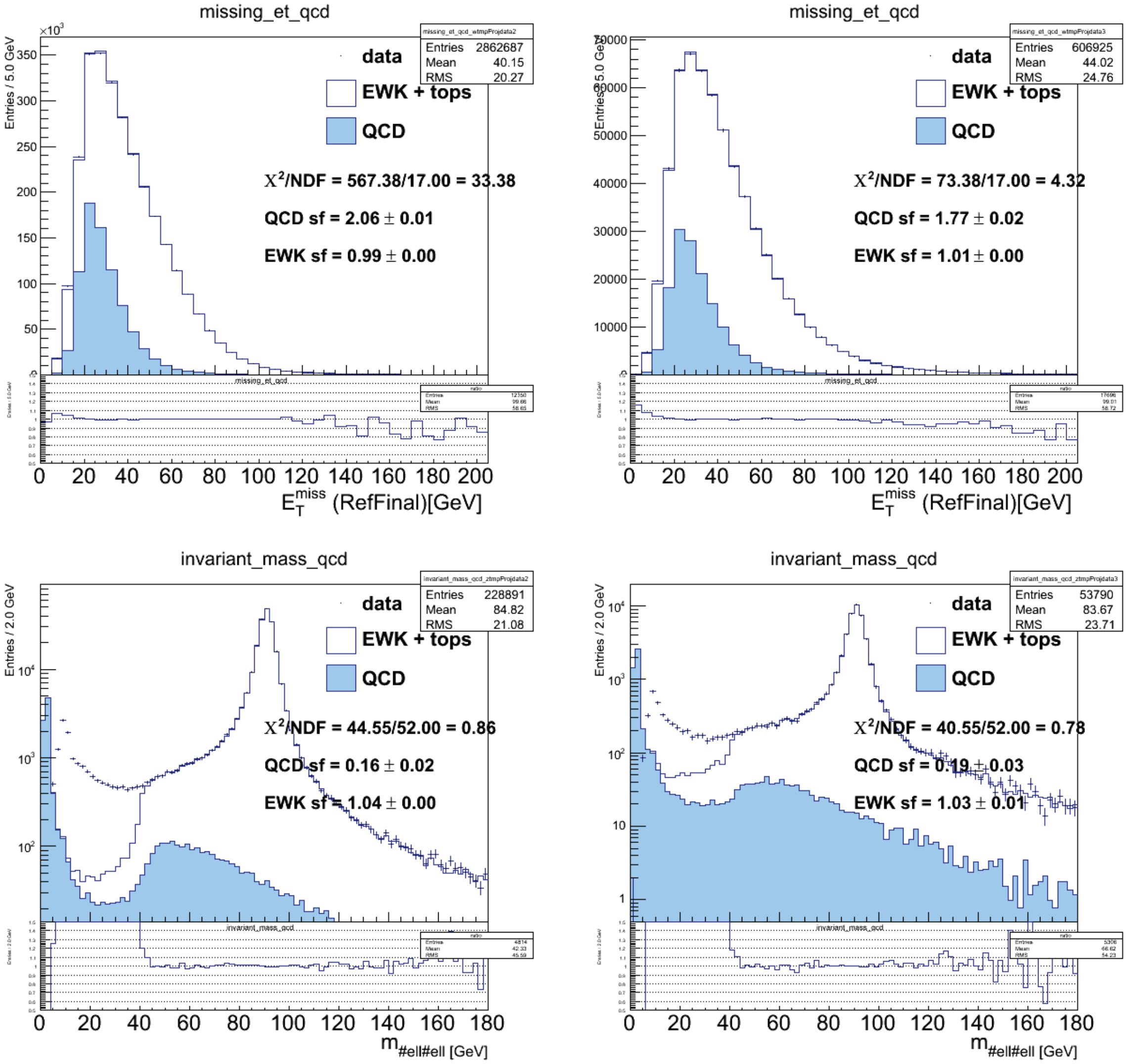

Figure 3.4. Template fits to determine the multijet fraction for the W channel(top) and Z channel(bottom). Fits shown are for exactly one jet (left) and exactly two jets (right). The bottom portion of each plot shows the ratio of the data to the MC prediction.

QCD Fraction	Njet = 0	Njet = 1	Njet = 2	Njet = 3	Njet = 4	Njet = 5
Nominal	0.0410	0.1424	0.1345	0.1301	0.1084	0.0806
Fractional Systematic Error on the QCD Fraction						
Fit Range Up	0.0025	0.0008	0.0024	0.0068	0.0441	0.0159
Fit Range Down	-0.0165	-0.0110	-0.0156	-0.0392	-0.0135	-0.0235
Alt Fit Variable	0.0000	-0.1014	-0.1728	-0.2648	-0.4682	-0.5283
Template Up	0.1215	0.0073	0.0101	0.0121	0.0153	0.0034
Template Down	-0.4971	-0.1405	-0.1702	-0.1698	-0.2638	-0.2921
Total Systematic	0.4971	0.1405	0.1728	0.2648	0.4682	0.5283

Table 3.4. W channel QCD fractions and systematic uncertainties, derived from varying the fit range, template selection, and fit variable.

Systematic	Njet = 0	Njet = 1	Njet = 2	Njet = 3
Nominal	0.0034	0.0055	0.0095	0.0084
Fractional Systematic Error on the QCD Fraction				
Fit Range Up	0.0750	0.0127	0.0108	0.0181
Fit Range Down	-0.0040	-0.0037	0.0000	-0.1193
Alt Fit Variable	0.0445	0.0117	-0.6365	-0.9117
Template Up	0.0947	0.0000	0.0224	0.0423
Template Down	-0.0029	-0.0089	-0.0946	-0.0471
Fit Stat Error	0.0585	0.1076	0.1556	0.4568
Total Systematic	0.0947	0.1076	0.6365	0.9117

Table 3.5. Z channel QCD fractions and systematic uncertainties, derived from varying the fit range, template selection, and fit variable.

atic uncertainties evaluated by these variations are likely correlated, the symmetrized envelope of variations is take as the systematic uncertainty on the multijet fraction.

3.7 Trigger Efficiency

The triggering and data acquisition system of ATLAS is described in detail in Section 2.2.4. A single muon trigger was used for the whole data taking period. An event filter (EF) trigger requiring a muon with p_{T} greater than 18 GeV was used, which had the title EF_mu18_MG, until run 186729. Because of higher luminosity, after this run, a more restrictive trigger was used: EF_mu18_MG_medium. The difference between these two triggers was the hardware-based (L1) trigger feeding them: the first trigger requires a 10 GeV muon at L1, whereas the medium chain requires an 11 GeV muon at L1.

Single muon trigger efficiency was measured from data using "tag-and-probe" methods using $Z \rightarrow \mu\mu$ events. The power of this method stems from the fact that requiring two tracks inside the Z mass window, with one track belonging to a combined "tag" muon, defines a sample of Z events with very high purity. Therefore, the second track should also belong to a muon, and depending on the definition of the second track, or "probe", this allows for the measurement of the trigger efficiency, ID track efficiency, or MS and track matching efficiency. In the case of determining trigger efficiency, both the tag and the probe are required to be combined muons, and the tag muon is required to fire the trigger. The probe muon is tested as to whether it also fired the trigger in question, to determine the trigger efficiency.

Combined muon definitions for trigger studies match the tight muon description in Section 2.3.2, with the exception that the d_0 requirement is dropped. The probe has the following additional requirements:

- opposite charge with respect to the tag
- $\left|M_{(\mathrm{tag-probe})} - M_{\mathrm{Z}}\right| < 10$ GeV
- $\Delta\phi(tag - probe) > 2$
- $\Delta z_0(tag - probe) < 3\,\mathrm{mm}$
- $\Delta d_0(tag - probe) < 2\,\mathrm{mm}$

The single-muon trigger efficiency is calculated for MC and data, and is calculated as a function of momentum and pseudorapidity. These efficiencies are used to calculate event level scale factors that correct the trigger efficiency of the MC samples. Event level efficiencies for the W are just the single lepton efficiencies. For the

Z, the efficiency is equal to probability that either lepton triggered the event. The resultant scale factors are applied to any distribution where a trigger requirement has been made. Muon trigger efficiencies have been determined to be independent of jet activity, except for the effects mediated by muon kinematics, which are taken into account.

In order to pass the event selection, at least one selected lepton must be ΔR matched to the trigger muon that fired the required trigger. This is in order to reject events for which some other non-selected muon initiated the trigger, because these events would not be reflected in efficiency studies. In practice, this is a very small effect.

The following were varied when calculating the systematic uncertainties: the p_{T} range over which the efficiencies were calculated, the bin size, and the muon selection criteria. The resulting uncertainty is approximately 1%. The systematic and statistical uncertainty from the measurement are added in quadrature and are used to define systematic variations of the muon trigger efficiency on the final measurement.

3.8 Muon Reconstruction Efficiency

The muon W/Z selection efficiency is corrected for the mismatch between reconstruction efficiency in data and Monte Carlo simulation. Single muon reconstruction efficiency is determined with tag-and-probe methods similar to those used to determine the trigger efficiency. Separate studies were done to determine the ID track efficiency, and the Muon Reconstruction and track matching efficiency relative to this.

To determine the ID efficiency for muons, the probe was defined as a standalone muon track extrapolated to the primary vertex. The kinematic, isolation, impact parameter, and other probe selection criteria are the same as those used trigger efficiency studies. These probes are matched to ID tracks passing the same kinematic

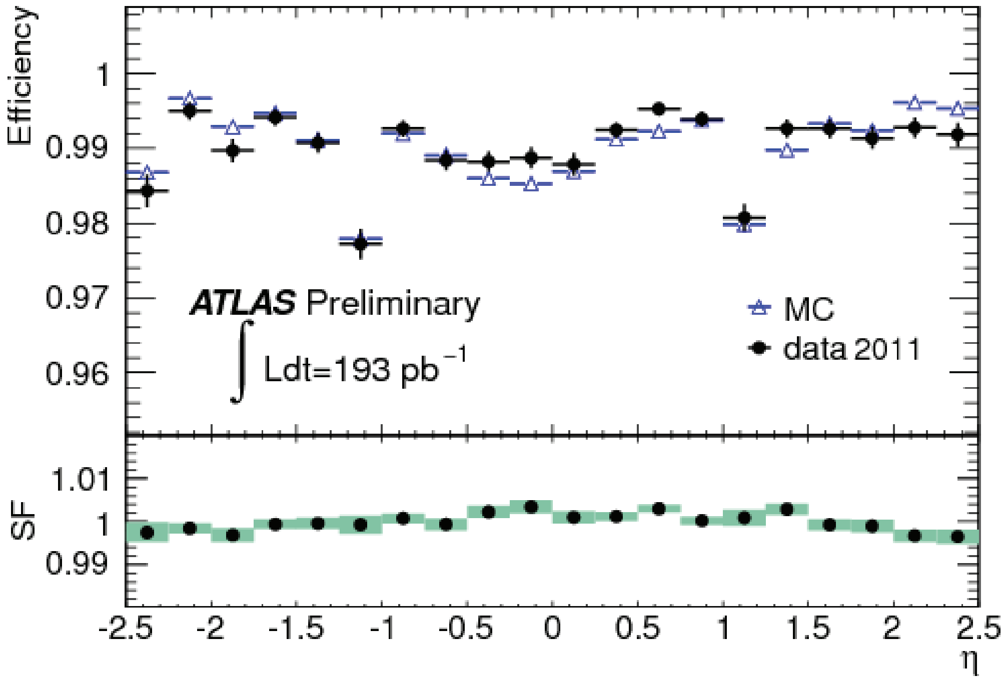

Figure 3.5. Measured inner detector muon reconstruction efficiency for muons with $p_{\mathrm{T}} > 20\,\mathrm{GeV}$ as a function of the muon's pseudorapidity.

selections used to select muons from W and Z decays. The hit requirements specified in Section 2.3.2 are not applied here to avoid double counting. Figure 3.5 shows a measurement of the ID efficiency for muons as a function of η, for a subset of the 2011 data (193 pb^{-1}).

To determine the combined muon efficiency relative to the ID efficiency (the muon tracking efficiency and the matching efficiency), an ID track was used for the probe, once again with the same kinematic, isolation, and impact parameter requirements. These probes are matched to combined muons, including hit requirements. Systematic uncertainties are determined by using muons identified by the calorimeter as the probe for comparison, which have higher purity than ID tracks. A minimum of 0.1% uncertainty is applied to all bins to cover very small variations that occur when varying the tag and probe selections. Figure 3.6 shows the combined muon efficiency

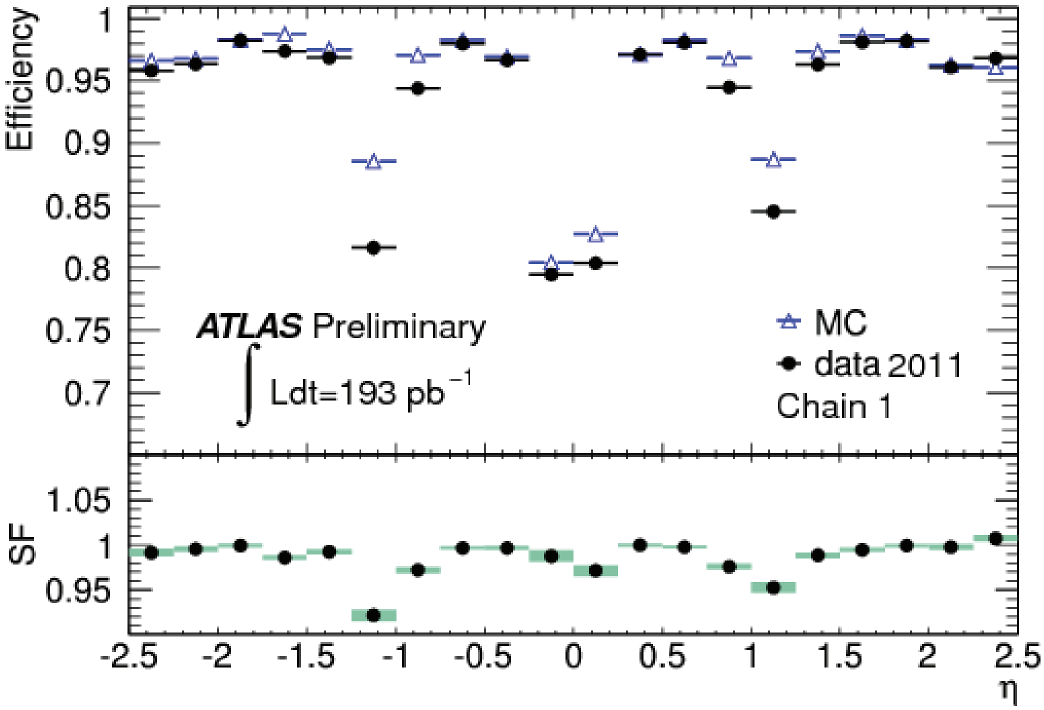

Figure 3.6. Combined muon reconstruction efficiency with respect to the inner tracking efficiency as a function of the pseudorapidity of the muon for muons with $p_{\mathrm{T}} > 20\,\mathrm{GeV}$. The panel at the bottom shows the ratio between the measured and predicted efficiencies.

relative to the ID efficiency as a function of η, for a subset of the 2011 data (193 pb^{-1}).

The reconstruction efficiency used in this analysis is divided into 10 bins using a phenomenological scheme in η and ϕ corresponding to the different detector elements traversed by a muon in that region of solid angle. The $\eta - \phi$ distribution of these is shown in Figure 3.7. The Muon Spectrometer is described in detail in Section 2.2.3. For each bin, the bin name and description of involved detector elements is listed below:

- Barrel large: large barrel stations
- Barrel small: small barrel stations
- Barrel overlap: overlap between small and large barrel stations

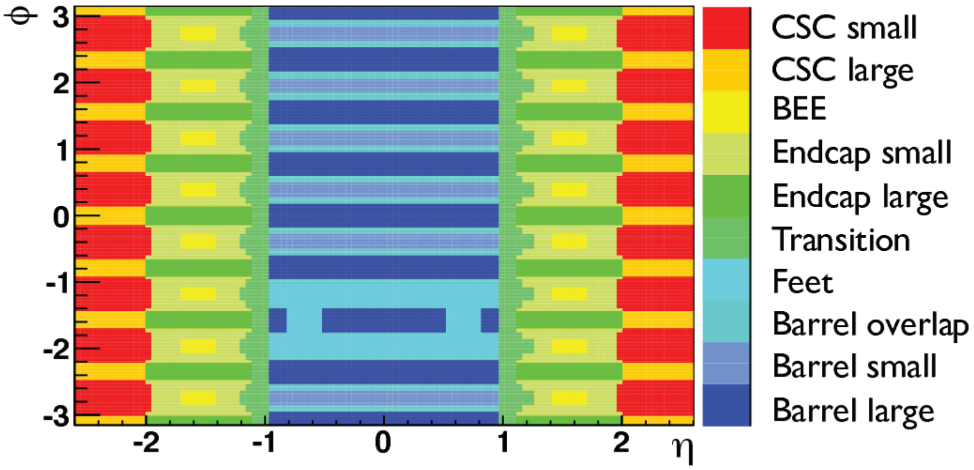

Figure 3.7. Coverage in $\eta-\phi$ of ten detector regions, used for binning muon efficiency and resolution measurements.

- Feet: region of the feet supporting the detector (some chambers are missing in this region which makes the muon reconstruction more difficult)
- Transition: transition region between the barrel part and the endcap wheels
- Endcap small: small endcap sectors, MDT chambers
- Endcap large: large endcap sectors, MDT chambers
- BEE: sectors containing barrel extended endcap chambers
- CSC small: small endcap sectors, CSC chambers, outside TRT acceptance
- CSC large: large endcap sectors, CSC chambers, outside TRT acceptance

Once again, the single muon efficiencies are used to determine event level scale factors that are applied to the simulation samples. The systematic and statistical uncertainty from the measurement are added in quadrature and are used to define systematic variations of the muon reconstruction efficiency on the final measurement.

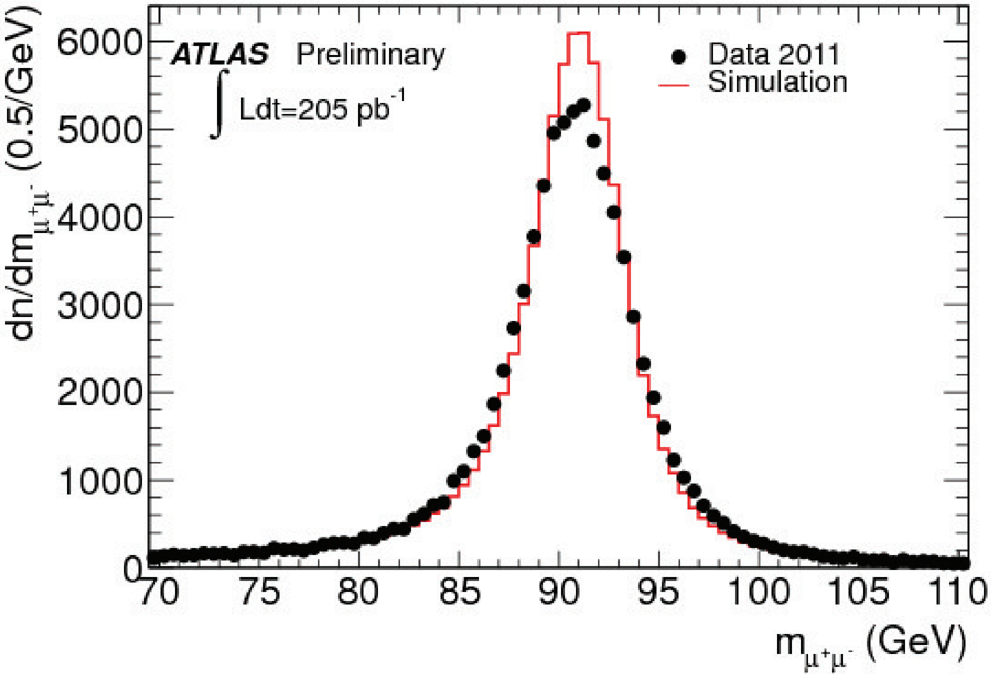

Figure 3.8. Dimuon invariant mass distribution for oppositely charged muon pairs with transverse momentum above 20 GeV. Selection details are given in the text.

3.9 Muon Momentum Scale and Resolution

The resolution of muon momentum is not perfectly modeled by the simulation. Therefore, before muon selection is performed in simulated samples, all muons have their p_{T} smeared and scaled by factors determined from Z dilepton invariant mass measurements. These factors are chosen to reproduce the width and central position of the invariant mass peak, and are measured as a function of p_T and as a function the broad bins in η and ϕ described in Figure 3.7, which follow variations in the structure of the Muon Spectrometer detector elements. Muon spectrometer and Inner Detector momentum measurements each undergo this smearing/scaling procedure, and the combined momentum is recalculated from these elements. Systematic variations based on the statistical and systematic uncertainty of the resolution measurement are performed on the final R_{jet} measurements.

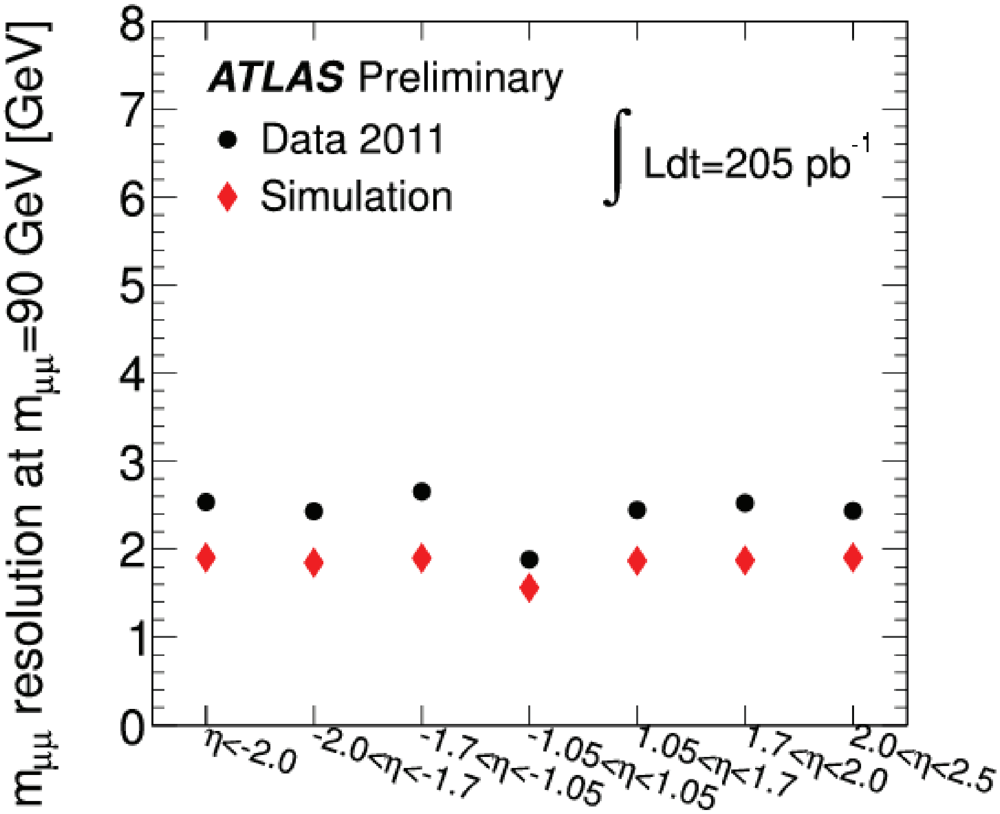

Figure 3.9. Dimuon mass resolution of combined muons in different pseudorapidity regions.

Figure 3.8 shows the dimuon invariant mass distribution for oppositely charged combined muon pairs with transverse momentum above 20 GeV. Both muons are restricted to $|\eta| < 2.5$. Collision events are selected from event filter triggers of 20 GeV threshold. The measured dimuon mass is compared to Monte Carlo prediction using Pythia generated $Z \to \mu\mu$ events. Figure 3.9 shows the experimental resolution compared to Monte Carlo predictions as a function of pseudorapidity.

3.10 Jet Energy Scale and Resolution

The reconstruction of jets using the anti-kt algorithm as described in Section 2.3.3 produces jets for which the energy contained in the charged particles in the showers is properly accounted for. The hadronic calorimeter is “non-compensating”, which means it does not correct for non-interacting decay products which do not leave their energy in the detector. Electromagnetic showers have their energy properly accounted for, but hadronic showers do not. Therefore, it is preferable to use a jet energy scale that more closely matches the energy of the gluon or quark from which the jet originated. For this reason, an additional sequence of calibrations are applied:

- Pileup Correction: Minimum-bias interactions leave additional energy in the detector. This energy is determined using minimum-bias events and subtracted from jet energy.
- Particle Level Correction: This correction is determined from MC, using a numerical inversion of the relationship between particle p_{T} and reconstructed jet p_{T}.
- In-situ Correction: This is only applied to data, and is a residual correction derived from the data as described below.

Measurements of this JES are validated by comparing the fraction of jet energy in the EM calorimeter in data and in simulation. In addition, measurements of asymmetry in jet events can be related to defects in calorimeter response. Within uncertainties there is good agreement between data and MC, and these studies are used to derive systematic uncertainties on the jet energy scale (JES), and to define the small in-situ correction. The jet energy spectrum is also measured in dijet studies, and shows good agreement between data and simulation, suggesting that no additional smearing of the jets is needed. The measured uncertainty in the resolution measurement of jets is used to create an over-smeared set of jets used to estimate the systematic uncertainty associated with the jet energy resolution (JER).

3.11 Monte Carlo Description and Systematics

Hadron level results used for unfolding come from Alpgen MC samples, as described in Section 3.1. Truth level jets are defined using the same anti-k_T clustering algorithm described in Section 2.3.3, using all of the interacting particles originating from the primary collision as inputs, with the exception of the W/Z decay products. Truth leptons are defined as "dressed" leptons as follows: photons originating from the boson, and within a cone of $\Delta R < 0.1$, have their 4-momenta added to that of the final state lepton. Because electrons are largely measured through the calorimeter systems, this closely matches what is measured by the reconstructed electron. For muons, energy lost in the calorimeter is taken into account when the combination of Inner Detector and Muon Spectrometer tracks is performed, but in practice the correspondence between dressed muons and detector muons is not as strong as in the electron case. Dressed muons are still used in this case to keep methods parallel between the muon and electron channel, and for theoretical clarity. As mentioned, dressed level results make the same kinematic requirements on leptons, $E_{\mathrm{T}}^{\mathrm{miss}}$ and jets as at detector level.

Final theoretical predictions are provided by BlackHat, with Sherpa used for showering. These predictions are given before the emission of any final state radiation, often referred to as Born level. A small correction factor is derived from Alpgen MC and applied to the BlackHat+Sherpa result to allow direct comparison with the dressed level measured result. BlackHat+Sherpa also does not model hadronization, nor does it model the evolution of beam remnants and of multiple interactions, which together are termed "underlying event". Corrections for these differences are calculated using Alpgen signal samples with these effects turned on and off. The underlying event (UE) correction is defined by (hadron level, UE on) / (hadron level, UE off), where as the hadronization correction is defined by (hadron level, UE off) / (parton level, UE off). Examples of these corrections are shown in Figures 3.10

and 3.11. Corrections derived with Sherpa are used to estimate the systematic uncertainty. MC simulation and the involved theoretical calculations are described in detail in Section 1.9.

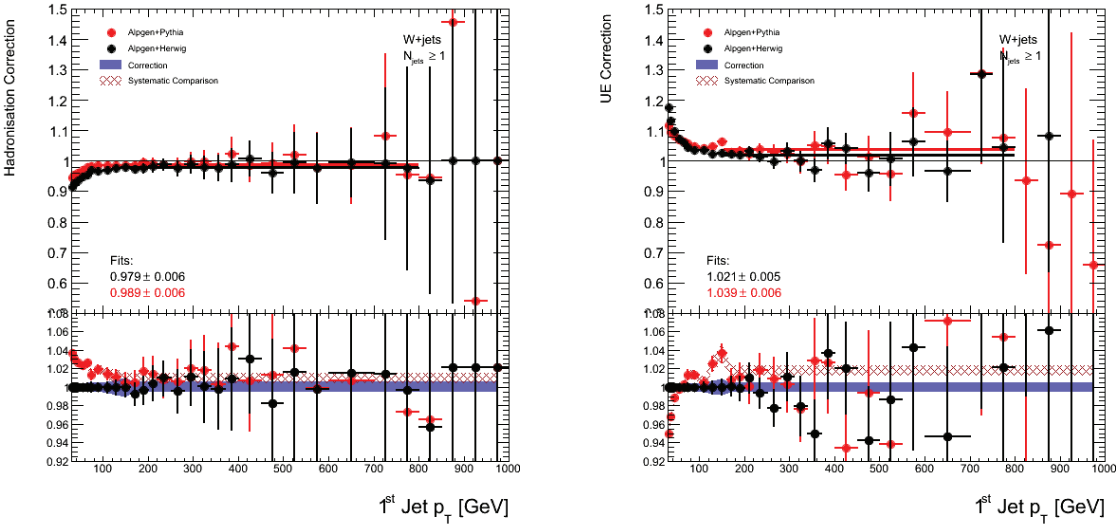

Figure 3.10. Corrections applied to the BlackHat+Sherpa theory inputs: hadronization (left), and underlying event (right). The black points for the top portion of the plot are nominal correction values, with the red the corrections calculated by Sherpa, used as a systematic uncertainty. The correction for high p_{T} is calculated using a fit to a straight line. The bottom portion of the plot shows the ratio between the calculated fit and the individual data points. The blue band represents the statistical error, and the red band the systematic error.

Some systematic uncertainty on the theoretical predictions exists due the our imperfect knowledge of the following parameters: PDF sets, renormalization scale, factorization scale and α_s, the strong coupling constant. To determine these uncertainties, the BlackHat+Sherpa theoretical calculation can be repeated with each parameter varied within their uncertainties. For technical reasons, the theorist providing these predictions was unable to provide these varied inputs within the current time-frame, and as such they are not included in the current version of this thesis. These parameters impact W and Z events in a nearly identical fashion, and as such, the effect on the ratio R_{jet} is very small. The impact of all these effects on the 2010

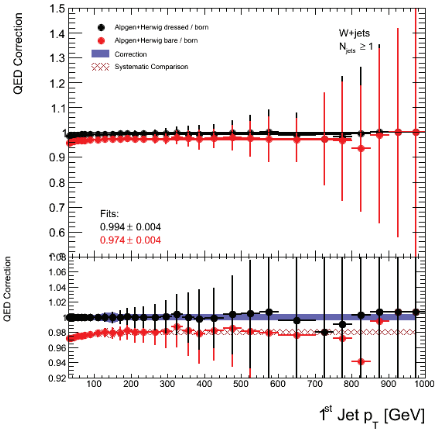

Figure 3.11. The FSR QED correction applied to the BLACKHAT+SHERPA theory inputs. On the upper half, the black points are the correction for born to dressed muons, whereas the red points are the correction from born to bare. The correction for high p_T is calculated using a fit to a straight line. The bottom portion of the plot shows the ratio between the calculated fit and the individual data points. The blue band represents the statistical error, and the red band the systematic error.

measurement as a function of lead jet p_T [7], was a 5-7% uncertainty on the W and Z cross sections, but only a 1-2% uncertainty on R_{jet}. As such, we expect these uncertainties to be much smaller than our dominant uncertainties.

3.12 Unfolding Methods

We aim to determine the "true" theoretical distribution of R_{jet} from the measured distribution, which includes detector effects including imperfect resolution and efficiency. The most straightforward solution to this is to apply what is termed a "bin-by-bin" correction. The ratio of the measured to the true cross section for each bin is determined individually, and this is used correct the measured cross-sections. This approach, however, completely discounts migration between the different bins, and for this reason is only valid if the migrations are small. The obvious solution is to treat this as a matrix problem, solved by the inversion of the transformation between truth and reconstructed quantities. This suffers from the problem that statistical fluctuations in the migration matrix will be interpreted as real structure, which is a serious problem as we determine the migration matrix from MC with limited statistics.

To solve this problem, we turn to Bayes' Theorem, using the method proposed by D'Agostini [46]. Bayes' theorem is a statement of conditional probability, typically written as:

$$P(A|B) = \frac{P(B|A)P(A)}{P(B)}. \tag{3.3}$$

In our case, this theorem can be rewritten as:

$$P(T_i|R_j) = \frac{P(R_j|T_i)P(T_i)}{\sum_\ell P(R_j|T_\ell)P(T_\ell)}, \tag{3.4}$$

where R_j is the j-th bin of measured distribution in data, T_i is the i-th bin of the truth distribution, so that $P(R_j|T_i)$ is the conditional probability of measuring some reconstructed value given a particular truth value. This matrix is measured from MC and termed the migration matrix. $P(T_\ell)$ is the unknown truth distribution, but as with other Bayesian procedures, we make a guess as to this distribution known as a "prior". We take the prior as the prediction from MC. This can be used to calculate $P(T_i|R_j)$, which can in turn be used to make a prediction for the truth distribution, given the measured distribution. The procedure can now be iterated using the recalculated $P(T_i)$. The result converges to the true value with a small number of iterations.

The migration matrices for the jet multiplicity distribution are shown in Figure 3.12. There is a trade off with the number of iterations, due to the fact that there is a tendency for areas of phase space with low statistics to diverge with more iterations due to a poorly defined migration matrix. We use two iterations as the default value. We have also tested an approach using a number of iterations that is optimized as follows: for each bin, the iterations are stopped when the statistical fluctuation is larger than the nominal value for the last two iterations. The two approaches produce similar results.

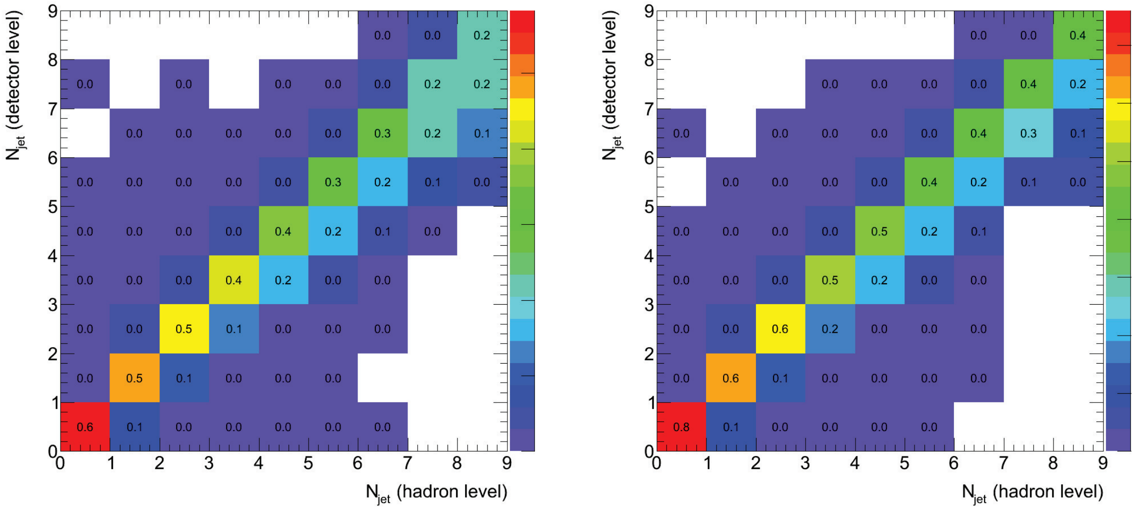

Figure 3.12. Migration matrices for W (left) and Z (right) events for exclusive jet multiplicity. Columns are normalized to the reconstruction efficiency for that truth jet multiplicity.

Systematic uncertainties on the unfolding method are measured as follows. First, estimates of the statistical uncertainty of the migration matrix are made by varying the migration matrix within its uncertainties, repeating the unfolding, and taking the maximum deviation for each bin. Second, an estimation of the uncertainty on the modeling of the migration matrix is made by performing the unfolding using migration matrices from an alternative generator, SHERPA. Finally there are uncertainties on the method itself. The number of iterations is an arbitrary value for this method: in an ideal world the result converges with increasing iterations. In practice, the effect of statistical fluctuations becomes enhanced as the iterations increase. For this reason we take the difference between 2 and 3 iterations as a systematic uncertainty. For the last systematic uncertainty on the unfolding, the bin-by-bin method of unfolding is compared to the nominal result, and the difference is taken as a systematic uncertainty. In most cases, while the bin-by-bin and Bayesian methods diverge somewhat for the individual W or Z channel, in the ratio, the methods agree fairly well due to cancellation between the two channels.

3.13 Systematics Summary

In order to preserve correlations between the W and Z channels, for each systematic uncertainty, the variation is applied to simultaneously to both channels, and R_{jet} is recalculated. This value is compared to the nominal value of R_{jet} to estimate the uncertainty. Due to low statistics, after taking the ratio some uncertainties have very large values in a few bins due to fluctuations in some regions of phase space. Therefore, the corresponding deviations $\mathcal{D}^k(\mathcal{O}_i)$ with respect to the nominal results are smoothed using Gaussian kernels, where k identifies the systematic uncertainty source,

$\mathcal{O}$ is a given variable, and i identifies a bin of the variable $\mathcal{O}$:

$$\begin{aligned}\tilde{\mathcal{D}}^k(\mathcal{O}_i) &= \frac{\sum_{j=1}^{N_{\text{bins}}} \mathcal{D}^k(\mathcal{O}_j) \cdot \mathcal{W}(\mathcal{O}_i,\, \mathcal{O}_j)}{\sum_{j=1}^{N_{\text{bins}}} \mathcal{W}(\mathcal{O}_i,\, \mathcal{O}_j)}, \\ \mathcal{W}(\mathcal{O}_i,\, \mathcal{O}_j) &= w(\mathcal{O}_j) \times \text{Gaus}\left(\frac{S(\mathcal{O}_i) - S(\mathcal{O}_j)}{\sigma_{\mathcal{O}}}\right), \end{aligned} \tag{3.5}$$

where $\tilde{\mathcal{D}}^k(\mathcal{O}_i)$ are the smoothed deviations, $w(\mathcal{O}_j)$ are a set of weights with $\sum_{j=1}^{N_{\text{bins}}} w(\mathcal{O}_j) = 1$, $\text{Gaus}(\cdot)$ is a Gaussian with $\mu = 0$ and $\sigma = 1$, $S(\cdot)$ is a function used to change the scale of $\mathcal{O}$, and $\sigma_{\mathcal{O}}$ is the width of the Gaussian kernel for the variable $\mathcal{O}$. Weights $w(\mathcal{O}_j)$ are computed from the statistical uncertainties $\delta\sigma(\mathcal{O}_j)$ on the nominal unfolded results:

$$w(\mathcal{O}_j) = \frac{1/(\delta\sigma(\mathcal{O}_j))^2}{\sum_{j=1}^{N_{\text{bins}}} 1/(\delta\sigma(\mathcal{O}_j))^2}. \tag{3.6}$$

The S function is taken as the natural logarithm if the variable $\mathcal{O}$ is a p_{T}-like variable: $S(\mathcal{O}) = \ln \mathcal{O}/1$ GeV. In the other cases, it is the identity. Values of $\sigma_{\mathcal{O}}$ are chosen for each variable such that the smoothing catch the shape of the deviations while introducing a stability with respect to statistical fluctuations. These values vary between 0.2 and 0.8.

Figure 3.13 shows the systematic uncertainties on the cross section as a function of leading jet rapidity for the W channel, the Z channel, and for R_{jet} both before and after smoothing. The jet uncertainty term includes both JES and JER contributions. The muon term includes contributions from the trigger efficiency, reconstruction efficiency, muon resolution and muon scale. The $E_{\mathrm{T}}^{\mathrm{miss}}$ term includes only the effect of soft $E_{\mathrm{T}}^{\mathrm{miss}}$ terms. The background term includes both cross section uncertainties and the uncertainty associated with the data driven multijet estimate. Jet related uncertainties are far higher than other uncertainties before taking the ratio. After taking the ratio, it is significantly reduced.

Figure 3.14 shows the smoothed systematic uncertainties on R_{jet} as a function of the jet rapidity for the 1st, 2nd, 3rd, and 4th leading jet. In each of these distributions, the jet and unfolding related uncertainties are dominant at high rapidity. Muon and background uncertainties are flat as a function of jet rapidity, and are significant in the central region of the detector. The background uncertainty is higher for high jet multiplicity. This is primarily because the $t\bar{t}$ background is dramatically larger in the W channel at high jet multiplicity, and correspondingly, the effect of the cross section uncertainty becomes larger. In addition, the multijet estimation uncertainty becomes larger at high jet multiplicity, but this has a smaller effect because of the smaller overall size of the multijet background.

Figure 3.15 shows the smoothed systematic uncertainties on R_{jet} as a function of the jet p_{T} for the 1st, 2nd, 3rd, and 4th leading jet. In each of these distributions, the jet and unfolding related uncertainties increase as a function of p_{T}, and are dominant at high p_{T}. Muon and background uncertainties are more flat as a function of jet p_{T}. The background uncertainty increases and then levels out as p_{T} increases. This

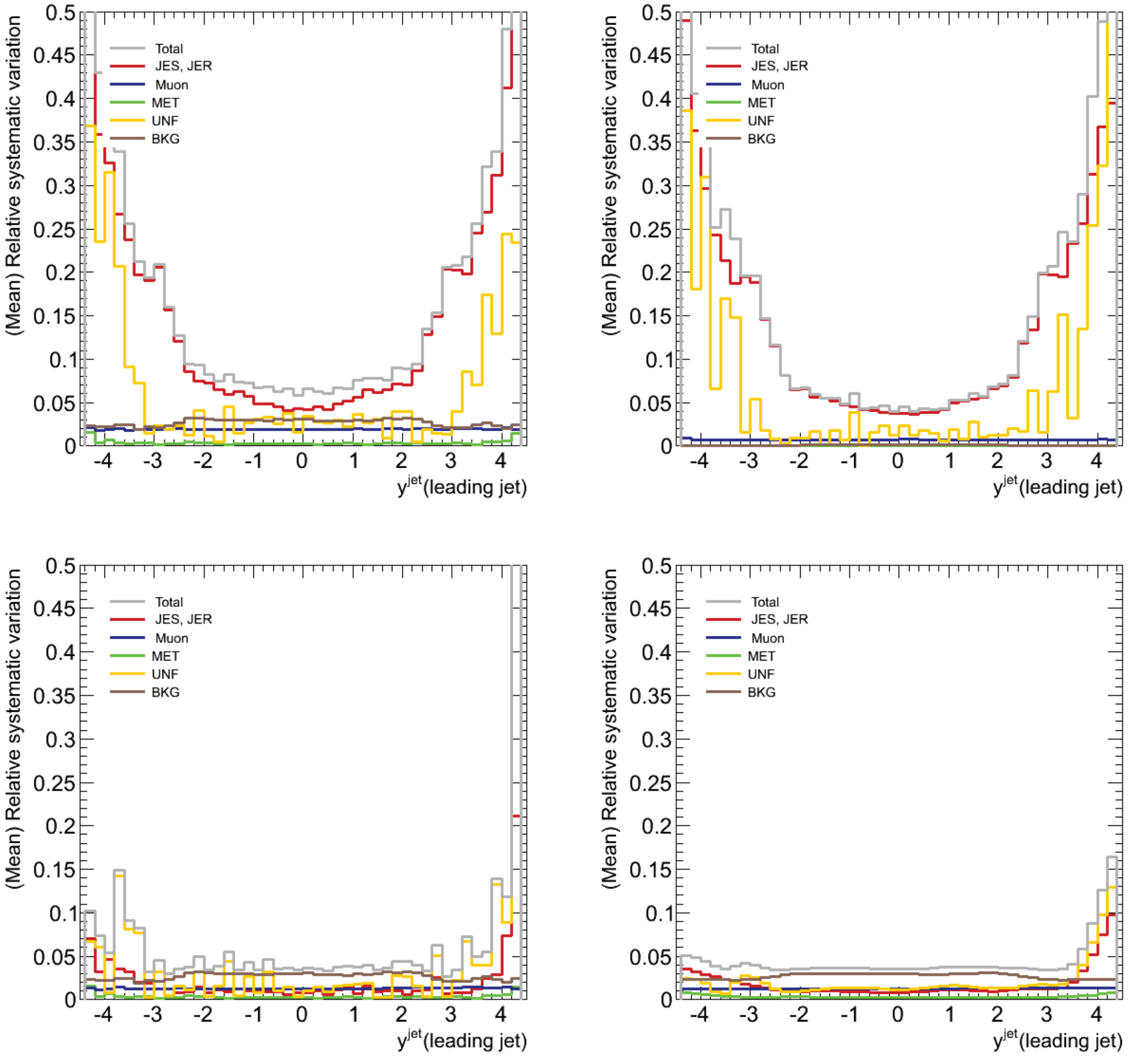

Figure 3.13. Systematic uncertainty contributions to the unfolded cross sections for W (top left), Z (top right), R_{jet} before smoothing (bottom left) and R_{jet} after smoothing (bottom right). Calculation of systematic uncertainties is discussed in detail in the text.

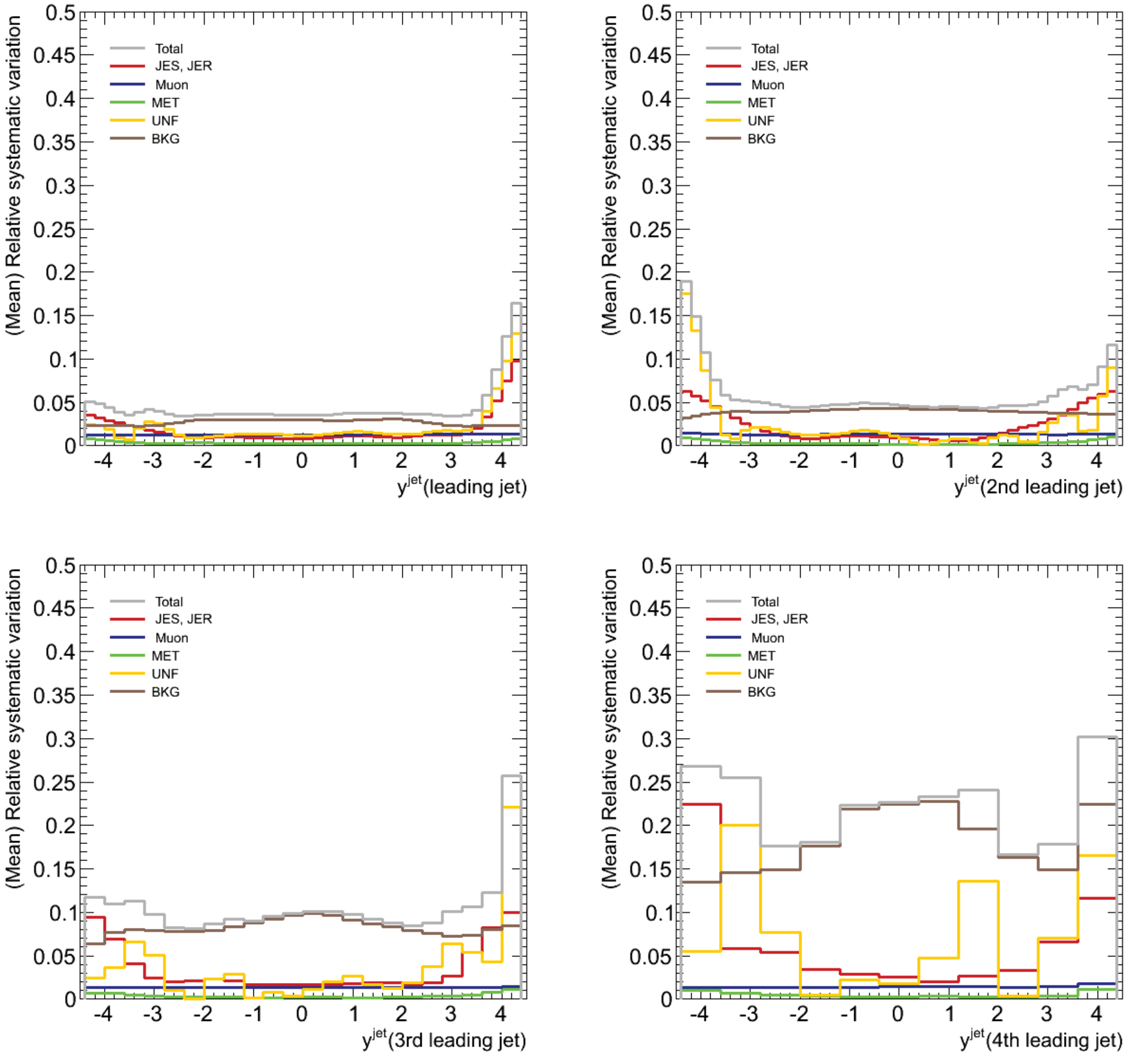

Figure 3.14. Systematic uncertainty contributions to R_{jet} for jet rapidity of the 1st (top left), 2nd (top right), 3rd (bottom left) and 4th (bottom right) leading jets. Calculation of systematic uncertainties is discussed in detail in the text.

is because the probability of additional jets above 30 GeV increases as p_{T} increases, and the the background uncertainty increases with multiplicity.

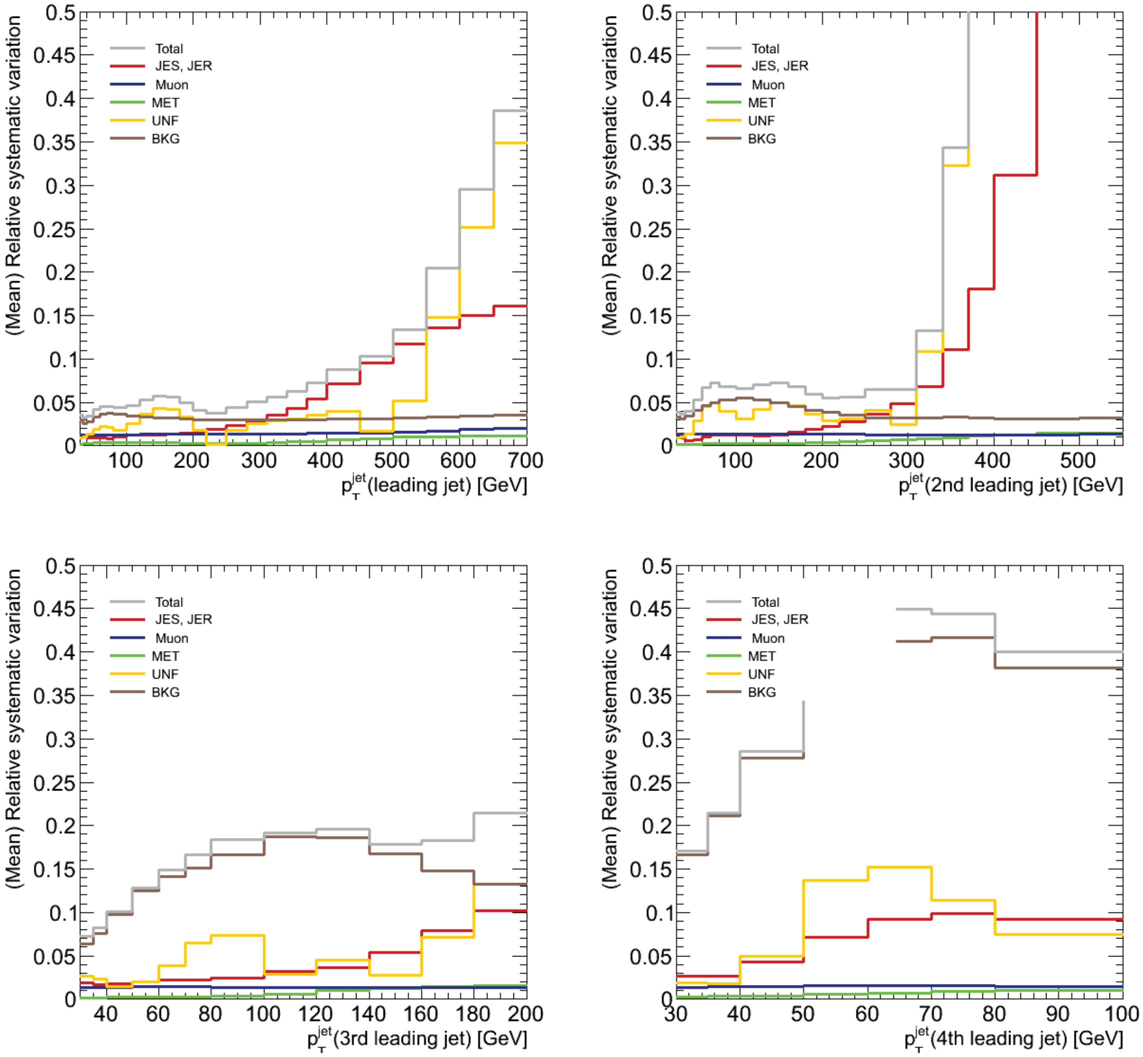

Figure 3.15. Systematic uncertainty contributions to R_{jet} for jet p_{T} of the 1st (top left), 2nd (top right), 3rd (bottom left) and 4th (bottom right) leading jets. Calculation of systematic uncertainties is discussed in detail in the text.

Figure 3.16 shows the systematic uncertainties for the following dijet variables: the dijet invariant mass, ΔR_{jj} and $\Delta\phi_{jj}$. The jet mass has a similar error structure to jet p_{T}, with jet and unfolding uncertainties dominant at high mass. For ΔR_{jj}, the unfolding uncertainty blows up both at very high and very low values. The jet uncer-

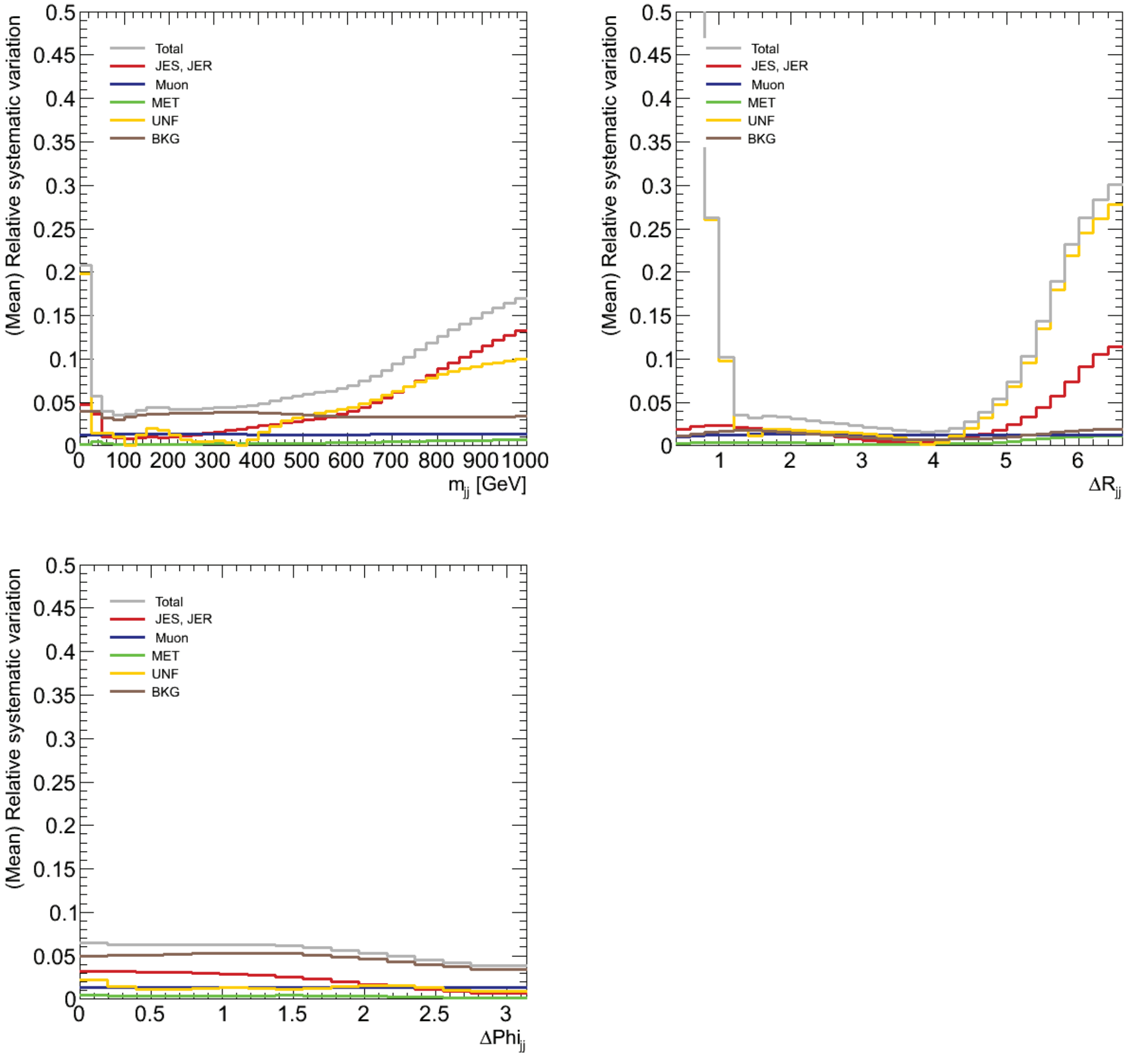

Figure 3.16. Systematic uncertainty contributions to R_{jet} as a function of dijet variables: dijet mass (top left), ΔR_{jj} (top right), and $\Delta\phi_{jj}$ (bottom left). Calculation of systematic uncertainties is discussed in detail in the text.

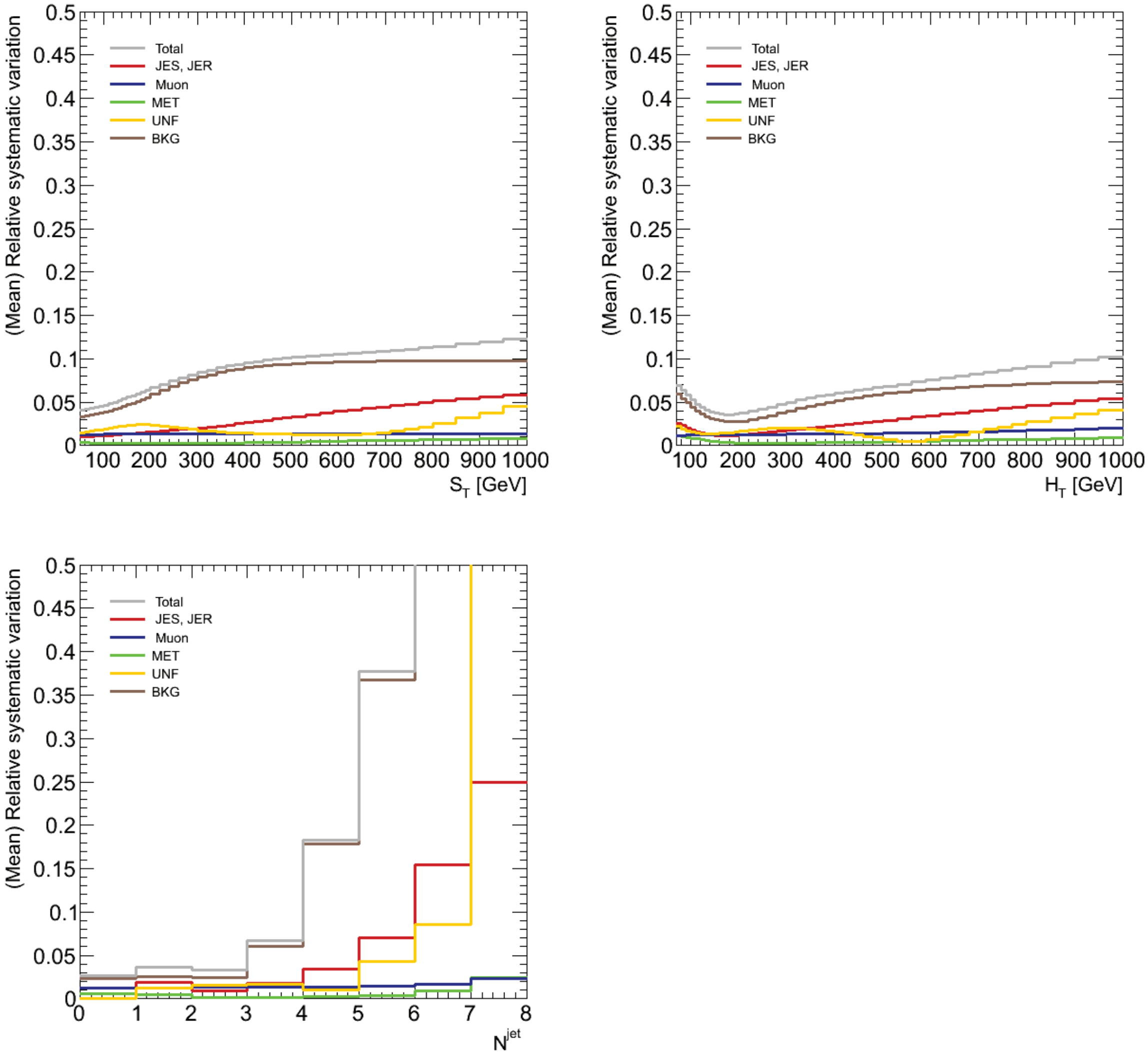

Figure 3.17. Systematic uncertainty contributions to $R_{\rm jet}$ as a function of S_T (top left), H_T (top right), and jet multiplicity (bottom left). Calculation of systematic uncertainties is discussed in detail in the text.

tainties increase with increasing ΔR_{jj}, because large values correlate with at least one jet with a high rapidity. Uncertainties are small and relatively flat for $\Delta\phi_{jj}$. Figure 3.17 shows the uncertainties for S_T, H_T, and jet multiplicity. A similar pattern of uncertainties is seen with S_T and H_T as with other p_{T} related variables. As mentioned previously, for large jet multiplicity, the background estimation is the dominant systematic uncertainty, only here it is seen more clearly. Due to this uncertainty, while for 0-3 jets R_{jet} gives us a very precise measurement, for higher multiplicities it doesn't give us much better precision than W or Z alone. For this reason, an area of future research will be working to reduce this top background related uncertainty. Possible ways of reducing this error include using data driven estimation methods, and taking advantage of the partial correlation in theoretical cross section uncertainties between top, the signal, and W/Z related backgrounds.

3.14 Results and Interpretation

The W and Z cross sections, and R_{jet} spectra are presented here corrected for detector effects and unfolded to dressed particle level, as described in Section 3.12. These results are compared with calculations from BlackHat+Sherpa, corrected as described in Section 3.11, as well as with generator level results from Alpgen and Sherpa. Each set of plots is presented with the measurement shown on top, and with the ratios of data/theory for each generator shown below.

Figure 3.18 shows the unfolded measurement for the exclusive jet multiplicity. Results for BlackHat+Sherpa are only calculated for 0-4 jets, due to theoretical limitations of the program. The theoretical predictions for Alpgen and Sherpa agree with the data within uncertainties for up to five jets. After this, there are substantial disagreements. This is expected as Alpgen only models up to five additional partons, and uses showering algorithms for additional jets. The mild disagreement in the five jet bin may be indicative of some mis-modeling in the generators. For W

and Z cross sections, BlackHat+Sherpa does a good job at describing the data within uncertainties, with the mild exception of the 1 jet bin for the W cross section. However, in the ratio, the systematic uncertainties are much reduced, and the 12% overestimate in this bin is a significant deviation. This is likely due to some difficulty by BlackHat+Sherpa at modeling perturbative QCD, as Alpgen and Sherpa do not show this issue.

As mentioned previously the Tevatron has only measured W/Z inclusively. The previous ATLAS measurement of R_{jet} was a 2010 measurement of R_{jet} as a function of jet p_{T} for events with exactly one jet, and analyzed 33 $\mathrm{pb}^{-1}$of integrated luminosity [7]. It found no significant discrepancy between the measurement and theoretical models, but the statistic uncertainty was larger. Similar comments can be made about the analogous CMS result, which presented R_{jet} as a function of jet multiplicity, using an integrated luminosity of 36 $\mathrm{pb}^{-1}$of data gathered in 2010 [47]. This paper also found that theory matched data in the 1 jet bin (and everywhere else), but the statistical errors were of order 10%, and a different generator was use for the theoretical comparison.

Figures 3.19, 3.20, 3.21, and 3.22 show the unfolded measurements as a function of the p_{T} of the 1st, 2nd, 3rd, and 4th leading jet. For the first leading jet, Alpgen and Sherpa have a trend of overestimating the W cross sections at high jet p_{T}. Within uncertainties, BlackHat+Sherpa does a better job of reproducing the W cross section at high p_{T}. For the Z, Alpgen and Sherpa are better at reproducing the data spectrum, and Sherpa underestimates it for high p_{T}. These deviations are not significant for the cross sections, but all generators show a significant overestimate of R_{jet}, especially at low p_{T}. The R_{jet} distribution shows disagreement between BlackHat+Sherpa and data at the level of 10-15%, outside the level of the systematic uncertainty, consistent with what is seen in the 1 jet bin of the jet multiplicity distribution. Because this occurs at low jet p_{T} as well as at high p_{T} it is unlikely that

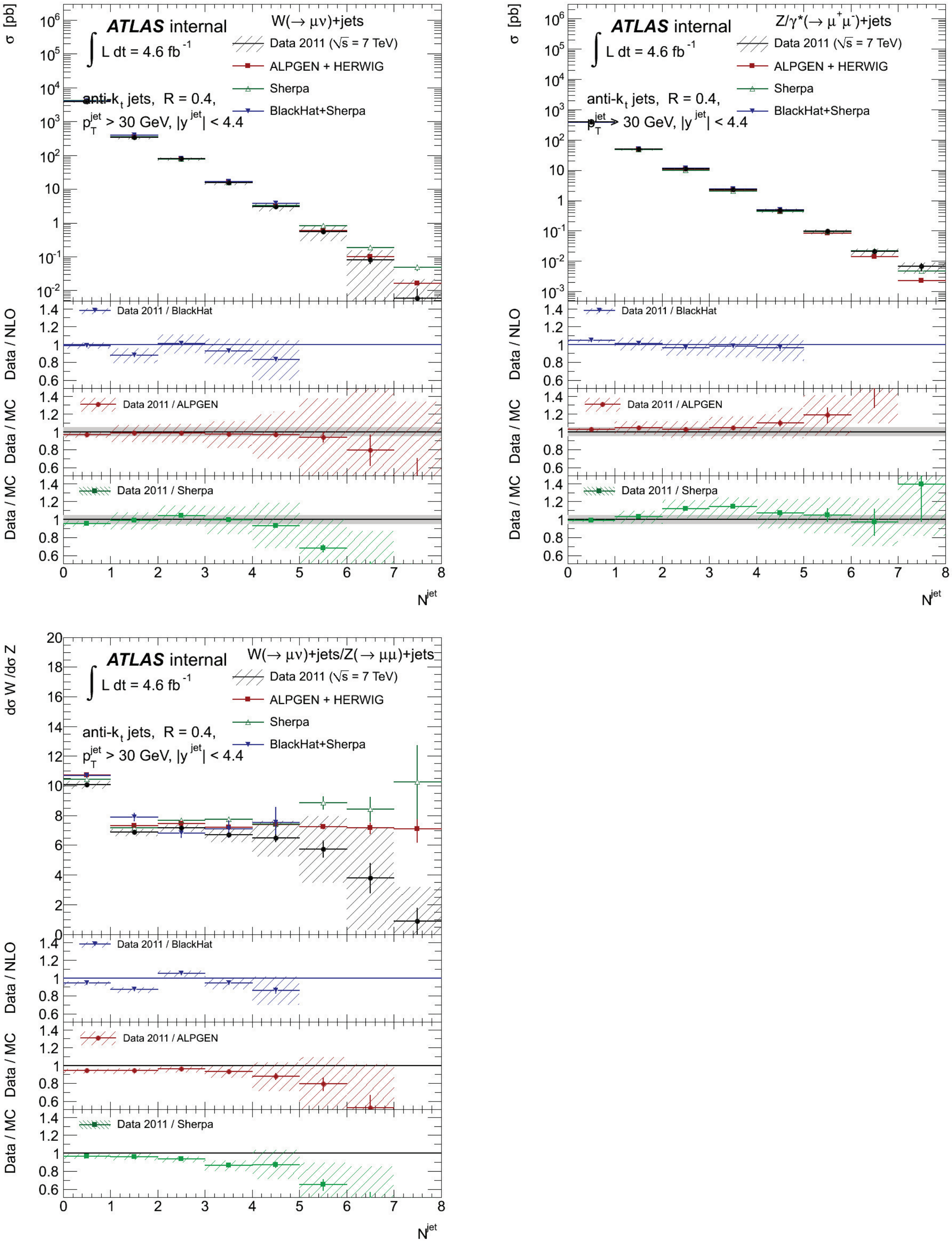

Figure 3.18. Exclusive jet multiplicity for $W \to \mu\nu$ (top left), for $Z \to \mu\mu$ (top right), and for R_{jet} (bottom). Values are presented for data unfolded to the particle level, BlackHat+Sherpa corrected to the particle level and predictions for from Alpgen and Sherpa. The figures show the cross sections and the ratios data/BlackHat, data/Alpgen, and data/Sherpa.

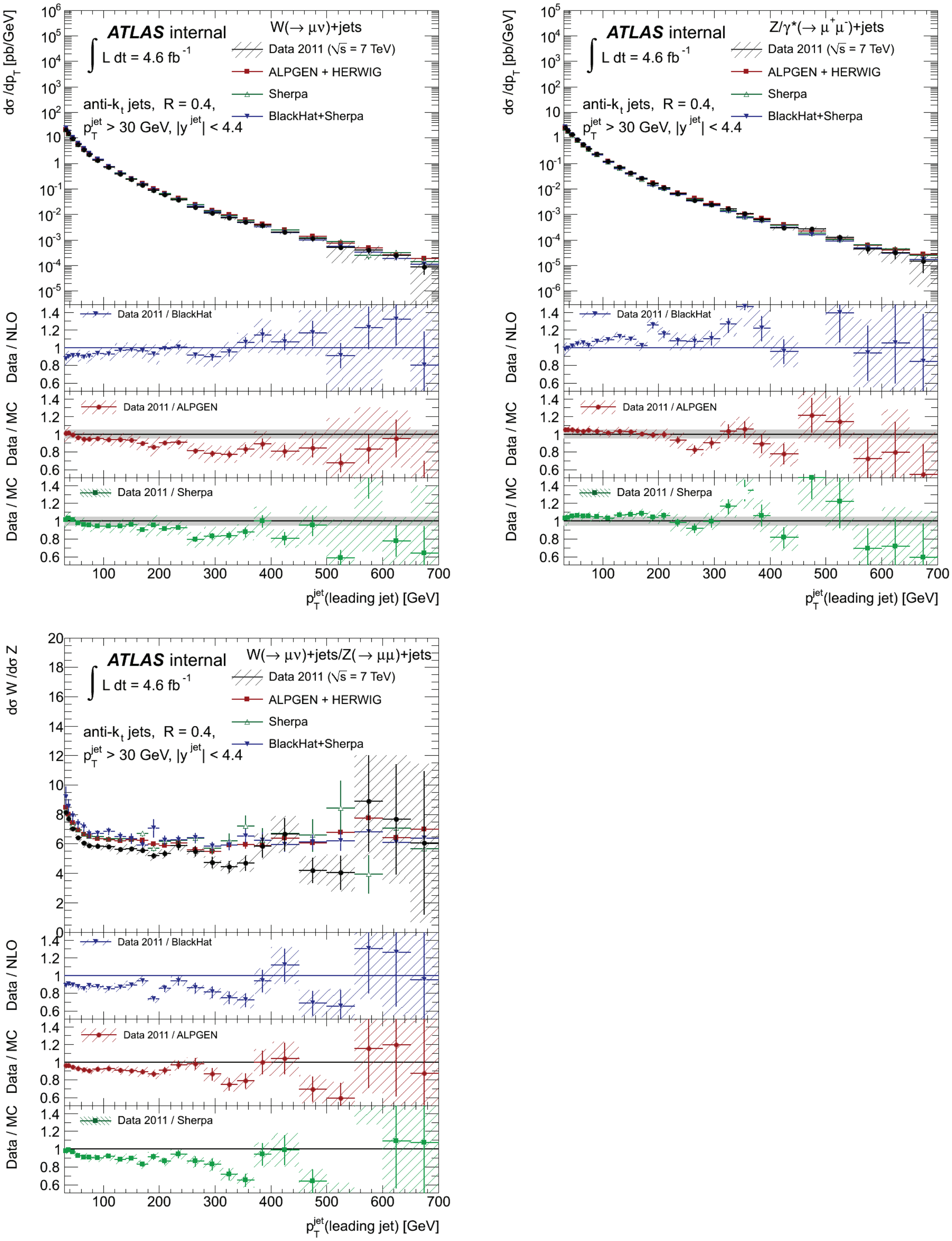

Figure 3.19. Leading jet p_{T} for $W \to \mu\nu$ (top left), for $Z \to \mu\mu$ (top right), and for R_{jet} (bottom). Values are presented for data unfolded to the particle level, BlackHat+Sherpa corrected to the particle level and predictions for from Alpgen and Sherpa. The figures show the cross sections and the ratios data/BlackHat, data/Alpgen, and data/Sherpa.

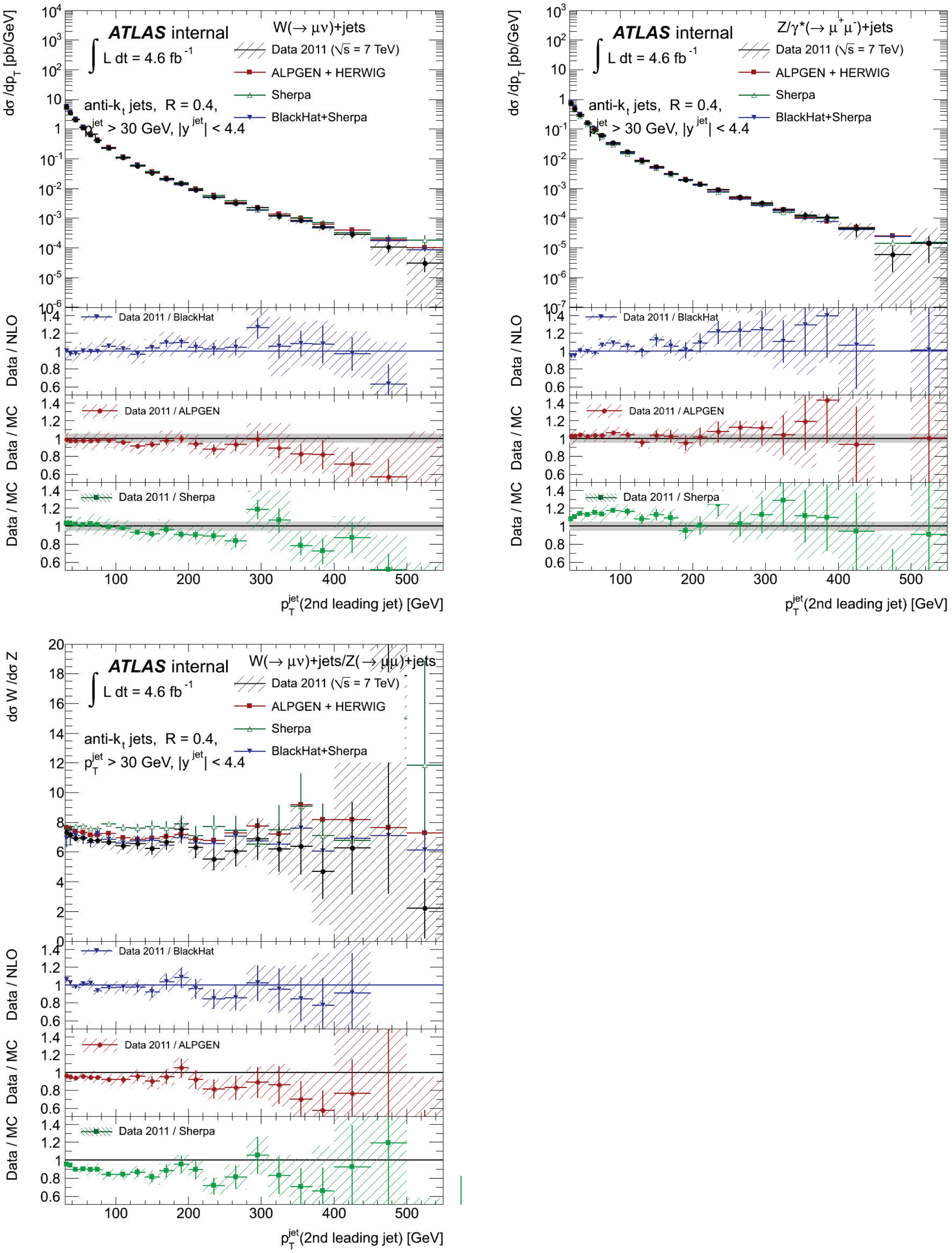

Figure 3.20. Second leading jet p_T for $W \to \mu\nu$ (top left), for $Z \to \mu\mu$ (top right), and for R_{jet} (bottom). Values are presented for data unfolded to the particle level, BlackHat+Sherpa corrected to the particle level and predictions for from Alpgen and Sherpa. The figures show the cross sections and the ratios data/BlackHat, data/Alpgen, and data/Sherpa.

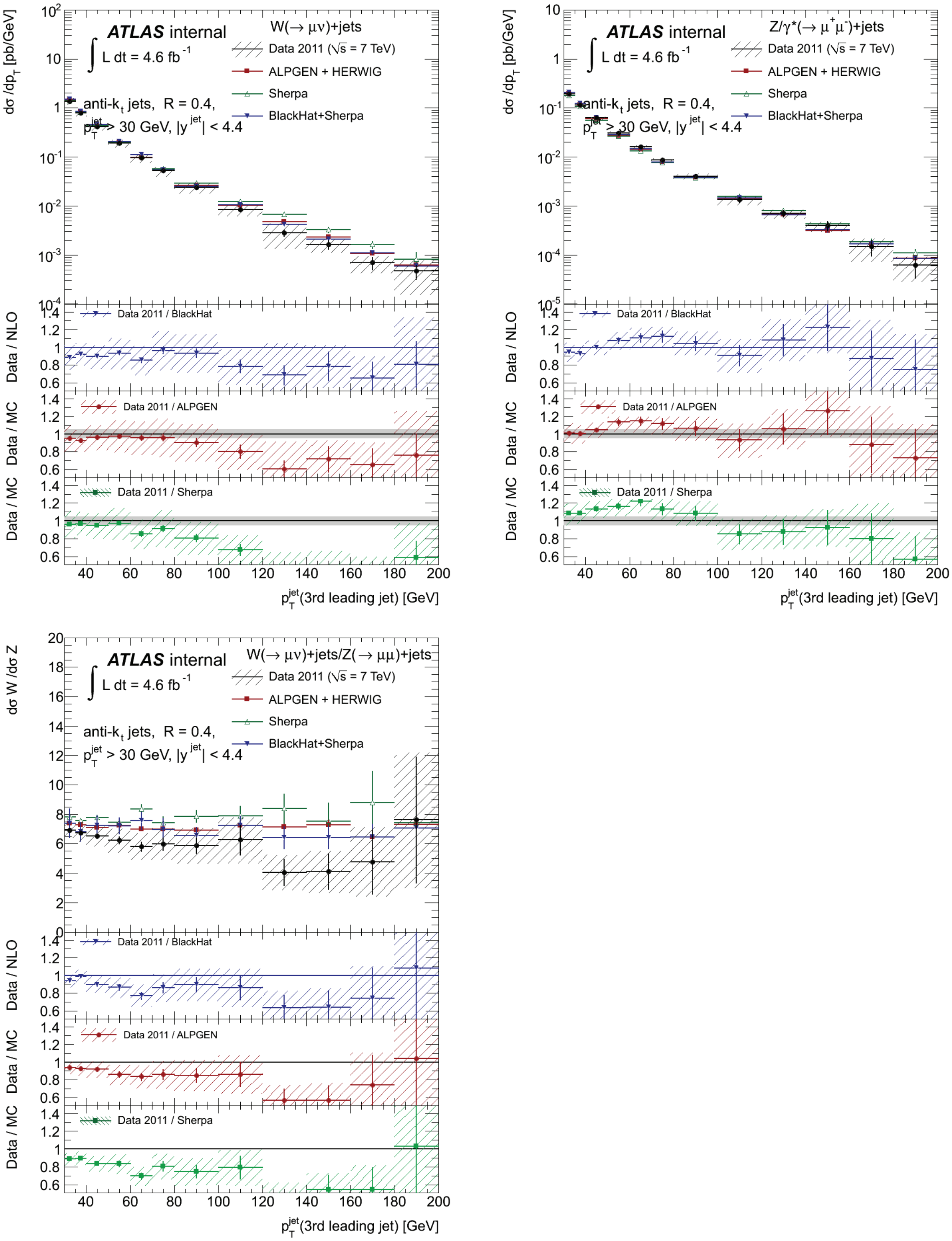

Figure 3.21. Third leading jet p_T for $W \to \mu\nu$ (top left), for $Z \to \mu\mu$ (top right), and for R_jet (bottom). Values are presented for data unfolded to the particle level, BlackHat+Sherpa corrected to the particle level and predictions for from Alpgen and Sherpa. The figures show the cross sections and the ratios data/BlackHat, data/Alpgen, and data/Sherpa.

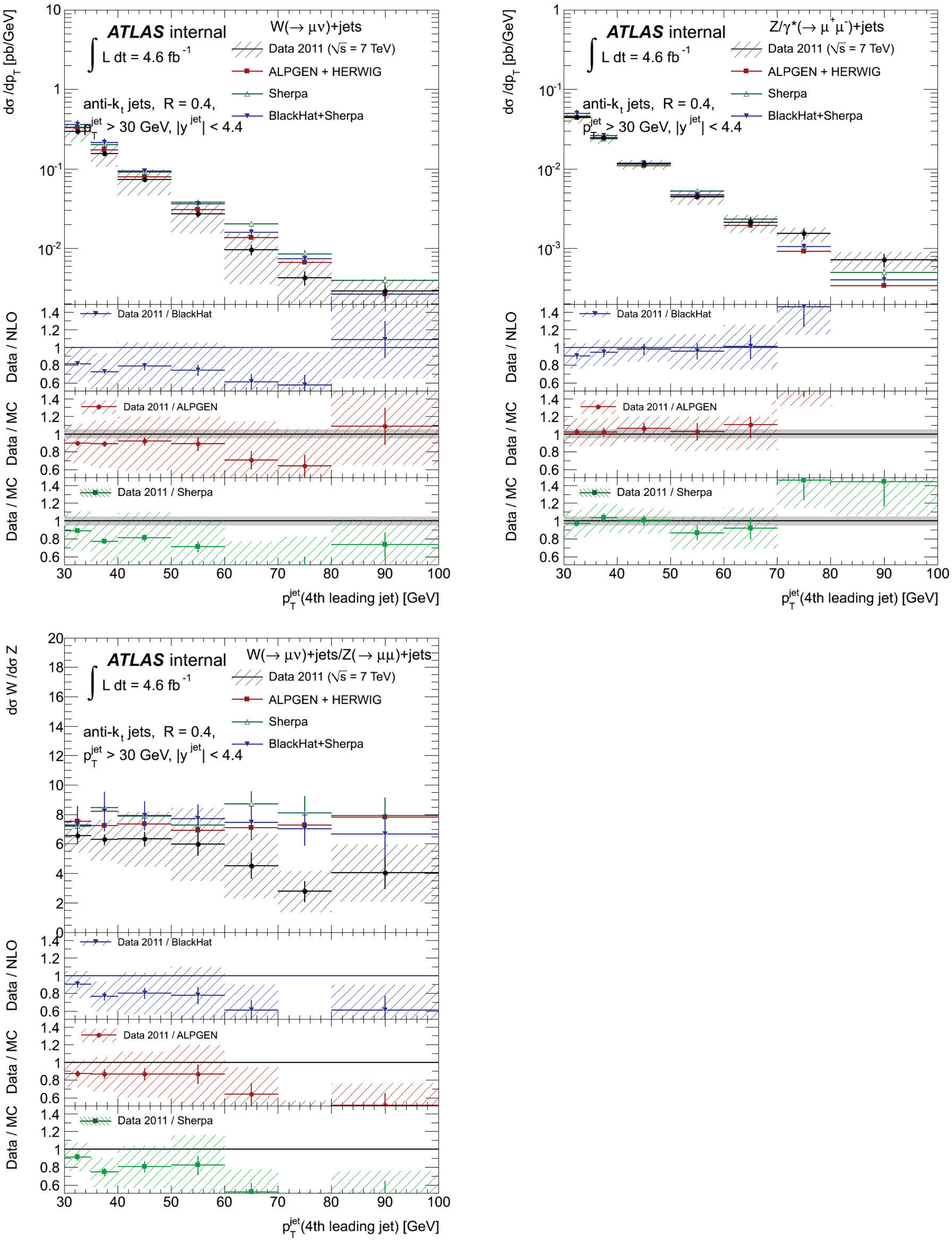

Figure 3.22. Fourth leading jet p_{T} for $W \to \mu\nu$ (top left), for $Z \to \mu\mu$ (top right), and for R_{jet} (bottom). Values are presented for data unfolded to the particle level, BlackHat+Sherpa corrected to the particle level and predictions for from Alpgen and Sherpa. The figures show the cross sections and the ratios data/BlackHat, data/Alpgen, and data/Sherpa.

this is an indication of new physics, rather it is likely that this is an indication of BlackHat+Sherpa not modeling the ratio between W and Z bosons correctly for this distribution. This distribution and the jet multiplicity distribution illustrate the power of the R_{jet} method, as this discrepancy is not significant in the individual W or Z channels.

For 2nd jet p_{T}, Alpgen and Sherpa describe the cross sections well, but show a slight overestimate of R_{jet}. The 2nd jet distributions are all described well by BlackHat+Sherpa. All generators slightly overestimate the W cross section for 3rd jet p_{T} around 160 GeV, but this deviation is only significant for Sherpa. The Z cross section is well modeled by all the generators for 3rd jet p_{T}. The picture for 4th jet p_{T} is similar, with W cross sections seeming to be overestimated, but in this case the uncertainties are very large, even on the ratio, due to the $t\bar{t}$ uncertainty.

Figures 3.23, 3.24, 3.25, and 3.26 show the unfolded measurements as a function of the rapidity of the 1st, 2nd, 3rd, and 4th leading jet. For the leading jet, the W and Z cross sections predicted by the generators agree reasonably well except for at high rapidity, where Sherpa and BlackHat+Sherpa overestimate the cross section. For the ratio, the shape of each distribution is more reasonable, but as seen in other distributions, R_{jet} for one selected jet is lower in the data than predicted by the generators, particularly when compared to BlackHat+Sherpa.

For the second and third jet rapidity distributions, the situation is very similar, only with BlackHat+Sherpa doing a much better job modeling the central value of R_{jet}. For the fourth jet rapidity, the statistics are worse, so it becomes more difficult to make a definitive statement, within errors the generators agree with the data for the cross sections. For R_{jet}, there is a slight excess for all generators, but it is still within uncertainties for Alpgen and BlackHat+Sherpa, with Sherpa showing a modest disagreement.

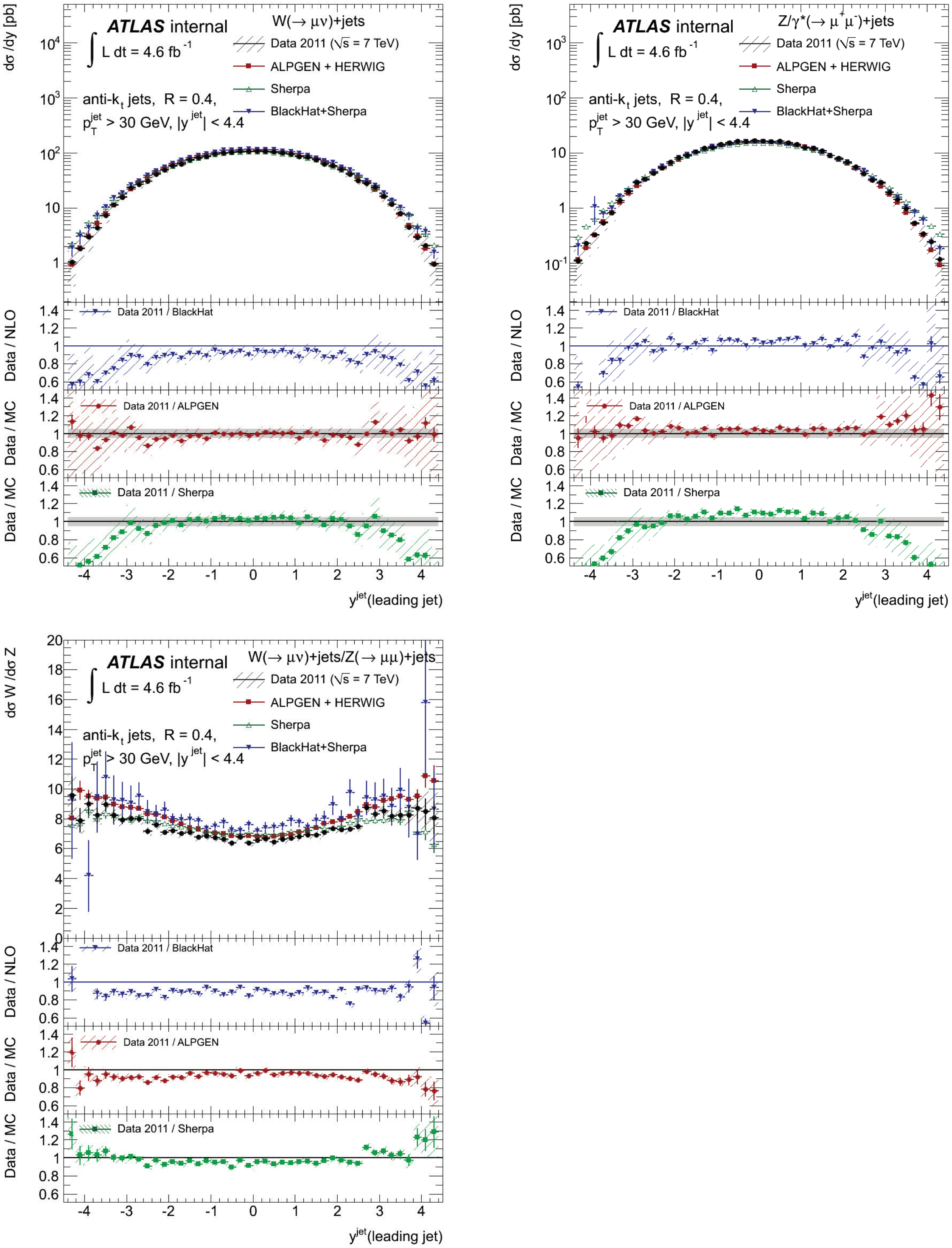

Figure 3.23. Leading jet rapidity for $W \to \mu\nu$ (top left), for $Z \to \mu\mu$ (top right), and for $R_{\rm jet}$ (bottom). Values are presented for data unfolded to the particle level, BlackHat+Sherpa corrected to the particle level and predictions for from Alpgen and Sherpa. The figures show the cross sections and the ratios data/BlackHat, data/Alpgen, and data/Sherpa.

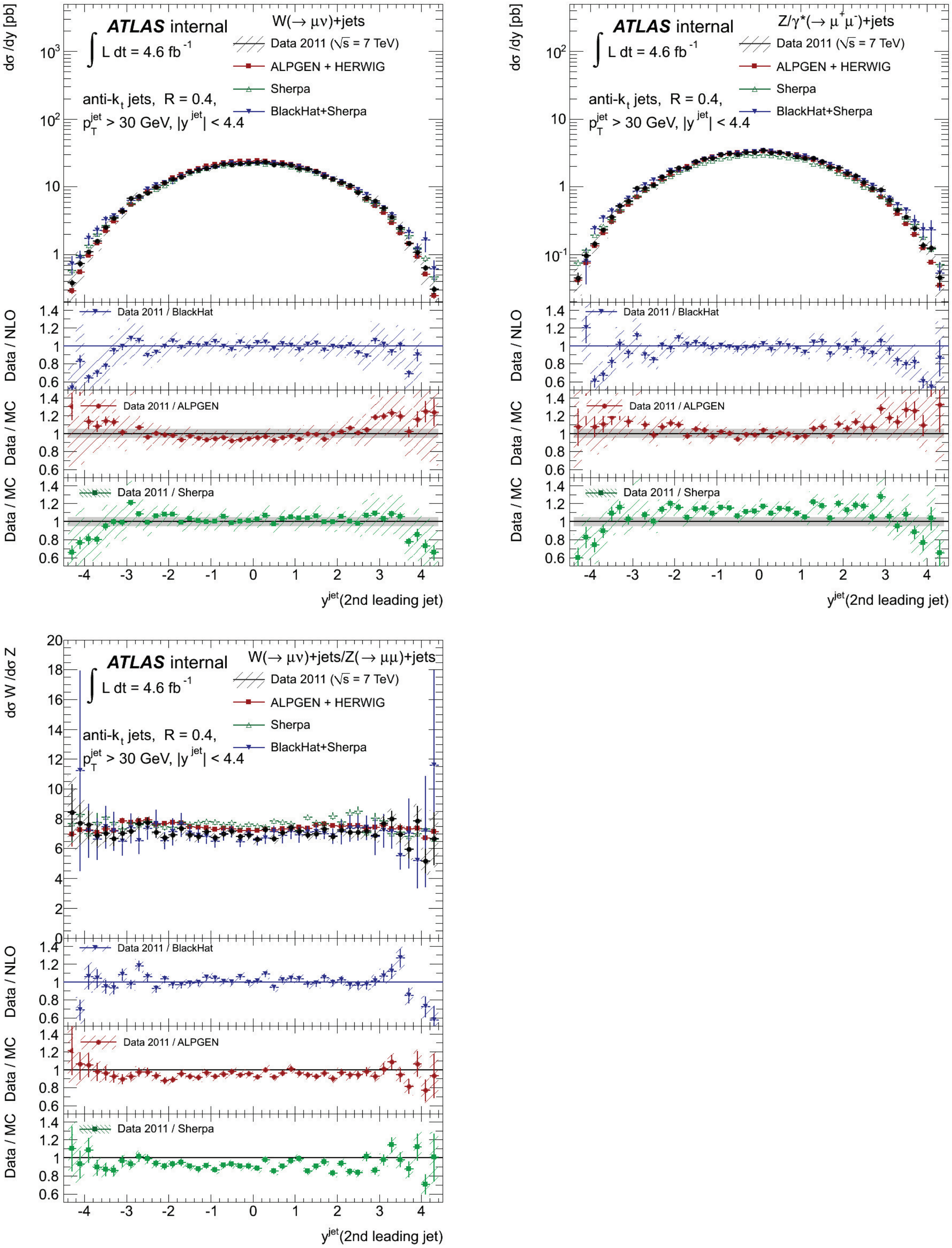

Figure 3.24. Second leading jet rapidity for $W \rightarrow \mu\nu$ (top left), for $Z \rightarrow \mu\mu$ (top right), and for R_{jet} (bottom). Values are presented for data unfolded to the particle level, BlackHat+Sherpa corrected to the particle level and predictions for from Alpgen and Sherpa. The figures show the cross sections and the ratios data/BlackHat, data/Alpgen, and data/Sherpa.

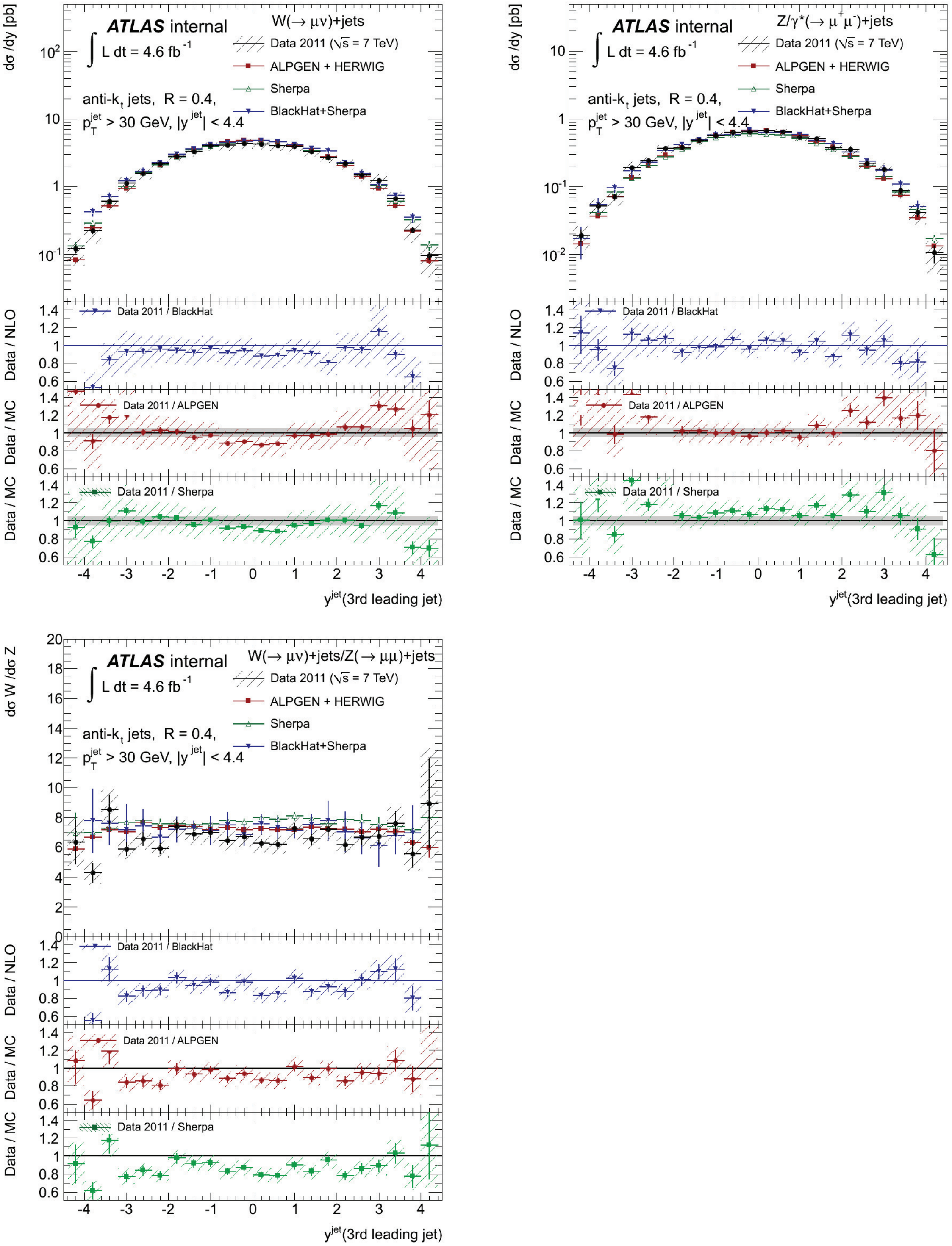

Figure 3.25. Third leading jet rapidity for $W \rightarrow \mu\nu$ (top left), for $Z \rightarrow \mu\mu$ (top right), and for R_{jet} (bottom). Values are presented for data unfolded to the particle level, BlackHat+Sherpa corrected to the particle level and predictions for from Alpgen and Sherpa. The figures show the cross sections and the ratios data/BlackHat, data/Alpgen, and data/Sherpa.

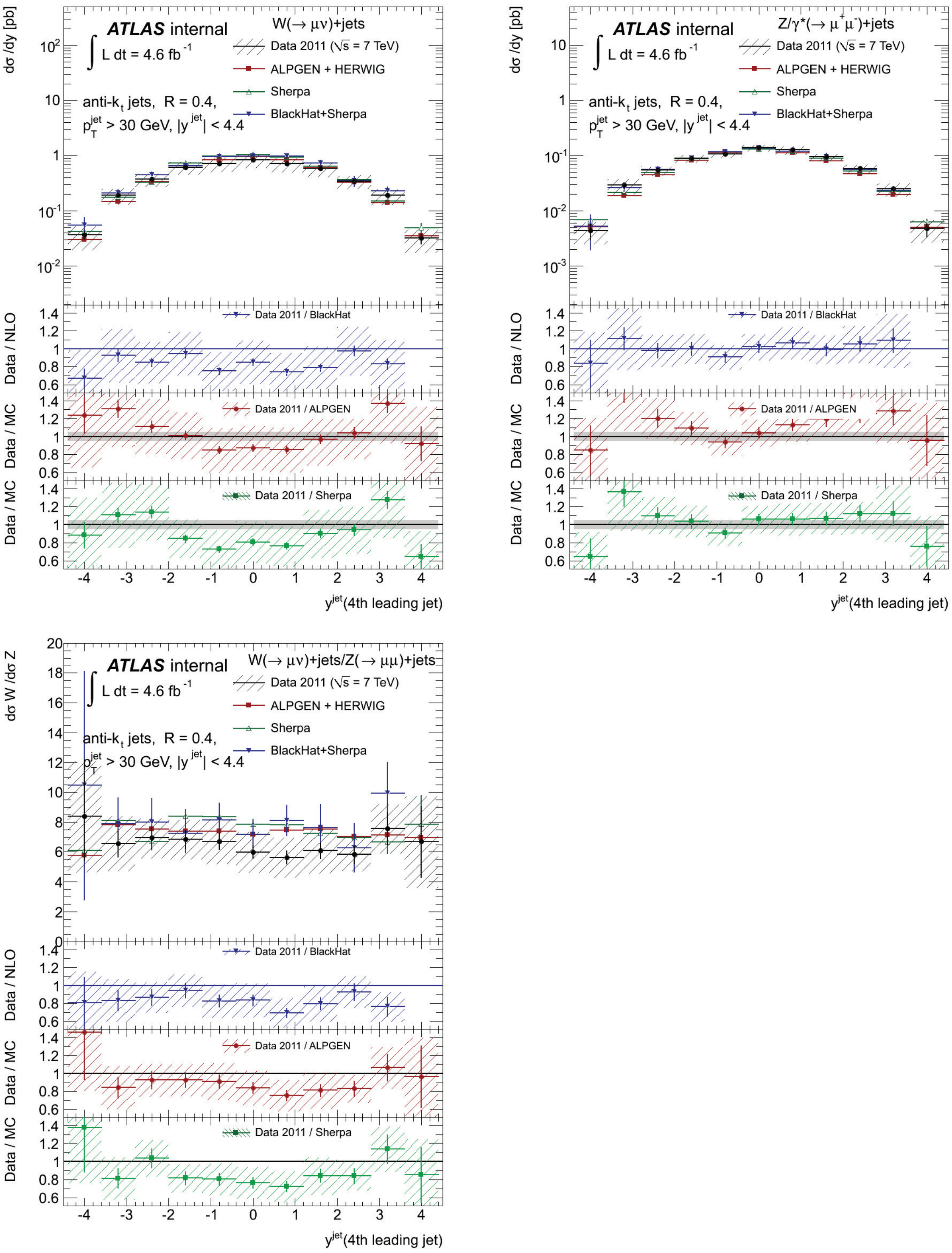

Figure 3.26. Fourth leading jet rapidity for $W \rightarrow \mu\nu$ (top left), for $Z \rightarrow \mu\mu$ (top right), and for R_{jet} (bottom). Values are presented for data unfolded to the particle level, BlackHat+Sherpa corrected to the particle level and predictions for from Alpgen and Sherpa. The figures show the cross sections and the ratios data/BlackHat, data/Alpgen, and data/Sherpa.

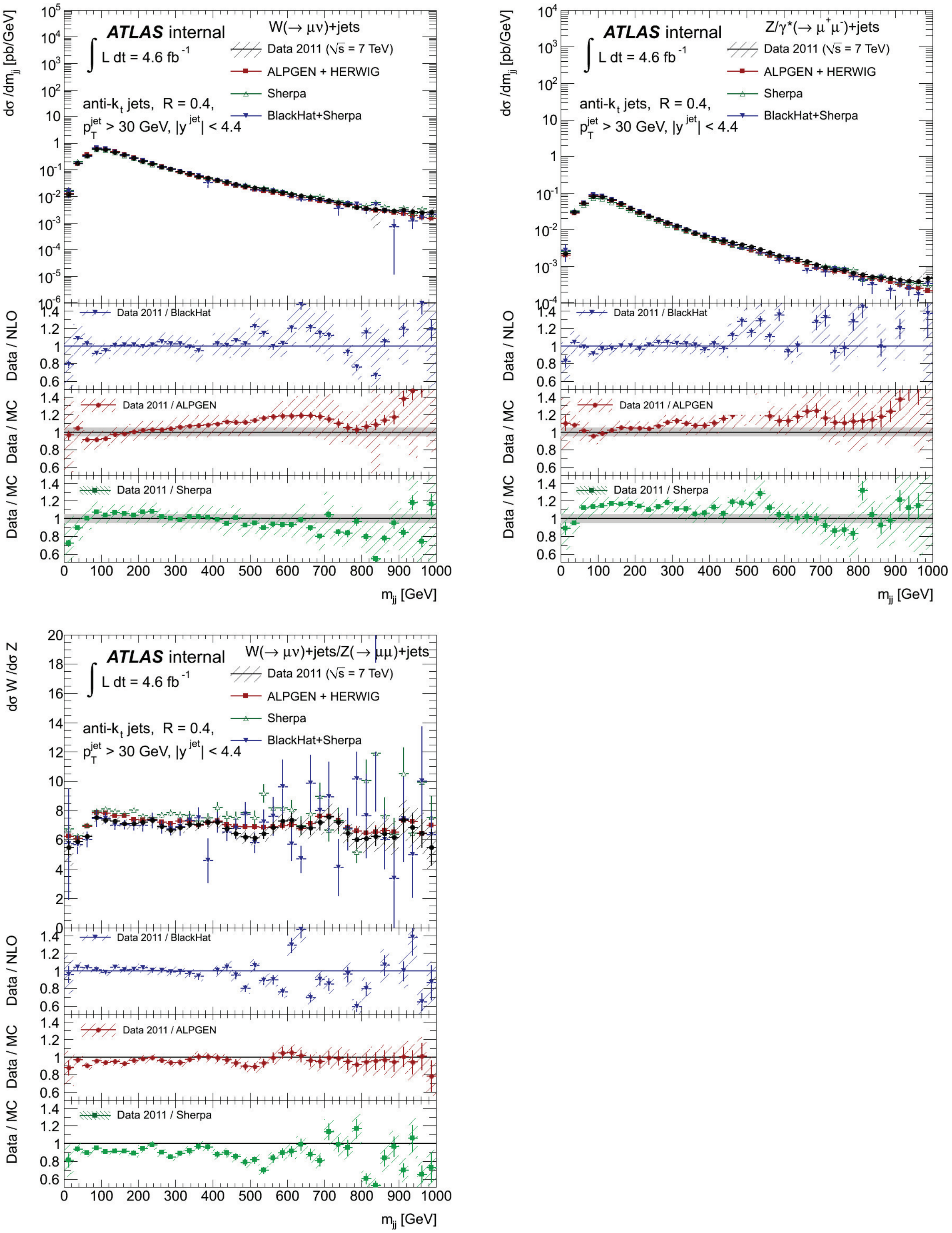

Figure 3.27. Dijet invariant mass for $W \to \mu\nu$ (top left), for $Z \to \mu\mu$ (top right), and for R_{jet} (bottom). Values are presented for data unfolded to the particle level, BlackHat+Sherpa corrected to the particle level and predictions for from Alpgen and Sherpa. The figures show the cross sections and the ratios data/BlackHat, data/Alpgen, and data/Sherpa.

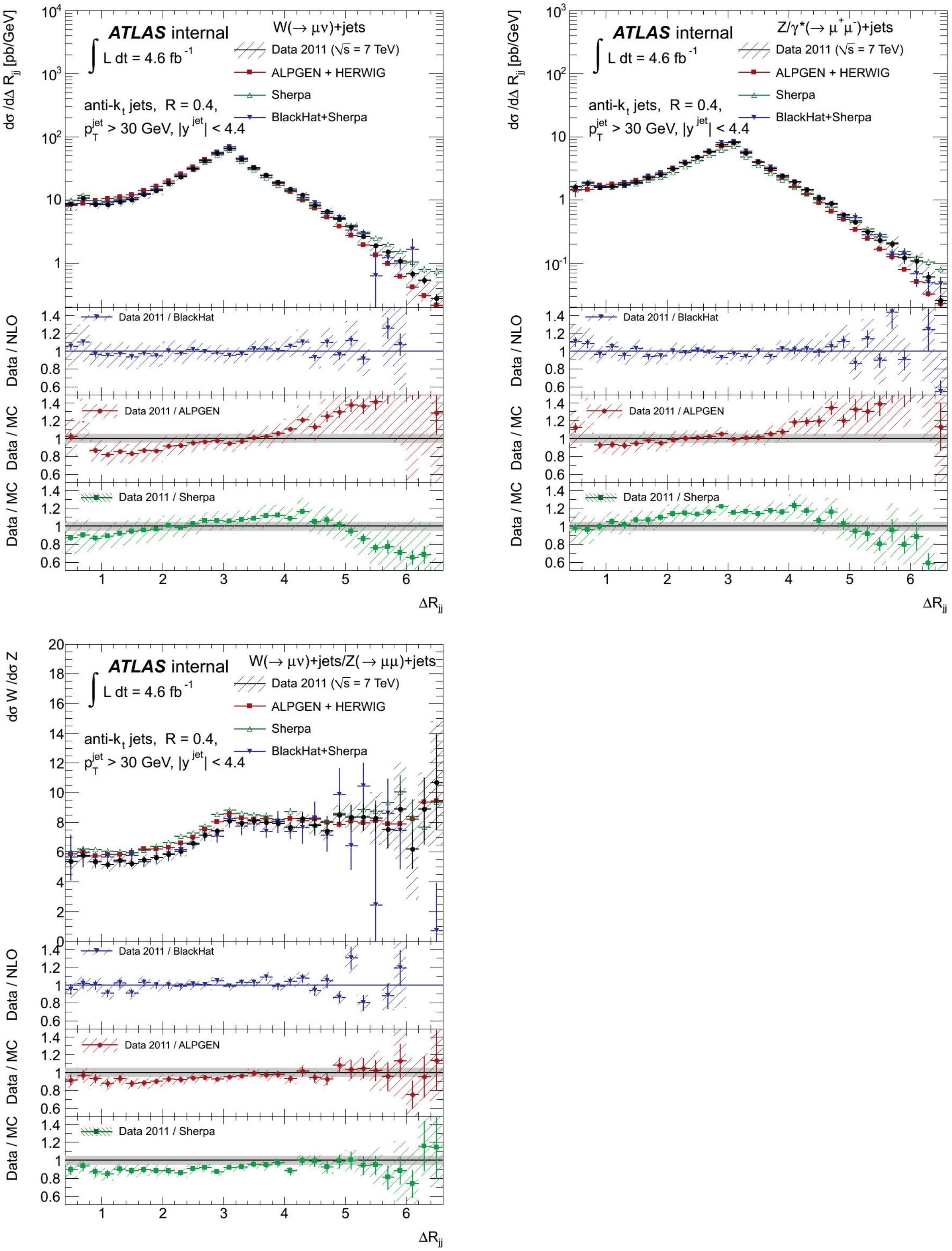

Figure 3.28. Dijet ΔR_{jj} for $W \to \mu\nu$ (top left), for $Z \to \mu\mu$ (top right), and for R_{jet} (bottom). Values are presented for data unfolded to the particle level, BlackHat+Sherpa corrected to the particle level and predictions for from Alpgen and Sherpa. The figures show the cross sections and the ratios data/BlackHat, data/Alpgen, and data/Sherpa.

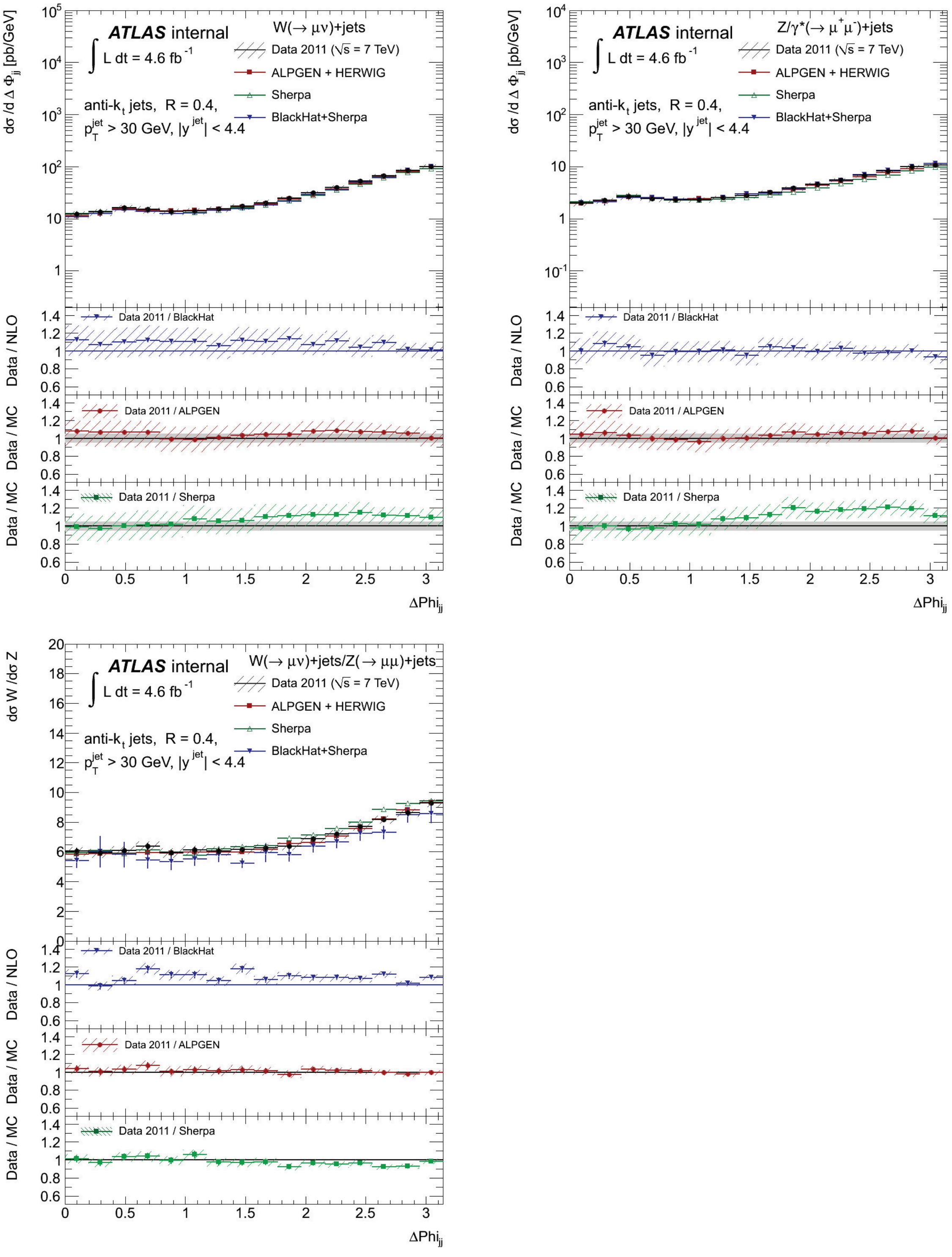

Figure 3.29. Dijet $\Delta\phi_{jj}$ for $W \to \mu\nu$ (top left), for $Z \to \mu\mu$ (top right), and for R_{jet} (bottom). Values are presented for data unfolded to the particle level, BlackHat+Sherpa corrected to the particle level and predictions for from Alpgen and Sherpa. The figures show the cross sections and the ratios data/BlackHat, data/Alpgen, and data/Sherpa.

Figures 3.27, 3.28, and 3.29 show the unfolded cross sections as a function of the following dijet variables: invariant mass, ΔR_{jj}, and $\Delta\phi_{jj}$. The dijet invariant mass has good agreement between the generators and the data for both the cross sections and for R_{jet}, though SHERPA slightly overestimates the value of R_{jet}. There is also a slight underestimate of ALPGEN of the W and Z cross sections, but this deviation is within uncertainties, and disappears in the ratio. Measurements of the ΔR_{jj} show similar excellent agreement, especially for BLACKHAT+SHERPA. For the W and Z, the cross section predictions are low for ALPGEN and high for SHERPA at very high ΔR_{jj}. As these trends are present in both W and Z cross sections, it does not appear in the ratio. The $\Delta\phi_{jj}$ distribution is well modeled by all the generators, though there is a small over-estimation of R_{jet} by BLACKHAT+SHERPA.

Figures 3.30 and 3.31 show the unfolded cross sections as a function of the S_T and H_T in the event. As defined at the beginning of the section, S_T is the scalar sum of the p_{T} of selected jets, and H_T is the same quantity with the p_{T} of selected muons and $E_{\text{T}}^{\text{miss}}$ (for the W channel) added as well. At high values, these variables have contributions from both a small number of high p_{T} jets, and from a larger number of lower p_{T} jets. Due to this, this is a very rigorous test of a generator over a variety of scales. There is good agreement between ALPGEN, SHERPA, and the data for lower S_T and H_T values. At higher momentums, ALPGEN and SHERPA overestimate the W cross section. This leads to a deviation in R_{jet}. This deviation is not large, but appears to be statistically significant around 300-400 GeV. This is likely due to the same cause as the deviation in the 1 jet p_{T}, but this warrants further investigation.

There is very poor agreement between BLACKHAT+SHERPA and the data for S_T and H_T at high momentum values. This indicates the weakness of strict fixed order calculations: for the multiplicity of 1 or more jets, it calculates exactly one jet at NLO, and then one additional jet at LO. This approach, as shown, fails to model the high S_T/H_T region, where high jet multiplicity becomes very important. This contrasts

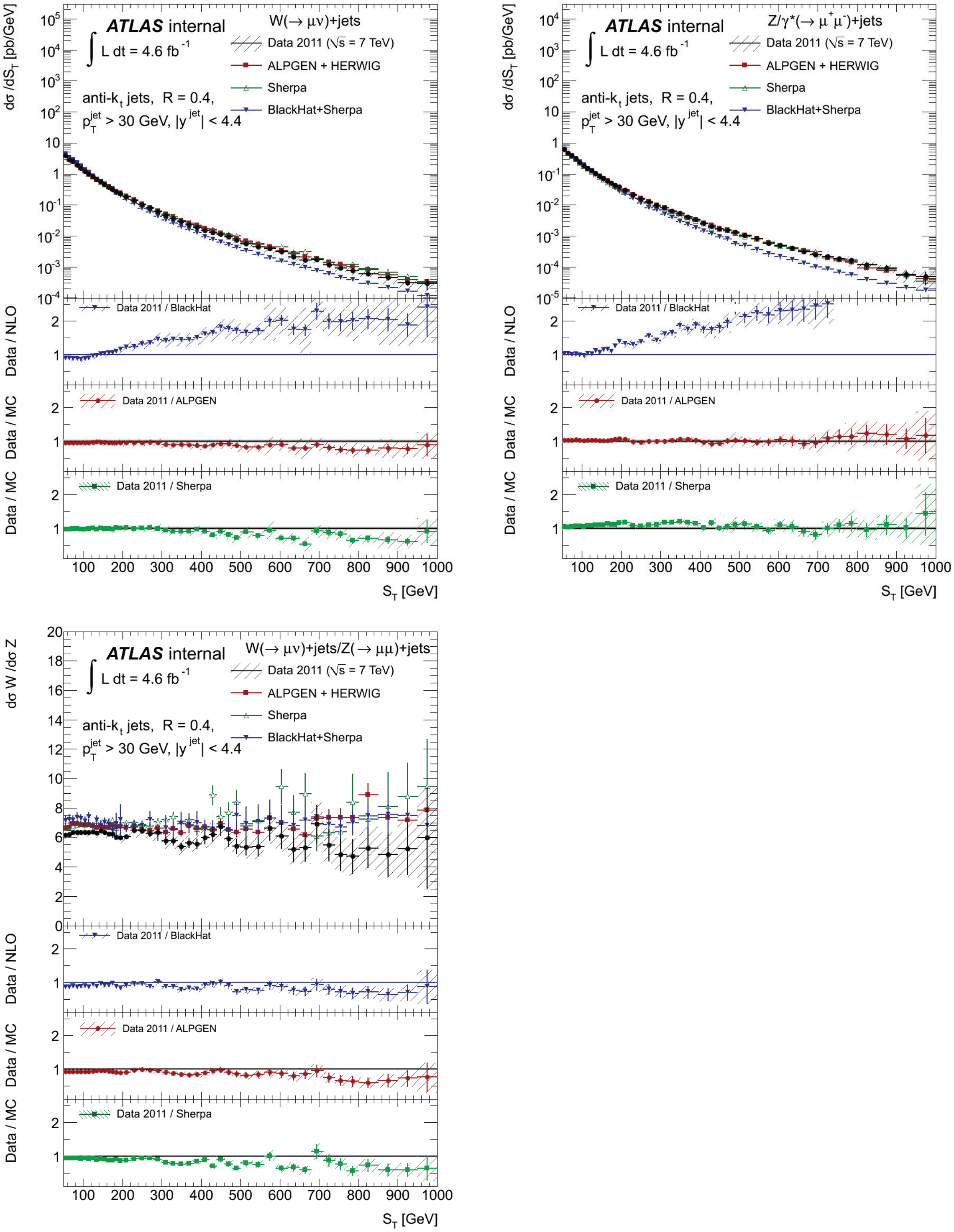

Figure 3.30. Scalar sum p_{T} of selected jets, S_T, for $W \to \mu\nu$ (top left), for $Z \to \mu\mu$ (top right), and for R_{jet} (bottom). Values are presented for data unfolded to the particle level, BlackHat+Sherpa corrected to the particle level and predictions for from Alpgen and Sherpa. The figures show the cross sections and the ratios data/BlackHat, data/Alpgen, and data/Sherpa.

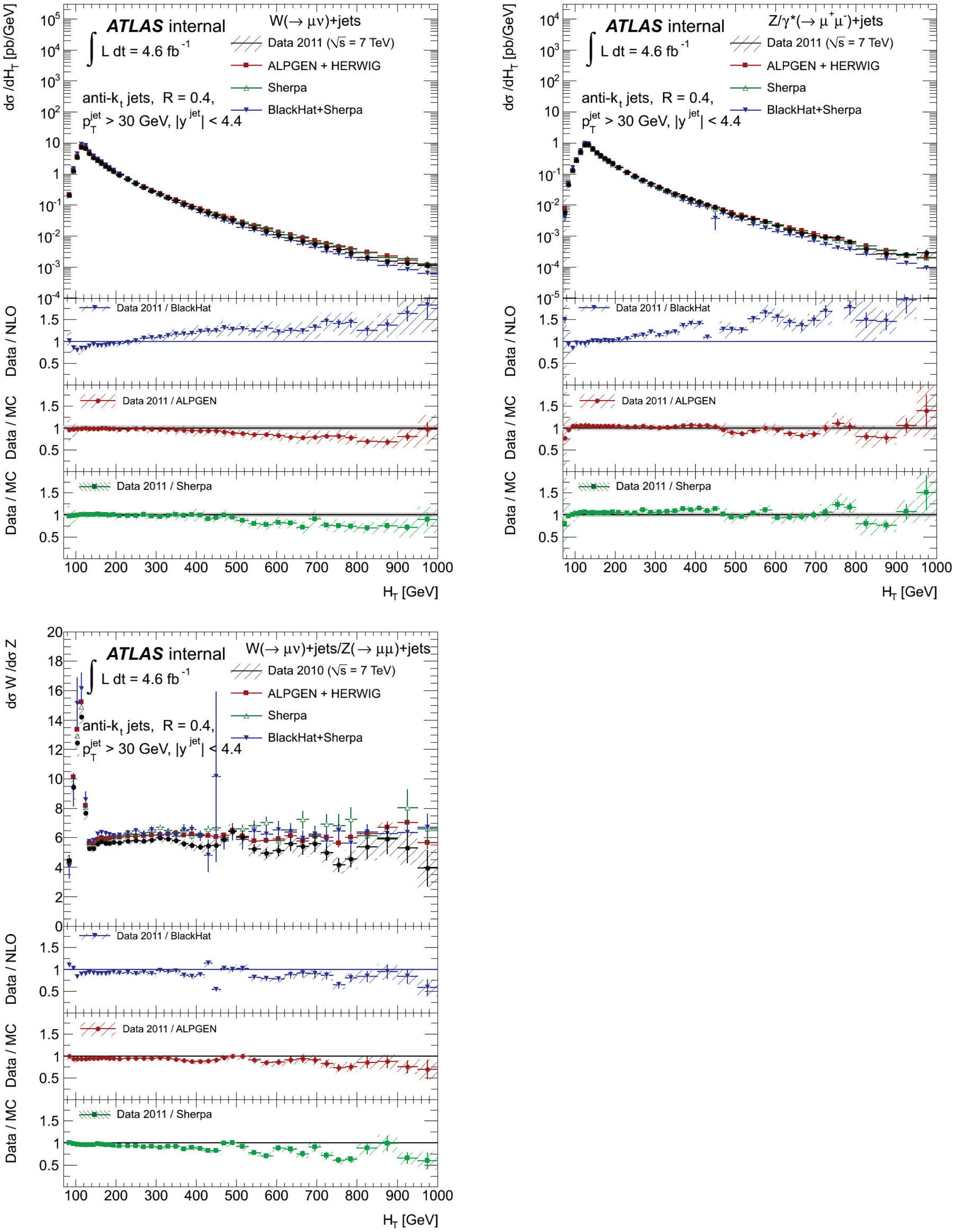

Figure 3.31. Scalar sum p_{T} of selected high p_{T} objects, H_T, for $W \rightarrow \mu\nu$ (top left), for $Z \rightarrow \mu\mu$ (top right), and for R_{jet} (bottom). Values are presented for data unfolded to the particle level, BlackHat+Sherpa corrected to the particle level and predictions for from Alpgen and Sherpa. The figures show the cross sections and the ratios data/BlackHat, data/Alpgen, and data/Sherpa.

with Alpgen and Sherpa, which both model these variables well, likely due to their showering description and the well developed matching/overlap-removal procedure between showering and matrix element calculations. Even this poor description of cross sections, BlackHat+Sherpa does a reasonable job describing R_{jet}, as these effects largely cancel in the ratio.

CHAPTER 4

CONCLUSIONS

Since 7 TeV collisions began in 2010, the LHC has been at the forefront of the high energy physics frontier. The prime motivation of the detector, the understanding of electroweak symmetry breaking, has been bolstered by the discovery of a particle consistent with the Higgs Boson. However, understanding the electroweak sector remains critical, both for studies looking to characterize the Higgs Boson, and for searches for other new phenomena. Specifically, understanding of W and Z boson production is critical, as they are an important background to other searches, often in concert with hadronic activity. Examining the ratio of W to Z production allows for a very precise and robust measurement, as this allows the cancellation of many experimental and theoretical systematics.

This thesis measures the W cross sections, Z cross section, and their ratio R_{jet} as a function of a variety of kinematic variables. The measurement is compared to results from three generators: ALPGEN, SHERPA, and BLACKHAT+SHERPA. The R_{jet} ratio agrees with the prediction from BLACKHAT+SHERPA over most of the kinematic range. There is a roughly 10% overestimation of R_{jet} in the 1 jet bin at low p_{T}. While this mismatch is interesting and worthy of further study, the low p_{T} nature of this mismatch suggests a generator deficiency. There are also small deviations in the S_T and H_T distributions that are likely related. In addition, for 5 or more jets, there is an overestimate by ALPGEN and SHERPA that increases with increasing jet multiplicity. However, this is somewhat expected as jets produced from more than

5 partons are produced in generators via showering algorithms not expected to have the rigor of matrix level calculations.

The LHC will continue to study electroweak symmetry breaking and other high p_{T} phenomena for years to come. The results of this study of R_{jet} will inform theorists and generator experts, improving both our simulations and our understanding of perturbative QCD. It is hoped that these results will further the long term mission of the LHC, and to contribute to probing some of the most fundamental questions about the universe and its nature.

APPENDIX

MUON RECONSTRUCTION SOFTWARE ROBUSTNESS

During the commissioning of the ATLAS detector, the muon reconstruction software algorithms also went through intense commissioning. Every detector is built with some degree of redundancy, but this redundancy depends not only on the detector elements themselves, but also on the flexibility of the software used to interpret the data. An exhaustive investigation into the robustness of reconstruction algorithms was performed before the beginning of collisions late in 2009 (using Athena release 14). This series of studies examined the effects of chamber failure, misalignment, miscalibration, magnetic-field deviations, and material mis-modeling on the efficiency, resolution and fake rate of muon reconstruction algorithms. This appendix focuses on the effect of the failure of an entire layer of precision chambers, as other aspects were not found to have a large effect for reasonable deviations. For example, the impact of the removal of entire trigger layers on reconstruction efficiency was found to be negligible, and the effect of removing a single CSC gas gap (out of four) was found to be very small.

The purpose of these robustness studies was twofold: to understand how performance parameters would suffer under partial failure of the muon spectrometer, and also to understand and to improve the flexibility of muon reconstruction algorithms. This study is described in detail in an internal ATLAS note [48].

Methodology

This study removed hit level information from the data-record of an event before it was reconstructed. It focused on removal of either a single multi-layer, or both multi-layers of one of the three station layers of precision chambers (Inner, Middle, and Outer stations of MDTs and CSCs). This removal was made for all of the solid angle range. While this is not a realistic failure, it is useful to simulate worst case scenarios, and the failure of a Mezzanine card could produce the failure of a multi-layer over some limited angular range.

The efficiency was studied using signal samples from several different processes with different energy muons and hadronic signatures, but the results of this appendix will focus on results from $Z \rightarrow \mu\mu$ simulation files. Efficiency measures are estimated from the truth record, with truth muons matched to reconstructed muons by hit matching.

While only Staco combined muons are used in the bulk of this thesis, this study considers all major muon reconstruction algorithms, with the exception of calorimeter tagging algorithms, since these do no rely on the muon spectrometer. ATLAS supports two families of muon reconstruction algorithms: Moore and Muonboy. These names typically refer to the reconstruction algorithms that use only muon spectrometer information. Combined reconstruction algorithms allow muon spectrometer (MS) information to be integrated with inner detector (ID) information. Muid and Staco are the combined algorithms for Moore and Muonboy, respectively. These algorithms back-extrapolate a muon spectrometer track to the beam line, match this track to the corresponding ID track, and build the combined track from the MS and ID tracks. Staco uses the error matrices of the ID and MS tracks to combine the tracks, while Muid uses the ID and MS hits to perform a full track refit.

Tagging algorithms follow a different approach, starting from an inner detector track and extrapolating outward into the muon spectrometer, associating one or more muon spectrometer segments with the inner detector track. The tagging algorithms that exist differ somewhat in their approach. MuTag belongs to the Muonboy family, and is designed explicitly to only fill in holes in acceptance. It only uses muon spectrometer segments that are not used by Muonboy itself, and is restricted primarily to the inner chamber-layer of MDTs (the newest version also incorporates middle chamber-layer segments over a limited eta region). MuGirl performs its own pattern recognition in the MS inside a road defined by an extrapolated ID track. It then applies track building and fitting algorithms to the MS and ID hits. MuTagIMO associates an extrapolated ID track with Moore MDT and CSC segments in any of the chamber-layers: inner, middle, and outer.

Early Improvement in Robustness

During an early iteration of this study, the Muonboy algorithm was found to have drastic drops in efficiency under removal of MDT multi-layers. This problem was traced back to an unrealistically tight selection on the number of missed hits in tubes traversed by the reconstructed muon track. This problem was eliminated in later versions of the code, as is shown in Figure A.1

Results for Muon Spectrometer Reconstruction

Efficiency as a Function of Pseudorapidity

Figure A.2 shows both a pseudorapidity distribution for missed muons and the nominal efficiency of muon spectrometer reconstruction (Moore) as a function of pseudorapidity (no chambers removed). Efficiency is defined as the number of matched reconstructed muons over the number of true muons. The drop in efficiency at $\eta = 0$ is due to a gap in detector coverage. The drop around $\eta = 1.2$ is similarly well understood, and is due to limited coverage, as the endcap outer chamber-layer does not cover the range $1.0 < \eta < 1.4$, and there are holes in the inner chamber-layer.

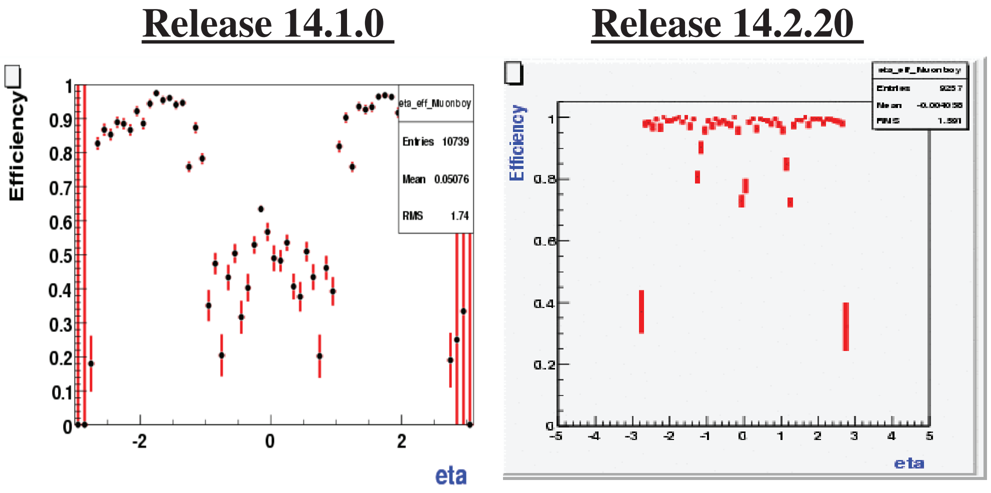

Figure A.1. Muon reconstruction efficiency for the Staco algorithm as a function of pseudorapidity, under the removal of the middle chamber layer of MDTs, shown for two different software releases.

Figure A.3 shows the same efficiency plot, but now removing all inner MDTs and the CSCs. There are periodic losses of efficiency in the barrel region, likely due to gaps in the middle MDTs, where the toroid ribs intersect the chamber-layer. There are also large losses in the transition region, in which some muons may only cross two chamber-layers of MDTs, including the removed inner layer.

The pattern of efficiency loss is quite similar for the removal of the middle chamber-layer of MDTs. Figures A.4 and A.5 shows the efficiency for the removal of no, inner, middle, and outer chamber-layer MDTs for Moore and Muonboy, respectively. This efficiency is binned into large eta regions: barrel (0-1.0), transition(1.0-1.4), endcap(1.4-2.0) and forward (2.0-2.5). The transition and forward regions correspond to the region lacking outer layer coverage and the region covered by the CSCs, respectively. The effect of the removal of the outer chamber-layer of MDTs is quite different from the other two layers. Efficiency loss in the barrel is moderate, again, likely due to gaps in the middle chamber-layer. However, there is little loss in the transition region, or in the endcap. There are no gaps in the inner and middle chamber-layers in this eta

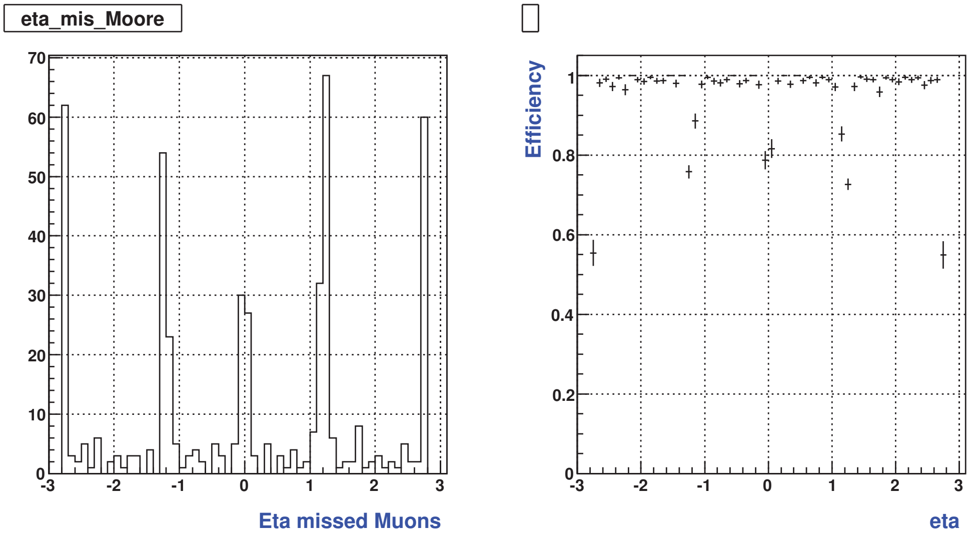

Figure A.2. Pseudorapidity distribution for true muons that are not reconstructed (left) and muon reconstruction efficiency as a function of pseudorapidity (right) for the Moore algorithm.

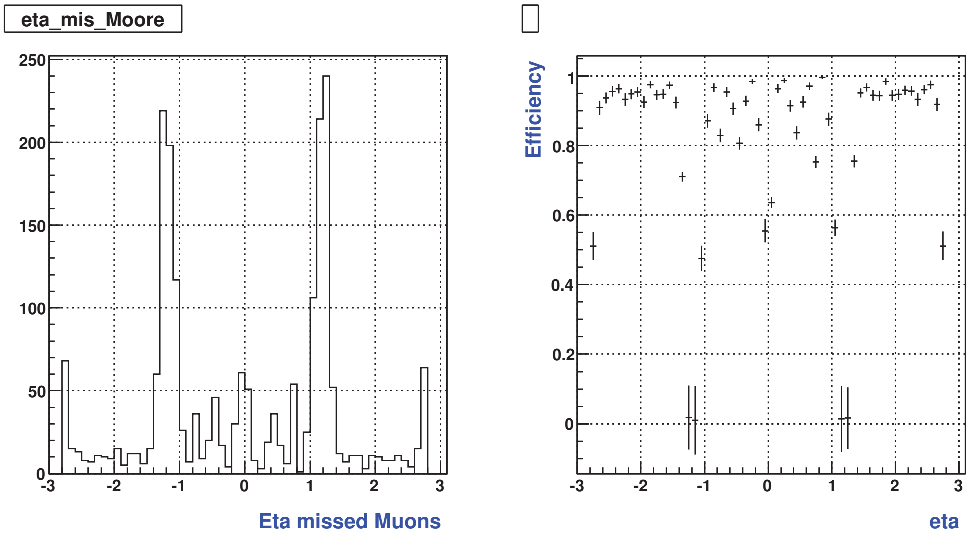

Figure A.3. Pseudorapidity distribution for true muons that are not reconstructed (left) and muon reconstruction efficiency as a function of pseudorapidity (right) for the Moore algorithm while removing the inner chamber-layer of MDTs.

region. The toroid lies between these two chamber-layers, and therefore, the primary field integral of a reconstructed muon is between these two layers. This is likely the reason for the relative insensitivity to the removal of the outer chamber-layer.

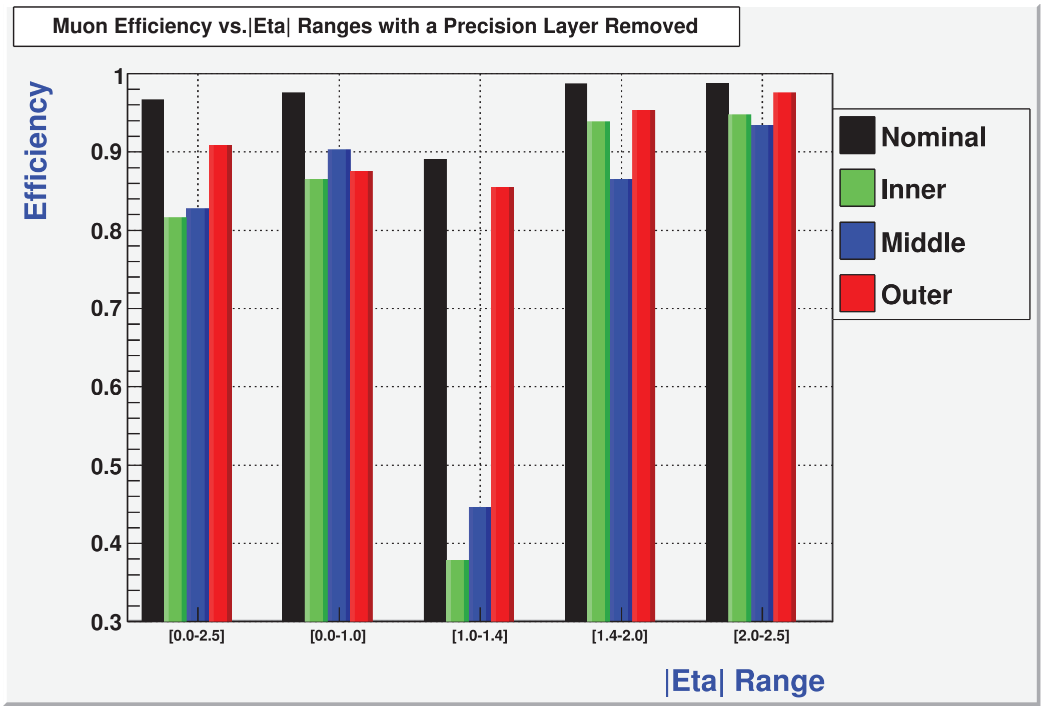

Figure A.4. Muon reconstruction efficiencies for various pseudorapidity ranges, as a chamber-layer of precision chambers is removed (Moore). Pseudorapidity ranges are chosen for the following reasons: $1.0 < \eta < 1.4$ is the range between the end of the barrel outer MDTs and the endcap outer MDTs, $\eta = 2.0$ represents the beginning of the CSCs, and $\eta = 2.5$ represents the end of inner detector coverage.

Comparison of Reconstruction Algorithms

Any measure of muon reconstruction performance in ATLAS must recognize the existence of two competing families of algorithms. It is difficult, however, to compare these algorithms in an equivalent manner. There are two related reasons for this. The first is that Muonboy applies tighter selection on tubes which are crossed by a reconstructed track, but which have no signal (holes). This is done as a way to reduce fake muons during reconstruction. However, this causes efficiency loss if the hole is

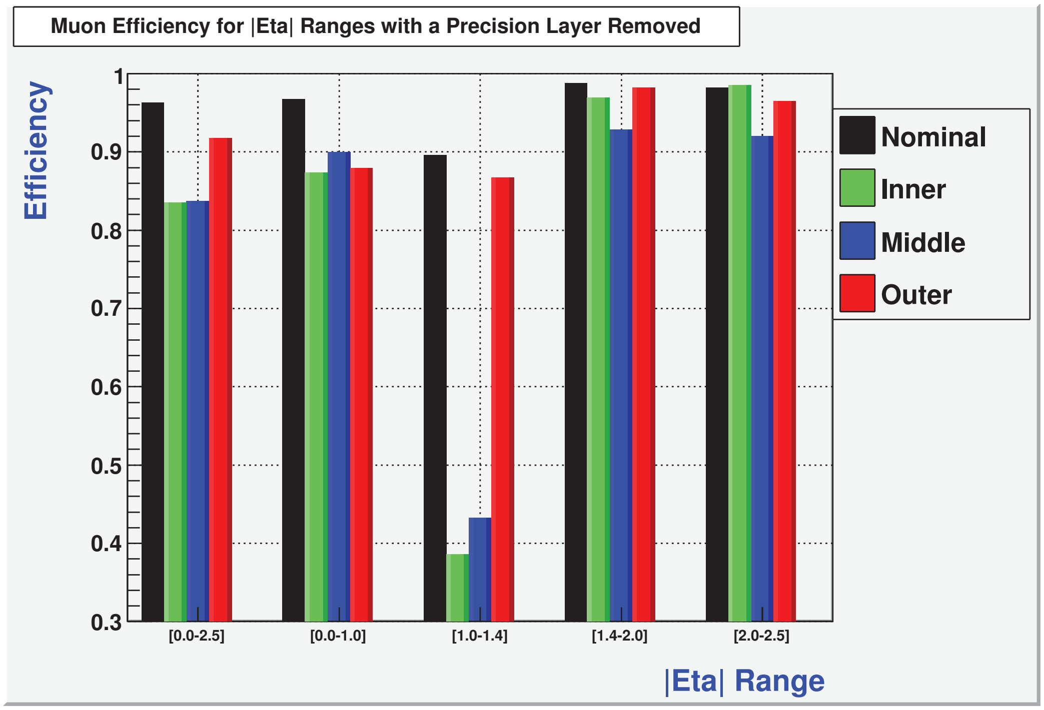

Figure A.5. Muon reconstruction efficiencies for various pseudorapidity ranges, as a chamber-layer of precision chambers is removed (Muonboy).

due to hardware inefficiency. In current running, there is a database based service to alert the algorithms as to which chambers are not functioning. However, at the time this study was performed, Muonboy had only a "by hand" method to take into account dead tubes (avoiding some loses due to rejection of events with holes), and Moore had no way to take this information into account at all.

Figure A.6 compares Moore and Muonboy for each possible removal of a single multi-layer or both multi-layers for a chamber-layer. CSCs are removed when the inner chamber-layer is removed, but not when a single multi-layer is removed. Due to difficulties in comparison, results for Muonboy are shown both with and without knowledge of the chamber removal. In all cases, we see the following pattern: Muonboy with knowledge of the removal performs the best, but without knowledge of the removal Moore outperforms Muonboy. This is especially true when only a single multi-layer is removed. When an entire chamber-layer is removed, the performance is more similar. Finally, Muonboy seems to struggle when the entire inner chamber-layer is removed without its knowledge, although this is quite an unlikely scenario from an instrumental viewpoint.

Momentum Resolution

Even when efficiency is not lost, any chamber failure will have some effect on the muon momentum resolution. Figures A.7 and A.8 show the normalized transverse momentum residual distribution for Muonboy and Moore when the middle chamber-layer of MDTs is removed. Overflows are not included in the Gaussian fit. Figure A.9 shows the width of the single Gaussian resolution fit for each set of chamber removals. For removal of the inner chamber-layer, the plot shows separate results for the barrel ($\eta < 1$) and the endcap ($\eta > 1$), due to the dramatic effects on reconstruction in the endcap for this case. The comparison between Moore and Muonboy is not equivalent in this case. Muonboy applies a loose constraint based on the location

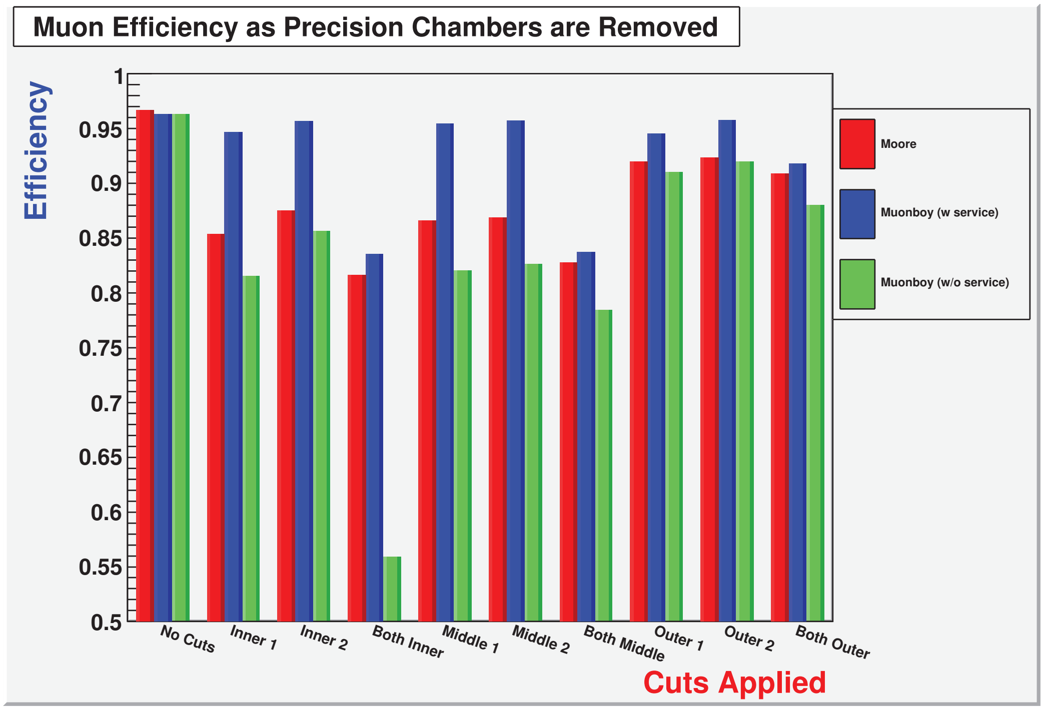

Figure A.6. Muon reconstruction efficiency for Moore and Muonboy under various sets of removed chambers.

of the interaction point, while this is not done for Moore. For this reason, Moore cannot determine the momentum in the endcap, because there is little magnetic field between the middle and outer chamber-layers. This issue does not hamper the performance of the Moore algorithm, as later stages of reconstruction (MuidStandalone) include full extrapolation back to the interaction point, which provides a momentum measurement.

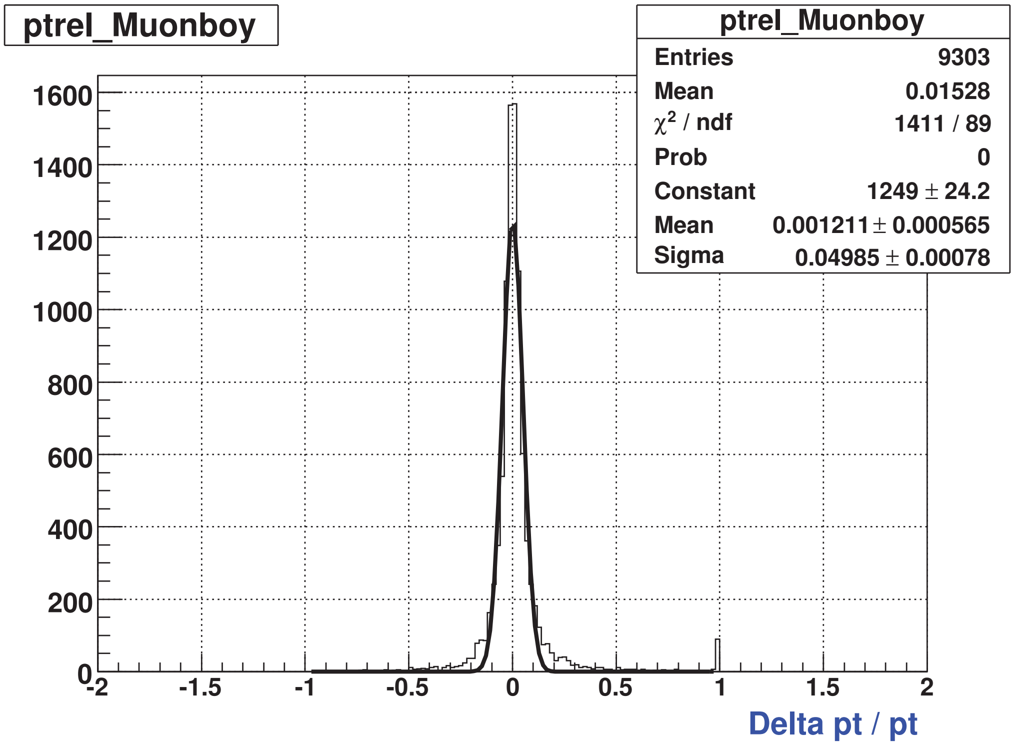

Figure A.7. Normalized transverse momentum residual distribution for Muonboy, while removing the middle chamber-layer of MDTs. The fit is to a single Gaussian, excluding overflow.

Results for Combined Muon Reconstruction

Efficiency and Resolution

As previously mentioned, the combined algorithms start with a muon spectrometer track, and extrapolate into the inner detector. Small inefficiencies in matching ID

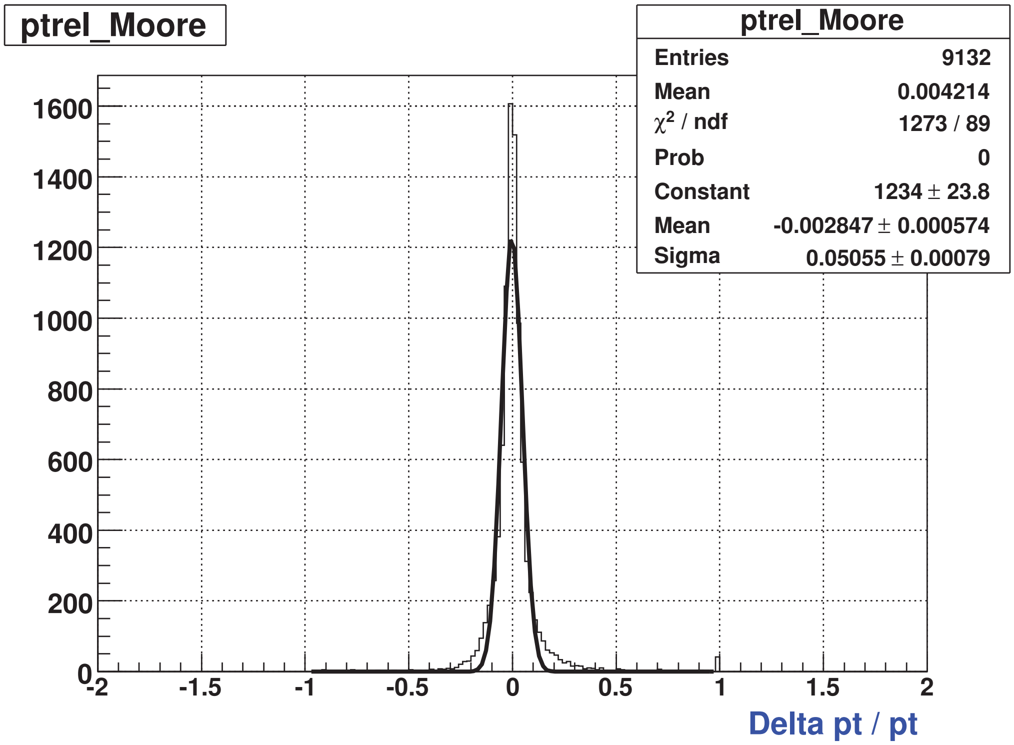

Figure A.8. Normalized transverse momentum residual distribution for Moore, while removing the middle chamber-layer of MDTs. The fit is to a single Gaussian, excluding overflow.

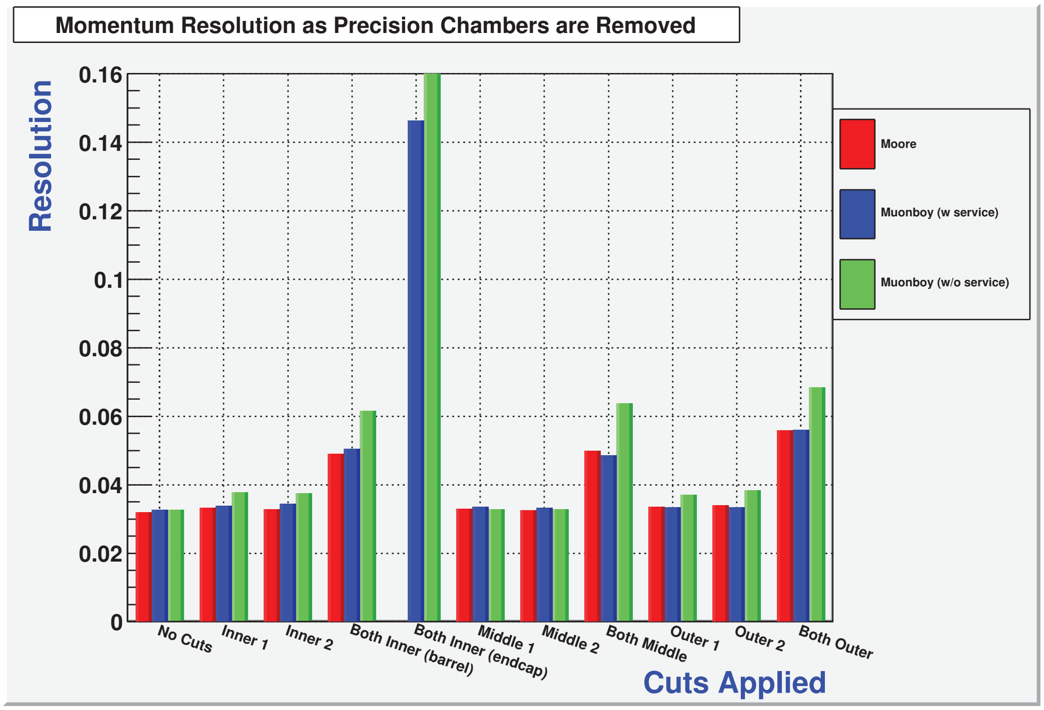

Figure A.9. Width of the single Gaussian transverse momentum resolution fit, as a function of removed chambers. For the removal of the inner chamber-layer, results are listed separately for the barrel ($\eta < 1$) and the endcap ($\eta > 1$). For the endcap in this case, there is not enough magnetic flux to make a momentum measurement. Muonboy gets a momentum measurement by applying a weak IP constraint. Such tracks do not have a momentum measurement for Moore, but are recovered in later stages of reconstruction.

and MS tracks lead to their efficiencies being slightly lower than the corresponding muon spectrometer algorithms. Figure A.10 shows a comparison of the efficiency of muon spectrometer and combined algorithms, as chambers are removed. The patterns of efficiency loss due to the removals are nearly identical between the combined algorithms and their MS only counterpart. Figures A.11, A.12 and A.13 show these losses as a function of pseudorapidity for the removal of the inner, middle, and outer chamber-layers, respectively.

Figure A.14 shows the momentum resolution as a function of removed chambers for the combined algorithms. In the momentum range below about 50 GeV, the inner detector resolution is better than that of the muon spectrometer, and thus dominates the combined reconstruction. This means that for this case the impact of missing muon spectrometer chambers on the combined momentum resolution is minimal.

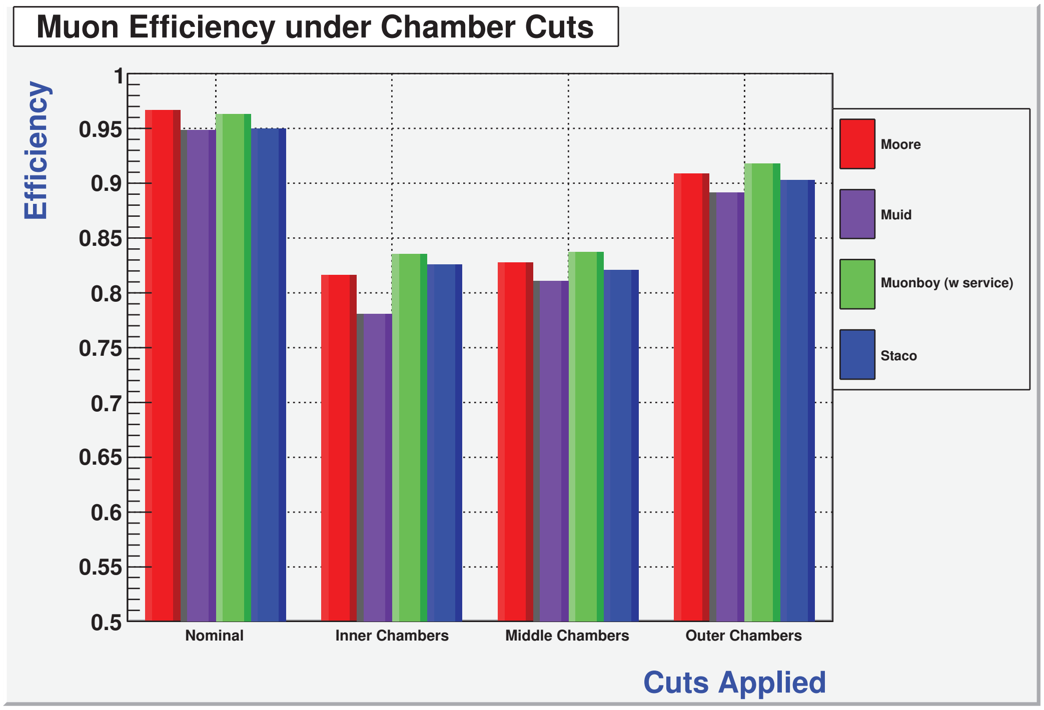

Figure A.10. Reconstruction efficiency for muon spectrometer and combined algorithms, under the removal of precision chambers.

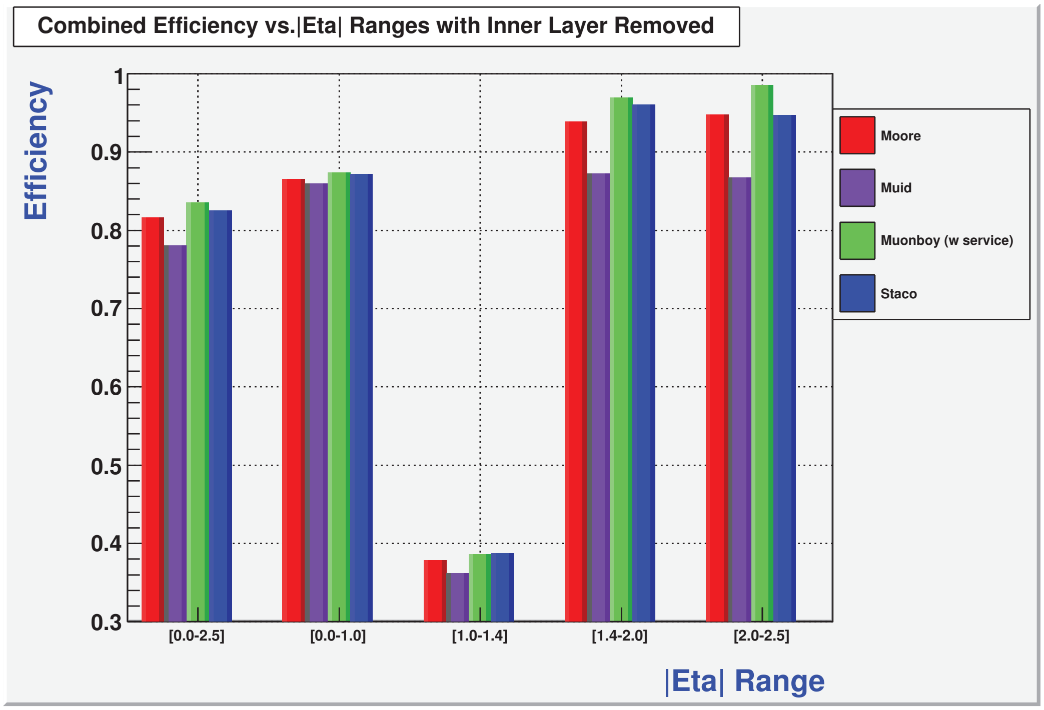

Figure A.11. Reconstruction efficiency for muon spectrometer and combined algorithms, under the removal of the inner chamber-layer of MDTs and CSCs, for various pseudorapidity ranges.

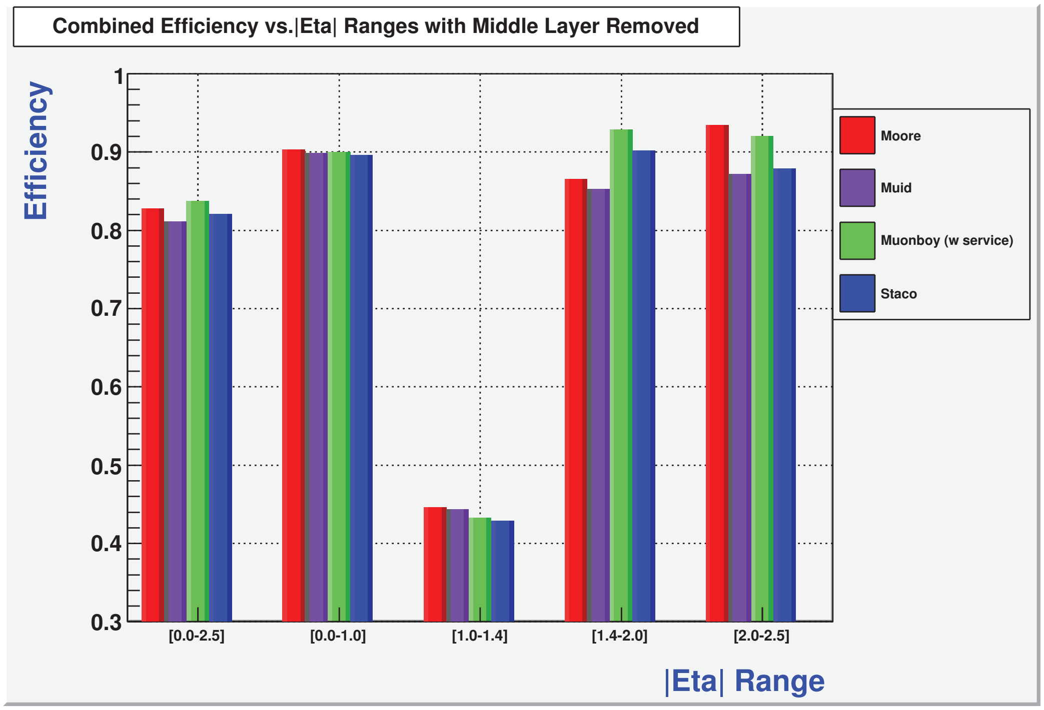

Figure A.12. Reconstruction efficiency for muon spectrometer and combined algorithms, under the removal of the middle chamber-layer of MDTs, for various pseudorapidity ranges.

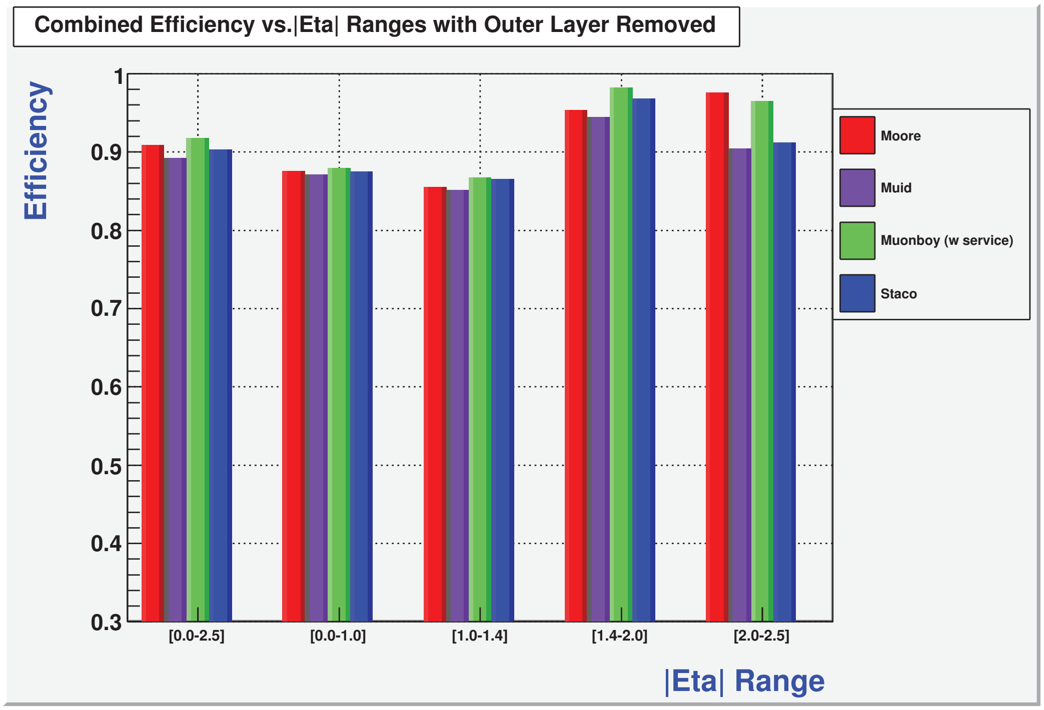

Figure A.13. Reconstruction efficiency for muon spectrometer and combined algorithms, under the removal of the outer chamber-layer of MDTs, for various pseudorapidity ranges.

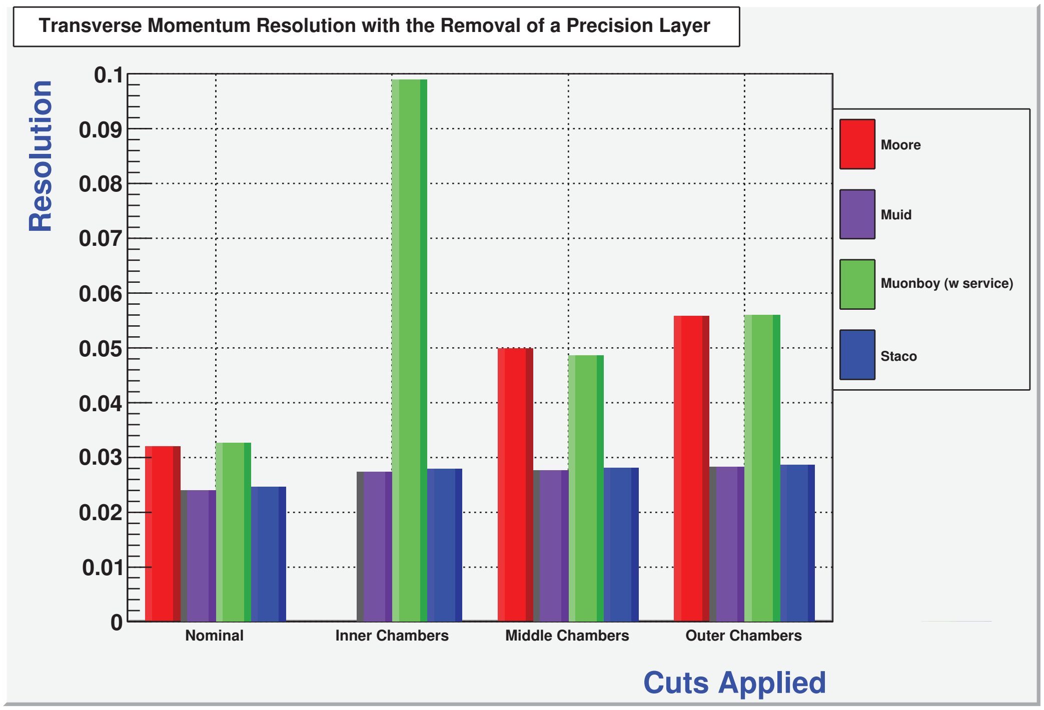

Figure A.14. Transverse momentum resolution for muon spectrometer and combined algorithms, under the removal of precision chambers. Moore is omitted for removal of the inner chamber-layer for reasons discussed in the text.

Effect of Tagging Algorithms

Tagging algorithms aim to identify muons which only have one or two reconstructed segments in the muon spectrometer, due to the fact that they begin with an inner detector track and work outwards into the muon spectrometer. For this reason, they are promising from the viewpoint of robustness. Figure A.15 shows the effect of removed chambers on the AOD muon containers, which combine a muon spectrometer only algorithm, a combined algorithm (Muid or Staco), and a tagging algorithm. It is clear that these tagging algorithms improve insensitivity to chamber failure. MuTag seems to be slightly less effective at improving robustness than the other two algorithms. This is likely due to the fact that MuTag only uses inner chambers to produce tagged muons (and middle stations over around a pseudorapidity of 1.2), while MuTagIMO and MuGirl can both produce tagged muons from a segment in any chamber-layer.

Summary and Conclusion

Muon reconstruction algorithms Moore and Muonboy are found to have similar robustness under chamber failure. Muonboy has an advantage of 5 to 10% over Moore when a single multi-layer is removed, likely due to the fact that incorporates knowledge of the loss of these chambers. In current versions of the ATLAS software a dead-tube service alerts both algorithms of known dysfunctional detector elements. Moore has a small advantage in robustness when Muonboy does not include knowledge of chamber loss. Overall, this study suggests that ATLAS muon reconstruction algorithms are very robust against all but the most dramatic failures of MDT or CSC chambers. Even when an entire chamber-layer is removed, efficiency losses are on the order of 5 to 15%, and momentum resolution by about 50%. The combined algorithms show similar efficiency losses but little loss of resolution (though this is not expected to be the case for samples with higher momentum). Efficiency losses due to chamber

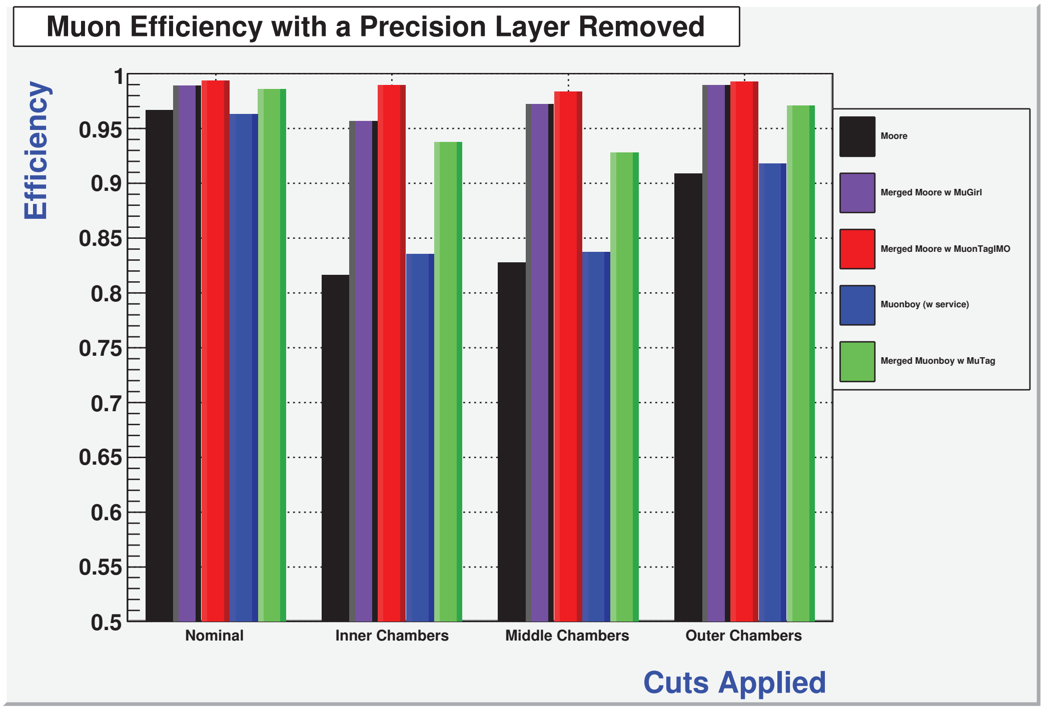

Figure A.15. Efficiency as a function of removed chambers for muon spectrometer algorithms, and merged collections. Merged collections include a standalone algorithm (e.g.Moore), a combined algorithm (e.g.Muid), and a tagging algorithm (e.g.MuGirl).

failure can be mostly recovered if tagging algorithms are used in reconstruction. This study shows that the loss of efficiency of these algorithms under the removal of the chamber-layer is only of the order of 1%.

BIBLIOGRAPHY

[1] Aad, Georges, et al. Observation of a new particle in the search for the Standard Model Higgs boson with the ATLAS detector at the LHC. *Phys.Lett. B716* (2012), 1–29.

[2] Kane, G. The Dawn of Physics Beyond the Standard Model. *Scientific American June* (2003), 60.

[3] Koch, Volker. Introduction to chiral symmetry. *arXiv:nucl-th/9512029* (1995).

[4] S. Weinberg. A model of leptons. *Phys. Rev. Lett.*, 19 (1967), 1264–1266.

[5] A. Salam. Weak and electromagnetic interactions. *Elementary Particle Theory, Proceedings Of The Nobel Symposium Held At Lerum, Sweden* (1968), 367–377.

[6] S. L. Glashow. Partial symmetries of weak interactions. *Nucl. Phys. 22* (1961), 579–588.

[7] Aad, Georges, et al. A measurement of the ratio of the W and Z cross sections with exactly one associated jet in pp collisions at $\sqrt{s} = 7$ TeV with ATLAS. *Phys.Lett. B708* (2012), 221–240.

[8] Abulencia, A., et al. Measurements of Inclusive W and Z Cross Sections in p-pbar Collisions at sqrts =1.96 TeV. *J. Phys. G 34* (2007), 2457.

[9] M. Peskin, and D. Schroeder. *An Introduction To Quantum Field Theory.* Addison-Wesley Advanced Book Program, 1995.

[10] J. Donoghue, E. Golowich, and B. Holstein. *Dynamics of the Standard Model.* Cambridge Monographs on Particle Physics, Nuclear Physics and Cosmology, 1996.

[11] Thomas, Shaun A., Abdalla, Filipe B., and Lahav, Ofer. Upper Bound of 0.28eV on the Neutrino Masses from the Largest Photometric Redshift Survey. *Phys.Rev.Lett. 105* (2010), 031301.

[12] Higgs, Peter W. Broken symmetries and the masses of gauge bosons. *Phys. Rev. Lett. 13* (Oct 1964), 508–509.

[13] Kobayashi, Makoto, and Maskawa, Toshihide. *cp*-violation in the renormalizable theory of weak interaction. *Progress of Theoretical Physics 49*, 2 (1973), 652–657.

[14] Akrawy, M.Z., et al. Measurement of the Z^0 Mass and Width with the OPAL Detector at LEP. *Phys.Lett. B231* (1989), 530.

[15] Zwicky, F. On the Masses of Nebulae and of Clusters of Nebulae. *ApJ 86* (Oct. 1937), 217.

[16] Clowe, D., Bradač, M., Gonzalez, A. H., Markevitch, M., Randall, S. W., Jones, C., and Zaritsky, D. A Direct Empirical Proof of the Existence of Dark Matter. *ApJ 648* (Sept. 2006), L109–L113.

[17] Niessen, Irene. Supersymmetric Phenomenology in the mSUGRA Parameter Space. *arXiv:0809.1748* (2008).

[18] Aaltonen, T., et al. Search for New Particles Leading to $Z+$ jets Final States in $p\bar{p}$ Collisions at $\sqrt{s} = 1.96$- TeV. *Phys. Rev. D76* (2007), 072006.

[19] Devenish, R., and Cooper-Sarkar, A. *Deep inelastic scattering.* Oxford University Press, Oxford, New York, USA, 2004.

[20] A. D. Martin, W. J. Stirling, R. S. Thorne, and Watt, G. Parton distributions for the lhc. *Eur. Phys. J. C 63* (2009), 189–285.

[21] P. M. Nadolsky et. al. Implications of CTEQ global analysis for collider observables. *Phys. Rev. D 78*, 013004 (2008).

[22] Agostinelli, S., et al. GEANT4 - a simulation toolkit. *Nucl. Inst. and Meth A506* (2003), 250.

[23] Mangano, M. Ll, et al. "alpgen, a generator for hard multiparton processes in hadronic collisions". *JHEP 0307* (2003), 001.

[24] Butterworth, J. M., Forshaw, Jeffrey R., and Seymour, M. H. Multiparton interactions in photoproduction at HERA. *Z. Phys. C72* (1996), 637.

[25] Gleisberg, T., et al. "event generation with sherpa 1.1". *JHEP 0902* (2009), 007.

[26] Berger, C.F., Bern, Z., Dixon, Lance J., Febres Cordero, F., Forde, D., et al. Vector Boson + Jets with BlackHat and Sherpa. *Nucl.Phys.Proc.Suppl. 205-206* (2010), 92–97.

[27] Sjöstrand, T., Mrenna, S., and Skands, P. PYTHIA 6.4 physics and manual. *JHEP 05* (2006), 026.

[28] Golonka, P., and Was, Z. Next to Leading Logarithms and the PHOTOS Monte Carlo. *Eur.Phys.J. C50* (2007), 53–62.

[29] Corcella, G., et al. HERWIG 6.5: an event generator for Hadron Emission Reactions With Interfering Gluons (including supersymmetric processes). *JHEP 0101* (2001), 010.

[30] Frixione, Stafano, and Webber, Bryan R. The MC@NLO 3.3 Event Generator. *arXiv:hep-ph/0612272* (2006).

[31] L. Evans, and P. Bryant. LHC machine. *JINST 3*, 08 (2008), S08001.

[32] Virdee, T.S. The LHC project: The accelerator and the experiments. *Nucl.Instrum.Meth. A623* (2010), 1–10.

[33] The ATLAS Collaboration, G. Aad et al. The ATLAS Experiment at the CERN Large Hadron Collider. *JINST 3* (2008), S08003.

[34] S. Myers. The LEP collider from design to approval and commissioning (lecture). http://sl-div.web.cern.ch/sl-div/history/lep_doc.html.

[35] CERN, http://public.web.cern.ch/public/en/research/AccelComplex-en.html.

[36] A. A. Glazkov, N. R. Lobanov, I. S. Balikoev, V. T. Barchenko, and S. I. Zagranichny. Duoplasmatron-type ion source with improved technical and operational performance for linear accelerator.

[37] Aad, G., et al. The ATLAS Experiment at the CERN Large Hadron Collider. *JINST 3* (2008), S08003.

[38] Aad, G. et al. *Expected performance of the ATLAS experiment: detector, trigger and physics*. CERN, Geneva, 2009.

[39] S. Catani, Y. L. Dokshitzer, M. H. Seymour, and Webber, B. R. "successive combination jet algorithm for hadron collisions". *Nucl. Phys. B 406* (1993), 187.

[40] Cacciari, Matteo, Salam, Gavin P., and Soyez, Gregory. "the anti-k_t jet clustering algorithm". *JHEP 04* (2008), 063.

[41] Y. L. Dokshitzer, G. D. Leder, S. Moretti, and Webber, B. R. "better jet clustering algorithms". *JHEP 9708* (1997), 001.

[42] Aad, G. et al. New atlas event generator tunes to 2010 data. Tech. Rep. ATL-PHYS-PUB-2011-008, CERN, Geneva, Apr 2011.

[43] Stump, Daniel, Huston, Joey, Pumplin, Jon, Tung, Wu-Ki, Lai, H.L., et al. Inclusive jet production, parton distributions, and the search for new physics. *JHEP 0310* (2003), 046.

[44] Lai, Hung-Liang, Guzzi, Marco, Huston, Joey, Li, Zhao, Nadolsky, Pavel M., Pumplin, Jon, and Yuan, C.-P. New parton distributions for collider physics. *Phys.Rev. D82* (2010), 074024.

[45] Kersevan, B., and Richter-Wa, E. *Eur. Phys. J. C 39* (2005), 439.

[46] D'Agostini, G. A Multidimensional unfolding method based on Bayes' theorem. *Nucl.Instrum.Meth. A362* (1995), 487–498.

[47] Chatrchyan, Serguei, et al. Jet Production Rates in Association with W and Z Bosons in pp Collisions at $\sqrt{s} = 7$ TeV. *JHEP 1201* (2012), 010.

[48] Meade, A, and Willocq, S. Robustness of muon reconstruction algorithms under partial mdt and csc chamber failures. Tech. Rep. ATL-MUON-INT-2009-003. ATL-COM-MUON-2009-005, CERN, Geneva, Mar 2009.